

REPORT DOCUMENTATION PAGE

0536

Public reporting burden for this collection of information is estimated to average 1 hour per response, including the time for reviewing instructions, searching existing data sources, gathering the required data, completing and reviewing this collection of information. Send comments regarding this burden estimate or any other aspect of this burden to Department of Defense, Washington Headquarters Services, Directorate for Information Operations and Reports (0704-0188), 4302. Respondents should be aware that notwithstanding any other provision of law, no person shall be subject to any penalty for failing to provide information unless it is specifically required by an act of Congress. **PLEASE DO NOT RETURN YOUR FORM TO THE ABOVE ADDRESS.**

1. REPORT DATE (DD-MM-YYYY) 26-09-2004		2. REPORT TYPE Final Technical Report		3. DATES COVERED (From - To) 15-12-2000 - 14-12-2003	
4. TITLE AND SUBTITLE Experimental Study of Nonlinear Behavior in Hypersonic Laminar Boundary Layer				5a. CONTRACT NUMBER F49620-01-1-0105	
				5b. GRANT NUMBER N/A	
				5c. PROGRAM ELEMENT NUMBER N/A	
6. AUTHOR(S) Chokani, Ndaona				5d. PROJECT NUMBER N/A	
				5e. TASK NUMBER N/A	
				5f. WORK UNIT NUMBER N/A	
7. PERFORMING ORGANIZATION NAME(S) AND ADDRESS(ES) NC State University Office of Contracts and Grants Campus Box 7214 Raleigh NC 27695-7214				8. PERFORMING ORGANIZATION REPORT NUMBER N/A	
9. SPONSORING / MONITORING AGENCY NAME(S) AND ADDRESS(ES) Unsteady Aerodynamics & Hypersonics Program AFOSR /NA 4015 Wilson Blvd, Room 713 Arlington, VA 22203-1954				10. SPONSOR/MONITOR'S ACRONYM(S) AFOSR	
				11. SPONSOR/MONITOR'S REPORT NUMBER(S) N/A	
12. DISTRIBUTION / AVAILABILITY STATEMENT Approved for public release. Distribution unlimited.					
13. SUPPLEMENTARY NOTES N/A					
14. ABSTRACT Three high order spectral analysis techniques - the short-time Fourier transform (STFT), the Fourier bispectrum, and the STFT bispectrum - are developed and used to characterize the nonlinear dynamics of a transitioning hypersonic boundary layer flow. The hot-wire measurements in a transitioning boundary layer in the NASA Langley Mach 6 quiet tunnel are analyzed, and the effects of wall cooling and adverse pressure gradient on the nonlinear dynamics are examined. The STFT identifies the modulation of the dominant second mode and its harmonic in the nonlinear region of the transition process. Phase modulation is observed to be the primary energy transfer mechanism, but in the latter nonlinear stages the role of amplitude modulation is increasingly important. The Fourier bispectrum quantifies the modulation as a low frequency phase coupled quadratic interaction. In addition, the Fourier bispectrum quantifies the dominant role of the second mode through its forcing of harmonic quadratic interactions. The STFT bispectrum identifies the transient stages of nonlinear interactions that are observed to be important in the nonlinear stages of transition. These nonharmonic, broadband interactions may offer new approaches for control of hypersonic transition.					
15. SUBJECT TERMS Hypersonics. Boundary Layer Transition. High-order Spectral Analysis.					
16. SECURITY CLASSIFICATION OF:			17. LIMITATION OF ABSTRACT	18. NUMBER OF PAGES	19a. NAME OF RESPONSIBLE PERSON
a. REPORT Unclassified	b. ABSTRACT Unclassified	c. THIS PAGE Unclassified			Ndaona Chokani
			None	129	19b. TELEPHONE NUMBER (include area code) 919-660-5333

20041028 087

BEST AVAILABLE COPY

Table of Contents

List of Tables.....	vi
List of Figures.....	vii
List of Symbols.....	xiv
1. Introduction.....	1
1.1. Hypersonic Transition.....	1
1.1.1. Applications.....	1
1.1.2. Boundary Layer Stability.....	1
1.1.3. Wind Tunnel Noise.....	3
1.1.4. Previous Experiments.....	4
1.1.5. Previous Computations	5
1.2. Nonlinear Interactions.....	6
1.3. Objectives.....	8
2. Approach.....	10
2.1. Quiet Tunnel.....	10
2.1.1. Quiet Tunnel Technology.....	10
2.1.2. Lachowicz and Blanchard Experiments.....	11
2.1.3. Constant Voltage Anemometer.....	12
2.2. High Order Spectral Analysis.....	15
2.2.1. Short-Time Fourier Transform.....	16
2.2.2. Bispectrum.....	17
2.2.3. STFT Bispectrum.....	19
3. Results and Discussions.....	21
3.1. Short-Time Fourier Transform.....	21
3.1.1. Spectrogram.....	21
3.1.2. Amplitude and Phase Modulations.....	24
3.1.3. Kurtosis and Skewness.....	26
3.1.4. Harmonic Frequency Band.....	28
3.2. Fourier Bispectrum.....	30
3.2.1. Baseline.....	31

3.2.2. Effect of Wall Cooling.....	32
3.2.3. Effect of Pressure Gradient.....	33
3.3. STFT Bispectrum.....	34
3.3.1. Baseline.....	35
3.3.2. Effect of Wall Cooling.....	38
3.3.3. Effect of Pressure Gradient.....	40
4. Concluding Remarks.....	43
4.1. Summary of Results.....	43
4.2. Recommendations for Future Work.....	45
5. References.....	47
6. Tables.....	51
7. Figures.....	52

List of Symbols

Roman Symbols

$2f_o, 3f_o$	First and second harmonic of the second mode frequency
a_w	Hot-wire overheat ratio
A	Coefficient for M_{CVA} estimation
b'	Calibration coefficient in CVA transfer function
$b^2(f_1, f_2)$	Bispectrum
$b_F^2(f_1, f_2)$	Fourier bispectrum
$b_S^2(T, f)$	Summed bispectrum
$b_{STFT}^2(T, f_1, f_2)$	STFT bispectrum
$b_T^2(T)$	Total bispectrum
B	Coefficient for M_{CVA} estimation
c_w	Specific heat of hot-wire material
C	Capacitance in CVA frequency compensation circuit
d	Diameter of the hot-wire sensor
e'	Fluctuating output voltage of CVA
e'_w	Fluctuating hot-wire voltage
e'_{corr}	Software corrected fluctuating CVA output voltage
e'_{raw}	CVA fluctuating output voltage before software correction
E	Total CVA output voltage (mean plus fluctuation), Mean output of CVA
f, f_1, f_2, f_l, f_k	Frequency in Hertz
f_N, F_N	Nyquist frequency
f_o	Frequency of the most amplified second mode disturbance
f_s	Sampling frequency
f_t	Operational amplifier frequency in CVA
$G_s(t, f)$	Short-time Fourier transform of $s(t)$
I_w	Hot-wire current
i'_w	Hot-wire current fluctuation

i, j	$\sqrt{-1}$
k_a	Heat conductivity of air
K	Nondimensional CVA output
M	Mach Number, Number of STFT segments
M_{CVA}	Hot-wire time constant for CVA
$n(f)$	Number of elements summed for the summed bispectrum
N	Number of data points in the time series
N_B	Number of STFT bispectra
N_E	Number of ensembles used to compute STFT bispectrum
N_{FFT}	Number of data points in time series used to compute the FFT
p	Pressure term in Navier-Stokes
$P_{xx}(f), P$	Power spectral density
r	Ratio of sensitivity coefficients
R	Stability Reynolds number, correlation coefficient, radius of curvature of the cone flare
R_I	Resistance in CVA circuit
R_2	$R_a + R_b$
R_a, R_b, R_d, R_F	Resistance in CVA circuit
R_W	Hot-wire resistance
s	Laplace operator
$s(t)$	Time series
$S(f)$	Fourier transform of $s(t)$
S_{To}	Sensitivity coefficient for total temperature fluctuations
$S_{\rho u}$	Sensitivity coefficient for mass flux fluctuations
t, t'	Time
t_n	Time in skewness and kurtosis calculation
T	FFT time interval, time of STFT bispectrum
T_C	Hardware time constant for CVA
T_o	Total or stagnation temperature
T_{To}	Normalized RMS total temperature fluctuations

$T_{\rho u}$	Normalized RMS mass flux fluctuations
u	Velocity
\bar{u}	Velocity vector in the Navier-Stokes equation
V_l	Reference dc voltage in CVA
V_i	Voltage in the CVA circuit
V_w	Voltage across the hot-wire in the CVA
x	Axial distance measured from apex of the flared-cone model

Greek Symbols

α	Amplitude modulation index, r – intercept in fluctuation diagram
β	Phase modulation index, r – intercept in fluctuation diagram
δ_f	Modulation or sideband frequency
Δf	Frequency resolution
$\Delta t'$	Temporal resolution in data time series
Δt	Temporal resolution in STFT
ΔT	Time duration of STFT bispectrum
γ	Angle in fluctuation diagram
γ^*	Running analysis window
κ	Dilation or scale parameter for wavelet analysis
K	Kurtosis
Λ	Skewness
μ	Mean
ν	Kinematic viscosity
π	3.14159...
Θ	Virtual total temperature fluctuation
ρ	Density
ρu	Mass flux
ρ_w	Hot-wire density
σ	Root mean square

τ	Delay time or translational parameter for wavelet analysis
ω_n	Natural frequency

Subscripts

∞	Freestream
----------	------------

Superscripts

*	Complex conjugate
()'	Fluctuating quantity

Abbreviations

91-6	Refers to geometric description of the Blanchard and Selby model (Reference 21)
93-10	Refers to geometric description of the Lachowicz <i>et al</i> model (Reference 35)
AC	Alternating current
AEDC	Arnold Engineering and Development Center
CCA	Constant current anemometer
CTA	Constant temperature anemometer
CVA	Constant voltage anemometer
DC	Direct current
DCD	Digital complex demodulation
DNS	Direct numerical simulation
FFT	Fast / finite Fourier transform
HOSA	High order spectral analysis
LST	Linear stability theory analysis
NASA	National Aeronautics and Space Administration
PC	Personal computer
PSD	Power spectral density

PSE	Parabolized stability equations
RMS	Root mean squared
STFT	Short-time Fourier transform

Units of Measurement

<i>dB</i>	Decibels
<i>ft</i>	Foot
<i>kHz</i>	Kilohertz
<i>in</i>	Inch
<i>kg</i>	Kilogram
<i>K</i>	Degrees Kelvin
<i>m/s</i>	Meters per second
<i>mm</i>	Millimeter
<i>ms</i>	Millisecond
<i>mV</i>	Millivolts
<i>MHz</i>	Megahertz
<i>psia</i>	pounds per square inch, absolute
<i>rad</i>	Radians
<i>W</i>	Watts
<i>s, sec</i>	Second
<i>μm</i>	Micrometer
<i>Ω</i>	Ohms
<i>/ft</i>	Per foot
<i>°R</i>	Degrees Rankine

Miscellaneous Symbols

$\langle \rangle$	Time average or a normalized quantity
$ $	Magnitude of a quantity
$\overline{()}$	Time average or mean of a quantity
\angle	Phase of a quantity
$[i]$	Segment over which the STFT bispectrum is evaluated, $i = 1, 2, \dots, 7$
$\Re(t)$	Real part
$\Im(t)$	Imaginary part
∂	Partial derivative
∇	Gradient operator
\cdot	Dot product
d/dt	Time derivative of a quantity
\rightarrow	“Produces through nonlinear phase coupled interactions”

INTRODUCTION

1.1 Hypersonic Transition

1.1.1 Applications

There is presently a strong interest in the development of air breathing hypersonic vehicles to be used for rapid global access. A critical aspect in the design of these vehicles is knowledge of the position of laminar to turbulent transition. An early transition results in increases in the skin friction and the surface heat transfer. The higher heating results in an increase in the weight of the thermal protection system, and thus a reduced payload mass fraction. The larger viscous drag resulting from the turbulent flow has an adverse effect on the aerodynamic performance of the vehicle.¹

Transition prediction methods shall play an important role in the development of these vehicles. The improvement in the capabilities of these predictive tools requires a better understanding of the physical processes related to hypersonic transition processes. This improved understanding shall also enable the development of transition control techniques. Recently a very promising passive control method has been demonstrated,^{2,3} But, it is known that passive control methods cannot be adapted in time and space. However, if the flow physics are better understood, it may, in the future, be possible to develop active control methods whereby the flow is locally and dynamically manipulated.

1.1.2 Boundary Layer Stability

The boundary layer transition process is characterized by the development and growth of instability modes that are present in the boundary layer. In a hypersonic

imperfections, and the sound propagating from the settling chamber and the valves that are upstream of the test section. If the flow is properly conditioned and the nozzle is carefully fabricated, the latter two sources are dominated by the noise radiating from the turbulent boundary layer on the tunnel walls.⁹ Therefore, the key to designing a quiet wind tunnel is to extend the region of laminar flow on the tunnel wall. Wilkinson¹⁰ summarizes the quiet tunnel work at NASA Langley that culminated in the development of the Mach 6 quiet tunnel.

1.1.4 Previous Experiments

Boundary layer stability experiments provide details of the mechanisms that subsequently lead to transition. The stability experiments of Kendall¹¹ provided the first confirmation of the existence and dominance of the second-mode disturbances in hypersonic boundary layer flow. At AEDC, Stetson *et al* employed thermal anemometry in a series of experiments that examined the stability of laminar boundary layer flow over a straight cone¹² including the effects of nose-tip bluntness,¹³ unit Reynolds number,¹⁴ and wall cooling.¹⁵ Kimmel *et al*⁵ documented the spatial structure of the second-mode disturbance in a transitional hypersonic boundary layer through the two simultaneous hot-film probe measurements on a sharp cone. Kimmel and Poggie^{16,17} have more recently further examined the spatial structure of the second-mode disturbance. Although the experiments mentioned above have significantly improved our understanding of the hypersonic transition process, they were conducted in conventional wind tunnels and thus potentially suffer from the effects of excitation due to the elevated freestream disturbances levels.

A series of three pioneering hypersonic boundary layer studies in a low-disturbance environment were conducted in the NASA Langley Mach 6 Quiet Tunnel. Lachowicz *et al*¹⁸ detailed the growth of the second-mode disturbances on a flared-cone at zero degree angle of attack through uncalibrated hot-wire measurements. Doggett *et al*¹⁹ examined the disturbance growth on a flared-cone model at angle of attack. Blanchard and Selby²⁰ examined the effect of wall cooling on the disturbance growth rates. When taken together, these three experiments document the effects of angle of attack, pressure gradient, and wall cooling on the hypersonic boundary layer stability in a quiet wind tunnel. However, the spectral analysis in these studies is limited to the application of Fourier spectra. Thus only the linear region of the transition process can be quantitatively described. In this regard the quiet tunnel experiments show excellent agreement with linear stability theory, Figure 1.3.

1.1.5 Previous Computations

A computational evaluation of the NASA Langley Mach 6 Quiet Tunnel experiments was conducted by Manning.²¹ A Navier-Stokes analysis of the mean flow was compared to the experimental results and then used as the basic flow in a linear stability theory analysis (LST) of the boundary layer. Results showed good agreement with the experimental data in the early linear stages of transition. However, the agreement deteriorates in the latter nonlinear stages of the flow, and indicates the need to use more advanced prediction tools to estimate the onset of transition.

The prediction of transition to turbulence of hypersonic flows is a difficult task. A complete transition prediction tool requires a detailed knowledge of the freestream and

surface disturbance environment that provide the necessary forcing that generates, through the receptivity process, the instability waves in the boundary layer. Then the various stages in the evolution of the instabilities - linear growth, nonlinear growth, nonlinear saturation, and final breakdown - must be simulated. The advent of the parabolized stability equations (PSE)^{22,23} and direct numerical simulation (DNS)²⁴ methods has motivated computational approaches to couple the receptivity and evolution stages for hypersonic flows. From a design perspective, transition prediction tools based on the Reynolds-averaged Navier-Stokes equations,²⁵ PSE, compressible linear Navier-Stokes equations,²⁶ and DNS show promise for transition prediction. However, the code validation of these prediction methods requires that details of the underlying flow physics be more completely described. At present, the quiet tunnel experiments of Lachowicz *et al*,¹⁸ Doggett *et al*,¹⁹ and Blanchard and Selby²⁰ provide the best simulation of free-flight conditions, however the majority of these measurements were uncalibrated. It is therefore necessary for future experiments to also focus on acquiring calibrated measurements, as the validation of computational methods such as the PSE require such data.

1.2 Nonlinear Interactions

As is seen in Figure 1.3, the initial growth of the second mode that is measured in the experiment is in good agreement with linear stability theory.¹⁰ However, further downstream there is a deviation from the LST theory that is a qualitative indicator of nonlinear interactions. This deviation from LST also coincides with the appearance in the spectra of peaks centered on frequencies that are two and three times the frequency of the dominant second mode, Figure 1.4. This is further qualitative evidence that nonlinear

interactions play a dominant role in the breakdown to turbulence. Chokani²⁷ noted that the spectral amplitudes of the second-mode disturbance and its harmonics saturate as the disturbances propagate downstream, Figure 1.5.

The nonlinear interactions between disturbance modes in the boundary layer are known to arise from the convective derivative, $(\bar{u} \cdot \nabla)\bar{u}$, terms in the governing Navier-Stokes equations

$$\frac{\partial \bar{u}}{\partial t} + (\bar{u} \cdot \nabla)\bar{u} = -\frac{1}{\rho} \nabla p + \nu \nabla^2 \bar{u} \quad (1.2.1)$$

The nonlinear interactions in a hypersonic boundary layer were first quantified using the bispectral analysis technique by Kimmel and Kendall.²⁸ Hot-wire measurements on a straight walled cone in a Mach 8 conventional wind tunnel were analyzed. The resulting bispectra indicated that nonlinear phase-coupled interactions, associated with the second mode, generate the harmonic that is observed in the spectra. Chokani²⁹ analyzed the measurements on a flared cone model in a Mach 6 quiet tunnel and detected additional nonlinear phase-coupled interactions. The detected interactions included the forcing of the harmonic by the second mode, but also interactions of the second mode and its harmonic to generate a second harmonic. Additionally, during the latter stages of transition, a dominant low frequency interaction, which was speculated to be the result of modulation of the second mode and harmonic disturbances, was observed, Figure 1.6.

The digital complex demodulation technique (DCD) was used to quantify the modulation of the second-mode disturbance.³⁰ The digital complex demodulation technique revealed that the low-frequency interaction, detected in the bispectral analysis, arises from amplitude and phase modulations of the second mode, Figure 1.7. Of these

modulations, the phase modulation was observed to be the dominant energy transfer mechanism. Although useful in detecting the modulation of the second-mode disturbance, the complex digital demodulation technique is limited as only a single frequency can be analyzed at a given time.

The wavelet technique more completely describes the time and frequency character of the flow. The wavelet analysis was applied to the transitioning hypersonic boundary layer in Reference 31. The results show that in the nonlinear region, amplitude modulation of the second-mode disturbance is significant, Figure 1.8. However, the wavelet analysis adapts the time resolution to the frequency band of interest. An increased time resolution of the wavelet is obtained at the expense of reduced frequency resolution. For example, in Reference 31 the Morlet wavelet results in a frequency resolution that is comparable to the analysis frequency, $\Delta f/f \sim 3$. The frequency resolution of the wavelet is thus poor at the relatively high frequencies of the second-mode disturbance. This poor frequency resolution impedes the detection of the temporal variations associated with the dominant second mode.

1.3 Objectives

The primary objectives of this work are to develop and apply high order spectral analysis techniques to quantify the time varying and nonlinear dynamics of a transitioning hypersonic flow. The time-varying analysis technique that is introduced here does not suffer from the limitations of the previous wavelet analysis. A new technique to characterize the nonlinear dynamics is also developed. This technique is unique because it also identifies the time varying nature of nonlinear interactions, and

does not have the long time averaging associated with the previous bispectral analysis. These new analysis tools are demonstrated by application to hot-wire measurements that were previously obtained in quiet tunnel stability experiments.

APPROACH

2.1 Wind Tunnel Facilities and Experiments

2.1.1 Quiet Tunnel Technology

There is a need to obtain boundary layer stability measurements in an environment that is an accurate representation of free flight. It is known that conventional high-speed, high-Reynolds number wind tunnels generally have significant freestream disturbance fields.³² As these elevated freestream disturbance levels hinder the ability to simulate free flight conditions, the quiet wind tunnel technology was developed in order to reduce the freestream noise levels.

In the early 1990's, the NASA Langley Mach 6 quiet tunnel that is equipped with a quiet nozzle was installed in the nozzle test chamber facility, Figure 2.1.³² The nozzle test chamber is an open-jet blow-down facility with a stagnation pressure range of 100 - 200 $psia$ and stagnation temperature range of 790 - 830° R . The axisymmetric nozzle has a throat diameter of 1.00 in and exit diameter of 7.99 in . The length from the throat to exit is 39.76 in .

In order to provide a quiet freestream environment, the nozzle design incorporated several features to maintain a large region of laminar boundary layer flow along the nozzle wall. First, the nozzle surface is highly polished and manufactured to very precise tolerances. Second, the slow-expansion nozzle features a straight wall section upstream of the inflection point of the nozzle contour, Figure 2.2. The straight portion, in conjunction with the large radius of curvature of the concave section of the nozzle, inhibits the growth of Görtler vortices and hence delays transition.³³ Finally, an annular

bleed slot is located just upstream of the throat. When the bleed slot is open, the suction removes the incoming turbulent boundary layer from the settling chamber and allows a new laminar boundary layer to develop on the nozzle wall. In addition to the nozzle design, high density meshes and screens were located in the settling chamber to attenuate disturbances. The combination of these features has proven to be successful in extending the extent of laminar flow and thus creating a quiet freestream environment. The performance of this tunnel is further discussed in Reference 32.

2.1.2 Lachowicz and Blanchard Experiments

Two hypersonic boundary layer stability experiments conducted in the NASA Langley Mach 6 quiet tunnel are examined in the present research. Lachowicz and Chokani³³ measured the transitioning boundary layer over a flared-cone model, where the radius of curvature of the flared region is 93.071in and the length of the 5 degree half angle cone section is 10in, Figure 2.3. This model is designated 93-10. The cone model was thin walled, and measurements were obtained under adiabatic wall conditions. Blanchard and Selby²⁰ conducted their experiments using the 91-6 flared-cone model. The radius of curvature of the flared region is 91.44in and the length of the straight region is 6in, Figure 2.4. Adiabatic and cooled wall conditions were examined for the 91-6 cone; for the cooled case the wall temperature was 465°R. These two experiments thus allow the effects of pressure gradient and wall cooling on the boundary layer stability to be examined.

Single point hot-wire measurements were obtained at several streamwise locations spaced at 0.25in intervals. At each streamwise location, the measurements were

taken at the location of maximum disturbance energy in the boundary layer. Table 2.1 lists the streamwise locations and corresponding stability Reynolds numbers for the 91-6 and 93-10 models. The two experiments were conducted at a stagnation temperature and total pressure of $810^{\circ}R \pm 3^{\circ}R$ and $130psia \pm 2psia$ respectively, and the free-stream Mach number is 5.91 ± 0.08 . These test conditions correspond to a unit Reynolds number of $2.82 \times 10^6/ft$.

A $2.5\mu m$ platinum-rhodium (10%) hot-wire operated by a constant voltage anemometer (CVA) was the primary measurement device. A hot-wire in a high-speed flow responds to a mixed mode of mass flux and total temperature³⁴

$$\frac{e'}{E} = S_{\rho u} \frac{(\rho u)'}{(\overline{\rho u})} + S_{T_o} \frac{T_o'}{\overline{T_o}} \quad (2.1.1)$$

At high overheat, the hot-wire becomes primarily sensitive to mass flux³³

$$\frac{e'}{E} \approx S_{\rho u} \frac{(\rho u)'}{(\overline{\rho u})} \quad (2.1.2)$$

The anemometer output was passed through an anti-aliasing, low-pass filter set at 1 MHz, and then sampled at 2 MHz using a digital storage oscilloscope.

2.1.3 Constant Voltage Anemometer

The constant voltage anemometer (CVA) was patented by Sarma³⁵ in 1991 and introduced as an alternative to the constant current (CCA) and constant temperature (CTA) anemometers. The CVA system has several advantages over the CCA and CTA; these include a larger bandwidth, higher signal-to-noise ratio, and relatively smaller insensitivity to the cable length. It was the availability of the CVA that enabled the

experiments of Lachowicz and Blanchard, as attempts to measure the naturally-occurring, high-frequency boundary layer disturbances with CCA and CTA proved futile.¹⁸

Similar to other thermal anemometry systems, the CVA operates by measuring the convective heat loss from a sensing element in a fluid flow. The basic CVA circuit is shown in Figure 2.5a³⁶ and consists of three main components: a stable DC reference voltage, an inverted operational amplifier, and a T-resistor network (R_F , R_2 , and R_W). The voltage across the hot-wire can be written as

$$V_W = \frac{R_F}{R_1} V_1 \quad (2.1.3)$$

From this equation, it is evident that the wire voltage, V_W , is constant for a given V_1 and therefore is independent of the hot-wire resistance, R_W . It is this characteristic that gives the CVA its name. A change in the convective heat transfer from the hot-wire alters the hot-wire resistance R_W , and thus changes the current through the hot-wire, I_W . By applying Kirchoff's current law at the node of the T-resistor network:

$$E + e' = \left(1 + \frac{R_2}{R_F}\right) V_W + R_2 I_W + R_2 i'_W \quad (2.1.4)$$

For a given wire voltage, a perturbation in the output voltage is linearly proportional to the fluctuations in the wire current. For a large R_2 , small changes in the wire current appear as large changes in output voltage.

In the compensated CVA, Figure 2.5b, the resistor R_2 is replaced by a resistor-capacitor combination whose function is to increase the frequency response of the anemometer. In the absence of the RC-combination, the classical first order hot-wire response

$$e'(t) = e'_w(t) + M_{CVA} \frac{de'_w(t)}{dt} \quad (2.1.5)$$

that arises from the thermal inertia of the wire determines the anemometer frequency response. Sarma has derived the anemometer transfer function

$$\frac{e'}{u}(s) = \frac{\left(\frac{R_2}{R_w}\right) I_w}{\frac{s^2}{\omega_n^2} + \frac{1}{\omega_n^2} \left(\frac{1}{T_c} + \frac{R_w}{R_d} 2\pi f_i\right) s + 1} \frac{(1 + T_C s)}{(1 + M_{CVA} s)} b' \quad (2.1.6)$$

The hot-wire time constant, M_{CVA} , that limits the frequency response, appears as a pole in the transfer function. The hardware time constant, T_C

$$T_C = \frac{CR_a R_b}{R_2} \quad (2.1.7)$$

appears as a zero, and can be selected to cancel the pole in the transfer function. However, such an approach is time consuming as the hot-wire time constant is a function of both wire overheat and Reynolds number³⁷

$$M_{CVA} = \frac{1 + a_w}{1 + 2a_w} \frac{d^2}{4} \frac{\rho_w c_w}{k_a} \frac{1}{A + B\sqrt{Re_w}} \quad (2.1.8)$$

Figure 2.6 shows the variation of the hot-wire time constant, measured in a low-speed flow at various wire Reynolds numbers and overheats. It is more productive to use partial compensation whereby measurements are obtained with a fixed T_C

$$e'_{rav}(t) = e'_w(t) + T_C \frac{de'_w(t)}{dt} \quad (2.1.9)$$

And then in software, correct for the mismatch of T_C and M_{CVA} using

$$e'_{corr}(t) = e'_{rav}(t) \left[\frac{1 + M_{CVA} s}{1 + T_C s} \right] \quad (2.1.10)$$

to obtain:

$$e'_{corr}(t) = e'_{raw}(t) + M_{CVA} \frac{de'_{raw}(t)}{dt} - T_C \frac{de'_{corr}(t)}{dt} \quad (2.1.11)$$

The resultant frequency response can then be several orders of magnitude larger than that of the hot-wire as it is limited by only the terms in the first bracket of equation 2.1.6.

The CVAs used in the work of Lachowicz and Blanchard had bandwidths of 350kHz and 400kHz respectively. Although the amplitude response is flat up to the stated bandwidths, the phase response is flat to a lower frequency. This limited phase response may play a role in the interpretation of the results of high-order spectral analysis presented below.

2.2 High Order Spectral Analysis

Time series signals, which are characterized as having a random or a high degree of variability, can more conveniently be analyzed in the frequency domain.³⁸ The decomposition of a time signal into harmonic components of various frequencies is often expressed as the power spectrum density (PSD)

$$P_{xx}(f) = \langle S(f)S^*(f) \rangle \quad (2.2.1)$$

where $S(f)$ is the finite Fourier transform of the time series $s(t)$

$$S(f) = \lim_{T \rightarrow \infty} \int_{-T}^T s(t) e^{-i2\pi ft} dt \quad (2.2.2)$$

The power spectrum estimates the distribution of power among the frequency components. The PSD of the hot-wire measurements in a laminar hypersonic boundary layer undergoing transition can be used to infer the growth or decay of the second mode. However, multiple peaks (or modes) are observed in the PSD. It is known that if modes

are coupled through a nonlinear interaction mechanism, a phase coherence will exist among them. The power spectrum does not preserve phase information, and thus we are motivated to use high order spectral analysis techniques; in this work the bispectrum is used to retain phase information. The PSD and bispectrum however employ the finite Fourier transform that is a statistical average over a relatively long duration. Under this condition, time local information, that is transient events, cannot be detected. However, these are known to be characteristic of the breakdown to turbulence. Thus, in the present work, we develop the short time Fourier transform (STFT) to characterize the transient events in the distribution of power and the STFT bispectrum to identify transient nonlinear interactions.

2.2.1 Short-time Fourier Transform

The power spectrum density cannot detect any transients in the distribution of power due to the relatively long analysis time. Hence, the STFT was developed in order to realize the time varying nature of the power spectrum of a signal. The STFT is obtained by sliding a running analysis window along the time series and is defined as³⁹

$$G_s(t, f) = \int_{t'} [s(t') \gamma^*(t' - t)] e^{-i2\pi f t'} dt' \quad (2.2.3)$$

This is graphically illustrated as steps 1 and 2 in Figure 2.7. The relatively short time duration of the analysis window that is centered on the analysis time, t , acts to mask out any part of the time series that is not in the local vicinity of the window, step 1. The fast Fourier transform of the windowed time series yields a time local FFT, step 2. Thus the STFT can be thought of as the local Fourier transform of the original time series at time t . For discretely sampled data, the next localized FFT is obtained by translating the analysis

window $\gamma^*(t'-t)$ from time t to time $(t + \Delta t')$. If there is no overlapping and the window length is N_{FFT} points, then the time resolution of the STFT is

$$\Delta t = \Delta t' (N_{FFT} - 1) \quad (2.2.4)$$

where

$$\Delta t' = 1 / f_s \quad (2.2.5)$$

The uncertainty principle⁴⁰

$$\Delta \omega \cdot \Delta t \geq \frac{1}{2} \quad (2.2.6)$$

indicates that there is a tradeoff between the frequency and time resolutions. That is the use of a narrow analysis window results in excellent time resolution and poor frequency resolution. Conversely, good frequency resolution requires the use of a long analysis window, which therefore results in poor time resolution.

2.2.2 Bispectrum

The auto-bicoherence spectrum (or bispectrum) provides a measure of the nonlinear (quadratic) phase coupling in the time series. The bispectrum in the present work is defined as

$$b^2(f_1, f_2) = \frac{|S^*(f_1 + f_2)S(f_1)S(f_2)|^2}{|S(f_1)S(f_2)|^2 |S(f_1 + f_2)|^2} \quad (2.2.7)$$

where $S(f)$ is the Fourier transform of the N_{FFT} data points in the signal $s(t')$. The bispectrum takes on values between 0 and 1 because of the normalization with the Fourier transform. Usually, the bispectrum is normalized by the power spectrum,

$$b^2(f_1, f_2) = \frac{|S^*(f_1 + f_2)S(f_1)S(f_2)|^2}{P_{xx}(f_1)P_{xx}(f_2)P_{xx}(f_1 + f_2)} \quad (2.2.8)$$

However this definition does not necessarily bound values of the bispectrum between 0 and 1 for signals of short time duration.⁴¹ However the use of equation 2.2.8 requires less computer memory storage and lower computation costs than equation 2.2.7. A bispectrum value of one indicates that the triplet of waves with frequencies f_1 , f_2 , and $f_1 + f_2$ are quadratically phase coupled. More specifically, the three frequency components, f_1 , f_2 , and $f = f_1 + f_2$ satisfy the phase relation

$$\angle f = \angle f_1 + \angle f_2 \quad (2.2.9)$$

Bispectrum values between zero and one indicate partial coupling. At near zero values of the bispectrum, the three components are statistically independent and of random phase.

The nonlinear interactions identified by the bispectrum are averaged over the relatively long analysis time. The length of the analysis time, N_{FFT} , is shorter than the entire time series of N points. Therefore the (N/N_{FFT}) number of bispectra are ensemble averaged to yield a single auto-bispectrum, which we term here the Fourier bispectrum

$$b_F^2(f_1, f_2) = \frac{\langle |S^*(f_1 + f_2)S(f_1)S(f_2)|^2 \rangle}{\langle |S(f_1)S(f_2)|^2 \rangle \langle |S(f_1 + f_2)|^2 \rangle} \quad (2.2.10)$$

The symmetry properties of the bispectrum and Nyquist frequency limits allow bispectrum to be displayed over the triangular region that is bounded by $f_2 = 0$, $f_1 = f_2$, and $f_1 + f_2 = f_N$ in the (f_1, f_2) plane, Figure 2.8.

2.2.3 STFT Bispectrum

One limitation of the Fourier bispectrum is that it spans a relatively long analysis time and therefore it averages out any transient nonlinear phase coupled interactions that may occur with the analysis time. Recently, the wavelet bicoherence, that combines the time-frequency analysis of the wavelet and nonlinear interaction detection of the bispectrum, has been proposed for the analysis of plasma turbulence.^{42,43} However, Chokani observed that the wavelet analysis technique is poorly suited for analysis of hypersonic laminar boundary layers. This is because the frequency resolution of the wavelet is poor at the high frequencies of second mode instabilities. This motivated the author to develop the STFT bispectrum as an alternative to the wavelet bispectrum to detect transient nonlinear interactions. The STFT bispectrum can be written by substituting equation 2.2.3 into 2.2.10 and integrating over the short time interval of the analysis window

$$b_{STFT}^2(T, f_1, f_2) = \frac{\frac{1}{T} \int_T |G_s^*(t, f_1 + f_2) G_s(t, f_1) G_s(t, f_2)|^2 dt}{\frac{1}{T^2} \int_T |G_s(t, f_1) G_s(t, f_2)|^2 dt \int_T |G_s(t, f_1 + f_2)|^2 dt} \quad (2.2.11)$$

A comparison of equations 2.2.10 and 2.2.11 shows that whereas the Fourier bispectrum averages out nonlinear interaction mechanisms over a relatively long analysis time, the STFT bispectrum is integrated over a smaller analysis time T . The computation of the STFT bispectrum is graphically illustrated in Figure 2.9.

The summed bispectrum and total bispectrum are convenient parameters to help in the interpretation of the STFT bispectrum.⁴² The summed bispectrum, that is taken along lines of constant $f = f_1 + f_2$

$$b_s^2(T, f) = \frac{1}{n(f)} \sum_{f=f_1+f_2} b_{STFT}^2(T, f_1, f_2) \quad (2.2.12)$$

is a measure of all the quadratic nonlinear interactions at frequency f over the short time interval. The total bispectrum

$$b_T^2(T) = \frac{1}{n(f)} \sum_f b_s^2(T, f) \quad (2.2.13)$$

provides an indication of the degree of intermittent behavior during the short time interval.

When calculating the STFT bispectrum, the following parameters are of interest. For the case where there is no overlapping of segments in the time or frequency domain, the following relation is obtained

$$\frac{N}{N_{FFT} N_b N_E} = 1 \quad (2.2.14)$$

The number of points N_{FFT} determines the frequency resolution, $\Delta f = F_s / (N_{FFT} - 1)$. The ratio (N/N_{FFT}) determines the number of segments in the STFT, $M = N/N_{FFT}$. The time resolution (that is, the time between each segment), Δt , is determined in equation 2.2.4. Thus, once the STFT has been calculated, it is sub-divided into N_b segments of N_E time local FFTs over which the STFT bispectra is computed. The time duration covered by the STFT bispectra is

$$\Delta T = \Delta t(N_E - 1) \quad (2.2.15)$$

It is noted that if $N_b = 1$, then the STFT bispectra is identically the Fourier bispectra.

RESULTS AND DISCUSSION

The Results and Discussion section is arranged as follows. First, the STFT analysis is presented to examine the time varying characteristics of the second mode and its harmonics. These characteristics are quantified using the modulation indices, and also qualitatively described using the high-order statistical moments of skewness and kurtosis. Next the nonlinear interactions are quantified using the Fourier bispectrum. This analysis shows that harmonic nonlinear interactions are the primary energy transfer mechanisms for the long time-averaged dynamics. The results of the STFT bispectrum, that are then presented, highlight the role of non-harmonic interactions in the observed transient nonlinear mechanisms. In the above analyses, the three previously described test cases are used to describe the effects of wall cooling and pressure gradient on the time varying and/or nonlinear interactions.

3.1 Short-time Fourier Transform

For the STFT calculations, the number of points used to calculate the Fourier transform is $N_{FFT} = 256$; therefore, the temporal resolution is $\Delta t = 0.1275ms$, and the frequency resolution is $\Delta f = 7.84kHz$.

3.1.1 Spectrogram

The contour plots of the magnitude of the STFT calculated from the hot-wire measurements on the adiabatic 91-6 (baseline) model are shown for six measurement

locations in Figure 3.1. At $R = 1609$, the second-mode disturbance is not discernible. From $R = 1680$ to 1749 , the second-mode is clearly detected and is centered on the frequency of 289kHz . Over the range $1680 < R < 1749$, the change in the intensity of the contour along $f = 289\text{kHz}$ indicates that the second-mode is weakly modulated (Figures 3.1b and 3.1c). For $R \geq 1815$, the first and second harmonics ($f = 578\text{kHz}$ and 867kHz , respectively) of the second-mode are also detected. Over this range, the weak modulation of the harmonics and a stronger modulation of the second-mode is also observed. The modulation of the harmonics was not observed in the previous wavelet analysis due to its poor frequency resolution.³¹ The frequency resolution in the STFT is 15.625kHz ; this resolution is 14 times smaller than the frequency resolution at the wavelet scale of the second-mode in the wavelet analysis. Furthermore, because of the limited bandwidth, the wavelet analysis cannot resolve the wavelet scales associated with the harmonic frequencies. However, the time and frequency representation of the STFT clearly reveals the transient nature of both the second-mode disturbance and its harmonics.

The effect of wall cooling on the second mode and its harmonics is examined in Figure 3.2. These plots of the STFT illustrate the destabilizing effect of wall cooling on the boundary layer stability. Due to wall cooling, the second-mode appears at a more upstream station, $R = 1609$ (Figure 3.2a), compared with $R = 1680$ for the baseline case (Figure 3.1b). The second-mode is centered at a higher frequency, around 306kHz . This shift to a higher frequency occurs on account of the “tuning” of the frequency of the second-mode to the boundary layer thickness. Wall cooling in a hypersonic boundary layer flow reduces the boundary layer thickness and consequently the second mode frequency is increased. A well-defined first harmonic for the cooled wall is detected at R

= 1749 (Figure 3.2c); *c.f.* $R = 1815$ for the baseline case (Figure 3.1d). A feature common to the baseline and cooled wall cases is the observed modulation of the second-mode frequency and its harmonic. However, as the second mode and harmonic first appear more upstream than in the baseline case (Figure 3.2f), the initial breakdown to turbulence at $R = 1940$, as determined from the filling in of the spectra, is observed. This is illustrative of the destabilizing effect of wall cooling.

The effect of the pressure gradient on the transient behavior can be observed by comparing the STFT results for the adiabatic 93-10 model presented in Figure 3.3 with the baseline case. At $R = 1879$, Figure 3.1e and 3.3a, the 93-10 model which has a smaller adverse pressure gradient, shows only the presence of a second-mode disturbance, whereas the second-mode and its harmonics are observed in the baseline case. It is also noteworthy that the second-mode occurs at a lower frequency on the 93-10 model, centered on $222kHz$, compared to $289kHz$ on the baseline case. For the 93-10 model, the boundary layer thickness is reduced less on the flare of the model because of the smaller adverse pressure gradient; this results in the lower frequency. At $R = 1940$, Figure 3.1f and 3.2b, the first harmonic is weakly detected on the 93-10 model, whereas the first and second harmonics are clearly observed on the baseline case. It is only further downstream at $R = 2058$ and 2114 that a harmonic clearly develops on the 93-10 model. At the most downstream station on the 93-10 model the STFT shows that spectral broadening is occurring without the clear appearance of a second harmonic as is observed at the most downstream station on the 91-6 model.

The STFT analysis clearly shows the time varying behavior of the second mode and its harmonics. Overall, the effect of wall cooling is more pronounced than the effect of adverse pressure gradient on this time varying behavior.

3.1.2 Amplitude and Phase Modulations

The amplitude and phase modulation of the second-mode disturbance can be inferred from the STFT. The time-series of the amplitude and phase of the STFT are extracted by taking a “slice” at the frequency of the second-mode, $f = f_o$. This is graphically illustrated in Figure 3.4. Since the STFT $G_s(t, f)$ has real and imaginary parts, its amplitude and phase are written as

$$|G_s(t, f)| = \sqrt{\Re^2(t) + \Im^2(t)} \quad (3.1.1)$$

$$\angle G_s(t, f) = \tan^{-1} \left(\frac{\Im(t)}{\Re(t)} \right) \quad (3.1.2)$$

The amplitude and phase of $G_s(t, f_o)$ at three measurement locations are shown in Figure 3.5 for the baseline case. At $R = 1680$ there is little amplitude modulation, however, the amplitude modulation becomes more marked as R increases (Figures 3.5a-c). The phase modulation shows strong, regular variations of $\pm\pi/2$ rad throughout the measurement range for the baseline case (Figures 3.5d-f).

The effect of wall cooling on the amplitude and phase of $G_s(t, f_o)$ is shown in Figures 3.6a-c for the three measurement locations, $R = 1680, 1815$ and 1940 . At $R = 1680$, the amplitude modulation is observed to be greater for this cooled wall case, Figure

3.6a than the baseline case, Figure 3.5a. However, for the cooled wall case, while the amplitude modulation is also clear at $R = 1815$, the amplitude modulation at the most downstream station ($R = 1940$) is reduced due to the initial breakdown to turbulence of the transitioning flow. The phase modulation examined in Figures 3.6d-f again shows strong, regular variations of $\pm\pi/2$ rad throughout the measurement range as observed in the baseline case.

The amplitude and phase of $G_s(t, f_o)$ for the 93-10 case is shown in Figure 3.7. The increase in the amplitude modulations from $R = 1879$ to $R = 2114$ (Figures 3.7a-c) closely resembles the behavior in the baseline case for $R = 1680$ to $R = 1815$ (Figures 3.5a-b). Hence, there is little effect of pressure gradient on the amplitude modulation. The phase modulation (Figure 3.7d-e) exhibits the same strong, regular variations that are observed for both the baseline and cooled wall cases.

The amplitude and phase modulation indices (α and β , respectively) that characterize the nonlinear interactions are calculated using the expressions³⁰

$$\alpha = \frac{\sqrt{\langle [|G_s(t, f)| - \langle |G_s(t, f)| \rangle]^2 \rangle}}{\langle |G_s(t, f)| \rangle} \quad (3.1.3)$$

$$\beta = \sqrt{\langle \angle G_s(t, f)^2 \rangle} \quad (3.1.4)$$

Although the STFT plots in Figures 3.1-3.3 were calculated using only 2^{13} data points, the entire time series of 2^{17} data points of the hot-wire measurements are used to compute the modulation indices. The effects of the wall cooling and adverse pressure gradient are examined through the downstream evolution of the modulation indices in Figure 3.8. For the baseline case, there is little variation in the amplitude modulation over the upstream

range of measurements, $R < 1766$, Figure 3.8a. Downstream of $R = 1766$, α gradually decreases. The effect of wall cooling is to cause a decrease in α at a more upstream station, $R = 1645$, compared to $R = 1766$ for the baseline, Figure 3.8a. For the cooled wall, α changes from its nearly constant value of 0.65 to a minimum value of 0.3 at $R = 1847$; in contrast for the baseline case, α is initially at 0.65 and decreases only to a value of 0.5 at $R = 1910$. For the cooled wall downstream of $R = 1847$, there is a sharp increase in α . The amplitude modulation for 93-10 case shows no discernible variation over the range of measurement and indicates that there is little effect of this pressure gradient on the non-linear interactions, Figure 3.8a.

While α shows small variation due to pressure gradient or large changes due to wall cooling, there is little effect on β . It remains essentially constant and at a high value, ≈ 0.9 , throughout the measurement range for all cases (Figure 3.8b).

The ratio α/β is presented in Figure 3.8c. Over the measurement range, α/β is less than unity for all three cases indicating the more dominant role of phase modulation in the energy transfer mechanisms. However, for the cooled wall case, it is observed that during the latter stages of transition, the relative role of amplitude modulation becomes more important. These observations regarding the relative role of the amplitude and phase modulations are in agreement with results from the digital complex demodulation technique.³⁰

3.1.3 Kurtosis and Skewness

The effects of the pressure gradient and wall cooling on the kurtosis and skewness are shown in Figure 3.9. The kurtosis and skewness are computed from the time-series of

the magnitude of the STFT at the frequency of the second-mode. The kurtosis is a normalized fourth moment, which has a value of three for a Gaussian distribution

$$K = \frac{1}{N\sigma^4} \sum_{n=1}^N \left(|G_s(t_n, f)| - \mu \right)^4 \quad (3.1.5)$$

The skewness is a normalized third moment, and is zero for a Gaussian distribution

$$\Lambda = \frac{1}{N\sigma^3} \sum_{n=1}^N \left(|G_s(t_n, f)| - \mu \right)^3 \quad (3.1.6)$$

For all three cases in general, the value of the kurtosis progressively decreases with increasing Reynolds number, Figure 3.9a. However the crossing of the value of three occurs most upstream at $R = 1715$ for the cooled wall case, at $R = 1847$ for the baseline case, and at $R = 2029$ for the 93-10 case. As the kurtosis is a qualitative indicator of nonlinearity, this result confirms the destabilizing role of both adverse pressure gradient, comparing the 93-10 result and the baseline, and of wall cooling, comparing the baseline and 91-6 cooled cases. In the previous section we have also observed that amplitude modulation plays an increasingly significant role with wall cooling. In the kurtosis we also observe an additional crossing of the value of three for the cooled wall case, at $R \cong 1900$. This coincides with the increase in the amplitude modulation index.

The variation in the skewness also shows a correlation with the evolution of the amplitude modulation. In Figure 3.9b for the baseline and 93-10 case, the skewness monotonically decreases from a value of two towards zero with increasing Reynolds number. As is previously seen for these two cases, there is only a small variation in amplitude modulation indices. However for the wall cooled case, the skewness decreases more rapidly, and is negative over the range $1750 < R < 1860$. The range of negative skewness coincides with the sharp decrease in the amplitude modulation index. The

subsequent sharp increase in the skewness coincides with increasingly pronounced role of amplitude modulation.

3.1.4 Harmonic Frequency Band

The time-series of the amplitude and phase of the first harmonic ($f = 2f_o$) were also extracted from the STFT using the previously described procedure. The amplitude and phase of $G_s(t, 2f_o)$ for the baseline case is shown in Figure 3.10, for three stations, $R = 1815, 1879$ and 1940 . The variation in the amplitude at $R = 1815$ for the baseline case has very low mean and fluctuating values, Figure 3.10a. At the more downstream locations, the mean value is increased, Figures. 3.10b and 3.7c. For each R location, the phase modulation shows strong, regular variations over $\pm\pi/2$ rad, Figure 3.10d-f. Therefore, the downstream evolution of the harmonic is similar to that of the second-mode observed in Figure 3.5.

At $R = 1815$ for the cooled wall case, Figure 3.11a, the mean and fluctuating values of the amplitude are larger than the baseline case and exhibit an intermittent behavior. However, as R increases for the cooled wall case, the mean and fluctuating values of the amplitude decrease, Figure 3.11b-c. The intermittent behavior also appears to become more pronounced at the downstream stations. The low values of the amplitude of $G_s(t, 2f_o)$ at the $R = 1940$ station for the cooled case are associated with the transfer of energy from harmonic frequency and an initial breakdown to turbulence. Again, the phase modulation, Figure 3.11d-f, shows a regular variation at each measured station.

The effect of the pressure gradient is examined in Figure 3.12a-c. The amplitude of $G_s(t, 2f_o)$ is initially low and only shows moderate increase at the downstream

locations. The levels at the two downstream locations are, however, slightly higher than that of the baseline case. The phase modulation has the same regular variations of the previous cases.

Amplitude and phase modulation indices of $G_s(t, 2f_0)$ are shown in Figure 3.13. The amplitude modulation indices, Figure 3.13a, show a similar trend to that of the second mode, Figure 3.8a. For the baseline case, α decreases with increasing R . For the cooled wall, there is a small initial rise upstream of $R = 1750$, downstream of which the amplitude modulation index decreases. The amplitude modulation continues to decrease until $R = 1850$, where there is then a sharp increase. It is noted that the minimum in the amplitude modulation for both the second mode and the harmonic of the cooled wall case occur at approximately the same location. For the weaker pressure gradient case 93-10, the amplitude modulation is essentially constant and is at a lower level than the baseline and cooled models.

The phase modulation of $G_s(t, 2f_0)$ remains at a constant value of $\beta = 0.9$ for all three cases over the range of measurement, Figure 3.13b. This trend is similar to that observed for the second-mode, Figure 3.8b. However the relative role of the amplitude and phase modulation differs for the harmonic. In Figure 3.13c, it is observed that for the cooled wall case the amplitude modulation is more dominant ($\alpha/\beta > 1$) for the range $1700 < R < 1800$ and $1900 < R < 2000$. This is in contrast to the second mode in which the phase modulation is always dominant, Figure 3.8c. Similar to the second mode behavior, the ratio α/β indicates that the phase modulation is more dominant for the harmonic in the baseline and 93-10 cases, Figure 3.13c.

The kurtosis and skewness of the magnitude of $G_s(t, 2f_o)$ for the three cases are examined in Figure 3.14. In general, the trends are similar to those of the second-mode, Figure 3.9a; however, the overall levels are higher for the harmonic frequency. Each of the three cases are initially well above three and then decrease quickly. For the baseline and pressure gradient case, the kurtosis decrease to a value of three and then stays relatively constant. The kurtosis for the cooled wall case reaches a minimum value of three at $R = 1815$ and immediately begins to rise to a high value. The skewness (Figure 3.14b) exhibits many of the same features as the skewness for the second-mode (Figure 3.9b), however, the initial and minimum levels are higher for the harmonic and do not go below zero. The skewness for both the baseline and pressure gradient case decrease as R increases. The cooled cone model shows a minimum skewness at $R = 1815$ for both the harmonic and second mode. For $R > 1815$, the skewness increases.

Overall, the STFT is effective in identifying the transient behavior of the harmonic of the second mode. Such behavior cannot be observed with the wavelet analysis technique due to its poor bandwidth resolution. The observed transient behavior of the harmonic occurs at a more downstream location than the onset of the second mode's transient behavior.

3.2 Fourier Bispectrum

For the PSD and Fourier bispectrum calculations, the number of points used to calculate the Fourier transform is $N_{FFT} = 256$ and the number of ensembles is $N_E = 512$, which yields a frequency resolution of $\Delta f = 7.84 kHz$. It should be noted that although a

higher frequency resolution could be obtained for the PSD, this lower resolution was used to ensure a consistent comparison with the bispectrum.

In the bispectrum phase information is retained. However, as the phase response of the CVA is not constant over the entire frequency range of interest (Figure 2.8b), only the streamwise evolution of a given nonlinear interaction can be quantitatively examined. Also, it is possible to only qualitatively compare different nonlinear interactions at a given measurement location or as they evolve downstream.

3.2.1 Baseline

The baseline case, 91-6 adiabatic cone, is first examined. The PSD at stations $R = 1609, 1680, 1749, 1815, 1879$, and 1940 are shown in Figure 3.15. For clarity the subsequent spectra are shifted up one decade. The streamwise evolution of the second mode that is centered on $f_o = 289kHz$ is seen. At the most upstream station, $R = 1609$, the second mode is barely distinguishable from the background noise. Further downstream at $R \geq 1680$, the amplitude of the second mode increases and a spectral broadening of its sidebands is observed. For $R \geq 1815$, the appearance of peaks centered on the harmonic frequencies of $2f_o$ and $3f_o$ are a qualitative indicator of nonlinear interactions.

The corresponding plots of the Fourier bispectrum are shown in Figure 3.16. In these plots, the diagonal dashed lines denote harmonic nonlinear interactions; that is the frequency pair (f_1, f_2) satisfies the relation $f_1 + f_2 = f_o, 2f_o$, or $3f_o$. Recall also that the Fourier bicoherence is averaged in the sense that a relatively long time record is analyzed. The plots of the Fourier bicoherence at $R = 1609$ and 1680 , Figures 3.16a and

3.16b, show no significant levels. At $R = 1749$, Figure 3.16c, a peak is observed at $(f_o, \delta f)$, where $\delta f \approx 23kHz$. This interaction peak may be interpreted as

$$f_o - (f_o - \delta f) \rightarrow \delta f \quad (3.2.1)$$

$$(f_o + \delta f) - f_o \rightarrow \delta f \quad (3.2.2)$$

which denotes interactions of the second mode and its sidebands. At $R = 1815$, Figure 3.16d, additional interaction peaks are observed at (f_o, f_o) , $(2f_o, f_o)$, and $(2f_o, \delta f)$. The interaction peak (f_o, f_o) indicates that the fundamental couples with itself to force the growth of the first harmonic, $2f_o$

$$f_o + f_o \rightarrow 2f_o \quad (3.2.3)$$

A similar interpretation of the interaction peak $(2f_o, f_o)$ explains the presence of the second harmonic that is observed in the Fourier spectrum. The interaction peak $(2f_o, \delta f)$ indicates the interaction of the harmonic with its sidebands. At $R = 1879$ and $R = 1940$, Figure 3.16e and 3.16f, additional peaks include $(\delta f, \delta f)$ and $(3f_o, \delta f)$. The interaction peak $(3f_o, \delta f)$ indicates the interaction of the second harmonic with its sidebands that are similar to the sideband interactions associated with peak $(2f_o, \delta f)$. The interaction peak $(\delta f, \delta f)$ indicates the low frequency modulation of the second mode. Note also that the interaction peak $(f_o, \delta f)$, that is also observed at $R = 1749$ and 1815, is broader.

3.2.2 Effect of Wall Cooling

A comparison of the PSD for the cooled wall, Figure 3.17, and baseline case, Figure 3.15, shows the earlier appearance of the second mode at $f_o = 306kHz$ (compare to the spectra at $R = 1609$) and the harmonic (compare to the spectra at $R = 1680$). The

streamwise evolution of the spectral peaks at $f_o = 306kHz$, shows that while the amplitudes increase significantly from $R = 1609 - 1749$ for both the adiabatic and cooled wall cases, for $R = 1749 - 1879$ the increase is relatively small for the cooled wall case and relatively large for the adiabatic wall. This apparent decrease in the growth rate for the cooled wall is a qualitative indicator of the stronger nonlinear interactions in the cooled wall case. For $R = 1940$, the spectral peaks associated with the second-mode and the harmonic frequencies are slightly reduced in amplitude and begin to broaden significantly. This is indicative of the beginning of the breakdown to turbulent flow for the cooled wall case.

The stronger nonlinear interactions suggested by the power spectra for the cooled wall case are confirmed in the comparison of the plots of the Fourier bispectrum, Figure 3.18 for the cooled wall and Figure 3.16 for the adiabatic wall. The multiple interaction peaks $(f_o, \delta f)$, (f_o, f_o) , $(2f_o, \delta f)$, and $(2f_o, f_o)$ that are seen at $R = 1749$ for the cooled wall, Figure 3.18d, are not seen until further downstream at $R = 1879$ for the adiabatic wall flow, Figure 3.16e. At $R = 1879$ for the cooled wall, Figure 3.18f, some of the interaction peaks are less pronounced since the boundary layer flow is in the initial stages of breakdown to turbulent flow.

3.2.3 Effect of Pressure Gradient

The effect of pressure gradient can be seen in the power spectra in Figure 3.19. At $R = 1879$, only the second mode centered on $f_o = 222kHz$ is observed, where as for the baseline case the first and second harmonics are seen at $R = 1879$ for the baseline case. This is a qualitative indication that the more adverse pressure gradient in the baseline

case promotes weaker nonlinear interactions. This is confirmed in the corresponding bispectrum in Figure 3.20. At $R = 1879$, no significant quadratic nonlinear interaction peaks are noted in the bispectrum, Figure 3.20a, where as several peaks are seen at $R = 1879$ for the baseline case, Figure 3.16e. At $R = 2114$, Figure 3.20e, additional peaks are observed at $(3f_o, \delta f)$, $(3f_o, f_o)$, and $(2f_o, 2f_o)$. These peaks, that are associated with the third harmonic, are observed for the 93-10 case since the frequency of the second mode is lower and its resulting third harmonic ($888kHz$) is less than the Nyquist frequency, $F_N = 1000kHz$.

Overall the Fourier bispectrum quantifies the nonlinear interactions that explain the presence of harmonics in the spectra. A low frequency nonlinear interaction that may be associated with previously observed amplitude and phase modulations is also observed. The effect of wall cooling is to make these interactions more pronounced.

3.3 STFT Bispectrum

For the STFT bispectral analysis the number of points used to calculate the Fourier transform is $N_{FFT} = 256$, the number of STFT bispectrum is $N_b = 7$, and the number of ensembles for each STFT bispectra is $N_E = 73$. These yield a temporal resolution in the STFT of $\Delta t = 0.1275ms$ and a time duration in the STFT bispectra of $\Delta T = 9.18ms$. In the discussion below the time duration in the STFT bispectrum is referred to as a segment, and seven ($N_b = 7$) segments cover over the analysis period. The frequency resolution is $\Delta f = 7.84kHz$. The same frequency resolution is used in the Fourier spectra and bispectra so that its' interpretation in relation to the STFT bispectra is unambiguous.

In the subsequent figures, the total bispectrum is shown in part a), the summed bispectrum in parts b) and f), the STFT bispectrum in parts c) and g), and, for sake of completeness, the corresponding STFT and time series segments in parts d), h) and e), i), respectively. The time histories of the interaction peaks $(\delta f, \delta f)$, $(\delta f, f_o)$, (f_o, f_o) , and $(2f_o, f_o)$ that are measured from the STFT bispectrum are also shown in part a).

3.3.1 Baseline

The transient nonlinear interactions for the baseline case are examined in Figures 3.21 - 3.32. The total bicoherence versus time at $R = 1609$, Figures 3.21a and 3.22a, show that there is a peak in $b_r^2(T)$ at segment [5], but it is otherwise at a low level for the other segments. This peak indicates that there are transient nonlinear interactions. The corresponding summed bicoherence at segment [5], Figure 3.22b, shows that the transient event is associated with nonlinear interactions that occur in the frequency bands 100-190, 210-290 and 300-350kHz. The plot of the STFT bicoherence in Figure 3.22c shows that the nonlinear interactions lie in diagonal $(f_1 + f_2)$ bands that are distinct and different from the harmonic interactions. A comparison of the Fourier bicoherence, Figure 3.16a, and the STFT bicoherence plots at segments [1], [3], [5] and [7], Figures 3.21c, 3.21g, 3.22c and 3.22g, shows that while the Fourier bicoherence averages out the transient events, the STFT bicoherence successfully identifies these.

The nonlinear interactions at $R = 1680$ are similar to $R = 1609$ and are presented in Figures 3.23 and 3.24. The levels of the individual interactions peaks, Figures 3.23a and 3.24, were invariant from $R = 1609$ to $R = 1680$, indicating that the transient nonlinear interactions associated with these pairs remain insignificant. The variation in

total bicoherence for $R = 1680$ also shows behavior similar to $R = 1609$ in that it remains flat except for a peak at segment [5]. The plot of the STFT bicoherence for segment [5] shows that the transients are primarily non-harmonic, low frequency interactions, Figure 3.24c. These interactions are centered on frequency bands 100-200, 230-280, and 310-350kHz, Figure 3.24b.

The transient nonlinear interactions at $R = 1749$ are examined in Figures 3.25 and 3.26. At this station, the Fourier spectra, Figure 3.15, shows a pronounced peak at the frequency of the second mode. The total bicoherence, Figures 3.25a and 3.26a shows a peak at segment [1] and a more pronounced peak at segment [5]. The interaction peak at (f_o, f_o) indicates that there is strong forcing of the second mode by itself over the entire analysis period. The summed bicoherence, Figures 3.25b, 3.25f, 3.26b and 3.26f, shows that the interactions in the frequency band centered on the most amplified second mode and in the frequency band 0-50kHz are time invariant. At segment [5], Figure 3.26b, there are several bands of nonlinear interactions, with the transient interactions strongest in the 100-200kHz frequency band. Thus, in the corresponding STFT bicoherence, Figure 3.26c, in addition to the harmonic interaction, $f_1 + f_2 = f_o$, strong non-harmonic interaction bands are also present. However, while the harmonic interaction is invariant over the analysis period, Figures 3.25c, 3.25g, 3.26c and 3.26g, the non-harmonic interaction is intermittent. It is also interesting to note the temporal evolution of the two interaction peaks $(\delta f, \delta f)$ and (f_o, f_o) , which respectively indicate modulation of the second mode and harmonic forcing. Neither peak is simultaneously high; and when the interaction peak $(\delta f, \delta f)$ has a relatively large value, the interaction peak (f_o, f_o) tends to have a relatively small value. This may suggest that different energy transfer mechanisms take place during the

analysis period. Additionally, the level of all of the interaction peaks in Figure 3.25 and 3.26a are higher than those observed at $R = 1609$ and 1680 .

The transient nature of the nonlinear interactions $R = 1815$ is described by the variation in the total bispectrum in Figure 3.27a and 3.28a. Peaks are observed at segments [3] and [5]. While the peak at segment [5] is due to transient interactions centered on $100\text{-}200\text{kHz}$ similar to those observed in Figures 3.26c and 3.24c, the peak at segment [3] is slightly different. Comparing the summed bispectrum at segment [3], Figure 3.27g, with Figures 3.27c, 3.28c, and 3.38g, it is observed that the pair $(\delta f_o, \delta f_o)$ is only present at segment [3]. Another feature of the interactions at $R = 1815$ is the increased level of the pair (f_o, f_o) in Figure 3.27a and 3.28a *c.f.* $R = 1609 - 1749$.

The temporal behavior of the interactions at $R = 1879$ is seen from the total bicoherence and interaction peaks of the seven consecutive segments in Figures 3.29a and 3.30a. The variations in the data show that there are periods of strong broadband nonlinear coupling as well as periods without significant broadband interactions. This is inferred as the interaction peak (f_o, f_o) is approximately equal to 0.6 over the analysis period, and the interaction peak $(\delta f, \delta f)$ is relatively high ($\approx 0.3 - 0.4$) at segments [1]-[4], but then relatively low ($\approx 0.1 - 0.2$) for the segments [5]-[7]. The summed bicoherence at segments [1], [3] and [7], Figures 3.29b, 3.29f and 3.30f, respectively, show that the strong interaction bands are in the frequency ranges $25\text{-}100$, $250\text{-}350$, $510\text{-}630$ and $800\text{-}900\text{kHz}$. The strongest interaction occurs in the low frequency band $25\text{-}100\text{kHz}$. At segment [5], strong nonlinear interactions occur in the $50\text{-}100$, $110\text{-}180$ and $230\text{-}300\text{kHz}$ frequency bands. These non-harmonic interaction bands are clearly seen in the STFT bicoherence, Figure 3.30c, but do not occur in the other segments, Figures 3.29c, 3.29g

and 3.30g. The STFT, Figures 3.29d, 3.29h, 3.30d and 3.30h, shows peaks at the second mode and harmonic frequencies; thus strong harmonic interactions are observed over the entire analysis period. As at the upstream measurement stations, the transient nonlinear interactions occur at frequencies that are less than the frequency of the second mode.

The total bispectrum at $R = 1940$, Figure 3.31a and 3.32a, shows only a slight variation in its level over the analysis period. The apparent absence of significant transient nonlinear interactions is suggested further by the similarity in the STFT bispectra at each analysis time, Figures 3.31c, 3.31g, 3.32c, and 3.32g.

3.3.2 Effect of Wall Cooling

The transient nonlinear interactions at $R = 1609$ are examined in Figures 3.33 and 3.34. The variations in the total bicoherence and in the interaction peaks measured from the STFT bispectrum show that transient nonlinear interactions are present. The plots of the summed bicoherence, Figure 3.33b, 3.33f, 3.34b, and 3.34f, show that the transient nonlinear interactions are only strong in segment [5]. In this segment the interactions occur in three distinct frequency bands, 100-200, 210-305 and 310-370kHz. The strongest interactions occur in the 100-200kHz frequency band. Although the STFT, Figures 3.33d, 3.33h, 3.34d and 3.34h, clearly show the second mode, harmonic interactions are not seen in the segments [1], [3] nor [7], during which there are no low frequency transient nonlinear interactions.

Further downstream at $R = 1680$, the peak in the total bicoherence at segment [6] indicates that a transient nonlinear interaction has occurred, Figure 3.35a and 3.36a. It is also observed that during the downstream evolution of the disturbances, the level of the

frequency pair $(f_o, \delta f)$ has increased while the other frequency pairs have remained at the same level, Figure 3.35a and 3.36a. The transient nature of the interactions at frequency pair $(f_o, \delta f)$ are clearly seen as a peak at segment [5] in Figure 3.35a and 3.36a and are also detected in the summed bispectrum (10-40kHz and 300-320kHz) and in Fourier bispectrum at segment [5], Figure 3.35f and 3.35g, respectively.

The plot of the total bicoherence at $R = 1749$, Figures 3.37a and 3.38a, shows that transient nonlinear interactions occur. It is seen in Figure 3.37a and 3.38a that the interaction $(\delta f, \delta f)$ has become more developed. The STFT bicoherence, Figures 3.37c, 3.37g, 3.38c and 3.38g, show that the phase coupled harmonic interactions, $f_1 + f_2 = f_o$, $2f_o$, or $3f_o$, are present over the entire analysis period. These phase coupled harmonic interactions are also seen as the peaks centered on f_o , $2f_o$, and $3f_o$ in the plots of the summed bicoherence, Figures 3.37b, 3.37f, 3.38b and 3.38f. In segment [5], transient nonlinear interactions are seen in the 60-200 and 210-280kHz frequency bands. These interaction bands are also pronounced in the corresponding STFT bicoherence, Figure 3.38d.

At $R = 1815$, the level of the total bicoherence has increased, indicating the downstream growth of nonlinear disturbances, Figure 3.39a and 3.40a. The frequency pairs $(\delta f, \delta f)$ and (f_o, f_o) are now at much higher levels than the previous locations and also exhibit transient behavior, Figure 3.39a and 3.40a. From the summed bispectrum (Figure 3.39b, 3.39f, 3.40b, and 3.40f), there is no evidence of the low frequency non-harmonic transient interactions such as those observed in Figure 3.38b. It is noted in the STFT bispectrum figures that the interaction pair $(f_o, \delta f)$ has become broader at this measurement location.

The transient nonlinear interactions at $R = 1879$ are examined in Figures 3.42 and 3.43. There are very large variations in the STFT bicoherence interaction peaks at $(\delta f, \delta f)$ and (f_o, f_o) , Figures 3.42a and 3.43a. The relative magnitudes of the interaction peaks show that in these latter stages of the nonlinear region, there are transient events associated with the interactions $(\delta f, \delta f)$ and (f_o, f_o) , Figures 3.42a and 3.43a. The summed bicoherence, Figures 3.42b, 3.42f, 3.43b and 3.43f, shows that in these latter stages, the nonlinear interactions are of a very low frequency, 0-100kHz.

At $R = 1940$ the initial effects of the breakdown to turbulent flow are observed. The magnitude of the total bispectrum has increased when compared to the previous stations, while the interactions pairs in Figures 3.43a and 3.44a have begun to decrease. This decrease is attributed to the spreading of the energy over the disorganized broadband nonlinear interactions present in the STFT bispectrum, Figure 3.43c, 3.43g, 3.44c, and 3.44g.

3.3.3 Effect of Pressure Gradient

The transient nonlinear interactions for the 93-10 adiabatic cone model are examined in Figures 3.45 - 3.54 at $R = 1879, 1940, 2000, 2058,$ and 2114 in order to examine the effects of a smaller pressure gradient. At $R = 1879$, the total bispectrum and frequency pairs in Figure 3.45a and 3.46a exhibit transient behavior, however the values are low in magnitude. The absence of significant peaks in the STFT bispectrum (Figure 3.45c, 3.45g, 3.46c, and 3.46g) confirm the low levels of nonlinear interactions. This is in contrast to the baseline case in which transient and steady nonlinear interactions are prominent in the STFT bispectrum, Figure 3.29c, 3.29g, 3.30c, and 3.30g.

At $R = 1940$, the level of the total bicoherence has increased and exhibits a peak at segment [6], Figure 3.47a and 3.48a. This peak is an indicator that transient nonlinear interactions exist. In Figure 3.47a and 3.48a, the frequency pair $(\delta f, \delta f)$ has increased in magnitude and also shows a transient behavior with a peak at segment [3].

Further downstream, the total bicoherence at $R = 2000$ (Figure 3.49a and 3.50a) shows peaks at segment [2] and [5]. The intermittent nonlinear interactions associated with the peak at segment [5] is again due to low frequency interactions, Figure 3.50b and 3.50c. The interaction peaks $(f_o, \delta f)$ and (f_o, f_o) are elevated and also show some transient behavior, Figure 3.49a and 3.50a.

The total bicoherence continues to increase in magnitude at $R = 2058$ and at this station is highest at segment [5], Figure 3.51a and 3.52a. Similar to previous cases, the STFT bispectra at segment [5] show non-harmonic interactions, Figure 3.52c. From the summed bicoherence at segment [5], it is observed that these transient nonlinear interactions are broadband in nature, Figure 3.52b.

Finally, for $R = 2114$ the total bicoherence continues to increase in magnitude, Figure 3.53a and 3.54a, and tends to vary regularly. The levels of the interaction peaks $(\delta f, \delta f)$, $(f_o, \delta f)$ and $(2f_o, f_o)$ also have increased as the nonlinear interactions continue to evolve. The more pronounced transient nonlinear interaction occurs at segment [3], where a significant low frequency peak is observed in the summed bicoherence, Figure 3.53g.

The STFT bicoherence identifies and quantifies both transient and steady nonlinear interactions. The steady nonlinear interactions are also observed in the Fourier

bispectrum, and are associated with primarily harmonic interactions. However, the transient nonlinear interactions are non-harmonic and broadband in nature.

CONCLUDING REMARKS

4.1 Summary of Results

High order spectral analysis (HOSA) tools that can capture the nonlinear and time varying characteristics of fluid flows are developed. These tools provide new insight into the dynamics of hypersonic transitioning flows. This insight is important for the development of transition prediction methods and techniques to control transition.

The HOSA tools are applied to previously obtained uncalibrated hot-wire measurements. The hot-wire was operated by a constant voltage anemometer (CVA) and the measurements obtained in a quiet (that is low disturbance freestream) Mach 6 tunnel. The uncalibrated hot-wire measurements document the stability of hypersonic transitioning boundary layer subject to the effects of wall cooling and adverse pressure gradient. These effects of the nonlinear and time varying characteristics are examined using the short-time Fourier transform (STFT), the Fourier bispectrum, and the STFT bispectrum. The most pertinent findings of the application of these methods can be summarized as follows.

The STFT is used to quantify the time varying characteristics of the dominant second mode and its first harmonic. The STFT clearly identifies the modulation of the second mode and its harmonic as the boundary layer undergoes transition. The STFT analysis quantifies that phase modulation is the primary energy transfer mechanism from the second mode during the hypersonic transition. However, during the latter stages of transition amplitude modulation plays an increasingly important role. In the present work, wall cooling is observed to have a more pronounced effect than adverse pressure gradient

on destabilizing the flow and thus resulting in an earlier onset of nonlinear interactions. Similar observations were made in previous work employing the digital complex demodulation (DCD) technique and the wavelet analysis. The DCD is limited to analysis of a single frequency at a time, and the wavelet analysis, with a sinusoidal basis function, suffers from poor resolution at the high frequencies characteristic of the dominant second mode.

The Fourier bispectrum is used to quantify the quadratic phase coupled interactions that arise as the transitioning hypersonic flow moves from the linear region into the nonlinear region. The peaks in the Fourier bispectrum indicate forcing of the first and second harmonics, and clarify the dominant role of the most unstable second mode disturbance. In the latter stages of the nonlinear region, low frequency phase coupled interactions are also identified in the Fourier bispectrum, and are associated with the amplitude and phase modulation that are observed in the STFT analysis. Thus in the initial stages of the nonlinear region harmonic band interactions play the more important role in energy transfer; in the latter stages of the nonlinear region the low frequency interactions play the more dominant role as the flow breaks down to turbulence. The effect of wall cooling and adverse pressure gradient is to advance the onset of the quadratic phase coupled interactions.

The author developed the STFT bispectrum to identify and quantify the time-varying nature of the nonlinear interactions. This new HOSA tool combines the time localization characteristic of the STFT and nonlinear identification feature of the bispectral analysis. The STFT bispectrum analysis shows that the forcing of the harmonic is intermittent, which also suggests that the energy transfer is transient. This information

is “hidden” in the Fourier bispectrum because of its long time average. In addition, the transient energy transfer is observed to occur within relative low frequency, non-harmonic, broad bands. These transient interactions appear to play a role in the transition of the hypersonic boundary layer.

4.2 Future Work

High order spectral analysis techniques provide additional insights into the dynamics of the transitioning hypersonic flow other than the limited information of the power spectrum. As a first step, the observed time-varying and nonlinear characteristics must be simulated in transition prediction methods. These characteristics are observed to be important in the latter stages of transition and must be modeled if the reliability of the transition prediction tools is to be improved. The improved understanding of the transition process provided by HOSA techniques has the potential to suggest new approaches for the control of transition. For example, a control method directed at interrupting the periodic and transient low frequency interactions may be more practicable than suppression of the relatively high frequency second mode.

In the previous experiments the measurements were limited to single-point, uncalibrated hot-wire measurements in a naturally excited flow. It is recommended that future experiments include multiple, simultaneous hot-wire measurements. These measurements can then provide additional information about the spatial-temporal dynamics of the transitioning flow. The HOSA tools developed here can be readily adapted to multiple point measurements. It is also recommended that future experiments include calibrated measurements of the freestream disturbance field, as these calibrated

data can be directly compared or input to transition prediction tools. Lastly, in a naturally excited flow, the forcing of the flow cannot be systematically controlled. It is recommended that artificial excitation be used in future experiments. The characteristics of the controlled disturbance input can be measured with the improved CVA capability. The evolution of the disturbances can be characterized using the HOSA techniques. These recommendations provide a framework for the currently proposed collaborative experiments with the Institute of Theoretical and Applied Mechanics, Russian Academy of Sciences – Siberian Branch.

REFERENCES

- ¹ Bowcutt, K. G., Anderson, J. D., and Capriotti, D., "Viscous Optimized Hypersonic Waveriders," *AIAA Paper 87-0272*, January 1987.
- ² Fedorov, A. V., Malmuth, N. D., Rasheed, A. and Hornung, H. G., "Stabilization of Hypersonic Boundary Layers by Porous Coatings," *AIAA Journal*, Vol. 39, April 2001, pp. 605-610.
- ³ Rasheed, A., Hornung, H. G. Fedorov, A. V. and Malmuth, N. D., "Experiments on Passive Hypervelocity Boundary-Layer Control Using a Porous Surface," *AIAA Paper 2001-0274*, January 2001.
- ⁴ Reshotko, E., "Boundary Layer Instability, Transition, and Control," *AIAA Paper 94-0001*, January 1994.
- ⁵ Kimmel, R. L., Demetriades, A. and Donaldson, J. C., "Space-Time Correlation Measurements in a Hypersonic Transitional Boundary Layer," *AIAA Journal*, Vol. 34, December 1996, pp. 2484-2489.
- ⁶ Reshotko, E., "Transient Growth: A Factor in Bypass Transition," *Phys. Fluids*, Vol. 13, May 2001, pp. 1067-1075.
- ⁷ Schneider, S. P., "Effects of High-Speed Tunnel Noise on Laminar-Turbulent Transition," *AIAA Paper 2000-2205*, June 2000.
- ⁸ Morkovin, M. V., "On Supersonic Wind Tunnels with Low Free-Stream Disturbances," *Journal of Applied Mechanics*, Vol. 26, September 1959, pp. 319-324.
- ⁹ Laufer, J., "Aerodynamic Noise in Supersonic Wind Tunnels," *Jet Propulsion Laboratory Progress Report No. 20-378*, California Institute of Technology, Pasadena, CA, February 1959.
- ¹⁰ Wilkinson, S. P., "A Review of Hypersonic Boundary Layer Stability Experiments in a Quiet Mach 6 Wind Tunnel," *AIAA Paper 97-1819*, June 1997.
- ¹¹ Kendall, J. M., "Wind Tunnel Experiments Relating to Supersonic and Hypersonic Boundary Layer Transition," *AIAA Journal*, Vol. 13, March 1975, pp. 290-299.
- ¹² Stetson, K. F., Thompson, E. R., Donaldson, J. C. and Siler, L. G., "Laminar Boundary Layer Stability Experiments on a Cone at Mach 8, Part 1: Sharp Cone," *AIAA Paper 83-1761*, July 1983.

-
- ¹³ Stetson, K. F., Thompson, E. R., Donaldson, J. C. and Siler, L. G., "Laminar Boundary Layer Stability Experiments on a Cone at Mach 8, Part 2: Blunt Cone," *AIAA Paper 84-0006*, January 1984.
- ¹⁴ Stetson, K. F., Thompson, E. R., Donaldson, J. C. and Siler, L. G., "Laminar Boundary Layer Stability Experiments on a Cone at Mach 8, Part 4: on Unit Reynolds Number and Environmental Effects," *AIAA Paper 89-1087*, June 1989.
- ¹⁵ Stetson, K. F., Thompson, E. R., Donaldson, J. C. and Siler, L. G., "Laminar Boundary Layer Stability Experiments on a Cone at Mach 8, Part 5: Tests with a Cooled Model," *AIAA Paper 89-1895*, June 1989.
- ¹⁶ Kimmel, R. L. and Poggie, J., "Disturbance Evolution/Breakdown to Turbulence in a Hypersonic Boundary Layer: Ensemble-Averaged Structure," *AIAA Paper 97-0555*, January 1997.
- ¹⁷ Poggie, J. and Kimmel, R. L., "Disturbance Evolution and Breakdown to Turbulence in a Hypersonic Boundary Layer: Instantaneous Structure," *AIAA Paper 97-0556*, January 1997.
- ¹⁸ Lachowicz, J. T., Chokani, N. and Wilkinson, S. P., "Boundary-Layer Stability Measurements in a Hypersonic Quiet Tunnel," *AIAA Journal*, Vol. 34, December 1996, pp. 2496-2500.
- ¹⁹ Doggett, G. P., Chokani, N. and Wilkinson, S. P., "Effects of Angle of Attack on Hypersonic Boundary Layer Stability in a Quiet Wind Tunnel," *AIAA Journal*, Vol. 35, March 1997, pp. 464-470.
- ²⁰ Blanchard, A. E. and Selby, G. V., "An Experimental Investigation of Wall-Cooling Effects on Hypersonic Boundary-Layer Stability in a Quiet Wind Tunnel," *NASA CR 198287*, 1996.
- ²¹ Manning, M. L., "Computational Evaluation of Quiet Tunnel Hypersonic Boundary Layer Stability Experiments," *MS Thesis*, MAE Department, North Carolina State University, Raleigh NC, December 2000.
- ²² Chang, C. -L., Vinh, H. and Malik, M. R., "Hypersonic Boundary-Layer Stability with Chemical Reactions using PSE," *AIAA Paper 97-2012*, June 1997.
- ²³ Herbert, T., "Parabolized Stability Equations," *Annual Review of Fluid Mechanics*, Vol. 29, 1997, pp. 245-283.
- ²⁴ Pruett, C. P. and Chang, C. -L., "Direct Numerical Simulation of Hypersonic Boundary-Layer Flow on a Flared Cone," *Theoretical and Computational Fluid Dynamics*, Vol. 11, March 1998, pp. 49-67.

- ²⁵ McDaniel, R. D., and Hassan, H. A., "Role of Bypass Transition in Conventional Hypersonic Facilities," *AIAA Paper 2001-0209*, January 2001.
- ²⁶ Street, C. L., "Direct Harmonic Linear Navier-Stokes Methods of Efficient Simulation of Wave Packets," *AIAA Paper 98-0784*, June 1998.
- ²⁷ Chokani, N., "Nonlinear Stability of Quiet Tunnel Hypersonic Laminar Boundary Layer Flow," *AIAA Paper 99-0407*, January 1999.
- ²⁸ Kimmel, R. L. and Kendall, J. M., "Nonlinear Disturbances in a Hypersonic Boundary Layer," *AIAA Paper 91-0320*, January 1991.
- ²⁹ Chokani, N., "Nonlinear Spectral Dynamics of Hypersonic Laminar Boundary Layer Flow," *Physics of Fluids*, Vol. 12, December 1999, pp. 3846-3851.
- ³⁰ Chokani, N., "Wave Modulation in the Transition of a Hypersonic Boundary Layer Flow," *AIAA Paper 2000-2653*, June 2000.
- ³¹ Chokani, N., "Wavelet Analysis of a Hypersonic Laminar Boundary Layer Flow," *AIAA Paper 2000-0535*, January 2000.
- ³² Blanchard, A. E., Lachowicz, J. T., and Wilkinson, S. P., "NASA Langley Mach 6 Quiet Wind-Tunnel Performance," *AIAA Journal*, Vol. 35, January 1997, pp. 23-28.
- ³³ Lachowicz, J. T. and Chokani, N., "Hypersonic Boundary Layer Stability Experiments in a Quiet Wind Tunnel with Bluntness Effects," *NASA CR-198272*, January 1996.
- ³⁴ Morkovin, M. V., "Fluctuations and Hot-Wire Anemometry in Compressible Flows," *AGARDograph 24*, November 1956.
- ³⁵ Sarma, G. R., "Flow Measuring Apparatus," *US Patent 5074147*, December 1991.
- ³⁶ Sarma, G. R., "Transfer Function Analysis of the Constant Voltage Anemometer," *Review of Scientific Instruments*, Vol. 69, June 1998, pp. 2385-2391.
- ³⁷ Comte-Bellot, G. and Sarma, G. R., "Constant Voltage Anemometer Practice in Supersonic Flows," *AIAA Journal*, Vol. 39, February 2001, pp. 261-270.
- ³⁸ Hardin, J. C., "Introduction to Time Series Analysis," *NASA Reference Publication 1145*, 1990.
- ³⁹ Rabiner, L. R. and Schafer R. W., *Digital Processing of Speech Signals*, Prentice-Hall, Englewood Cliffs, 1978.
- ⁴⁰ Qian, S. and Chen, D., *Joint Time-Frequency Analysis*, Prentice-Hall, Upper Saddle River, NJ, 1996.

⁴¹ Morgenstern, A. and Chokani, N., "Hypersonic Flow Past Open Cavities," *AIAA Journal*, Vol. 32, December 1994, pp. 2387-2393.

⁴² van Milligen, B. Ph., Sánchez, E., Estrada, T., Hidalgo, C., Brañas, B., Carreras, B., and García, L., "Wavelet Bicoherence: A New Turbulence Analysis Tool," *Physics of Plasmas*, Vol. 8, August 1995, pp. 3017-3032.

⁴³ van Milligen, B. Ph., Hidalgo, C., Sánchez, E., "Nonlinear Phenomenon and Intermittency in Plasma Turbulence," *Physical Review Letters*, Vol. 74, January 1995, pp. 395-398.

TABLES

Table 2.1 - Measurement locations and corresponding stability Reynolds numbers for the Mach 6 quiet tunnel.

	<i>x</i> (in)	<i>R</i>	
	9.00	1455	
	9.25	1475	
	9.50	1495	
	9.75	1515	
	10.00	1534	
	10.25	1553	
	10.50	1572	
	10.75	1590	
	11.00	1609	
	11.25	1627	
	11.50	1645	
	11.75	1663	
	12.00	1680	
	12.25	1698	
	12.50	1715	
	12.75	1732	
	13.00	1749	
	13.25	1766	
	13.50	1782	
	13.75	1799	
	14.00	1815	
	14.25	1831	
	14.50	1847	
	14.75	1863	
	15.00	1879	
	15.25	1894	
	15.50	1910	
	15.75	1925	
	16.00	1940	
	16.25	1955	
	16.50	1970	
	16.75	1985	
	17.00	2000	
	17.25	2015	
	17.50	2029	
	17.75	2044	
	18.00	2058	
	18.25	2072	
	18.50	2086	
	18.75	2100	
	19.00	2114	

91-6 Adiabatic and Cooled Cone
(Blanchard and Selby²¹)

{

93-10 Adiabatic Cone
(Lachowicz *et al*³⁵)

}

Table 2.2 - Reynolds numbers and overheats for the SWK runs.

FIGURES

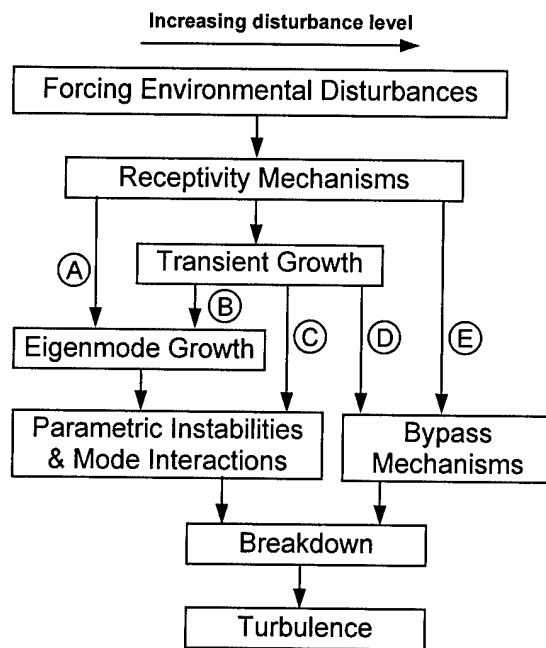


Figure 1.1 – Paths to turbulence (Reference 6).

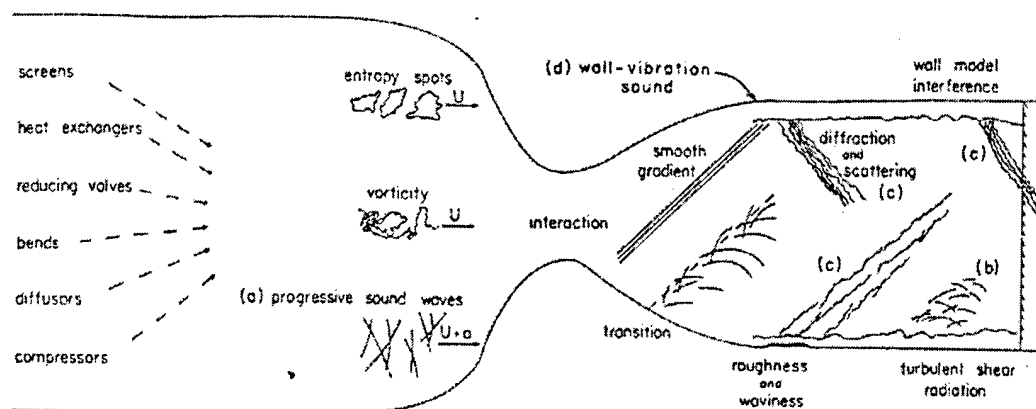


Figure 1.2 – Free-stream disturbance sources in high-speed wind tunnels (Reference 8).

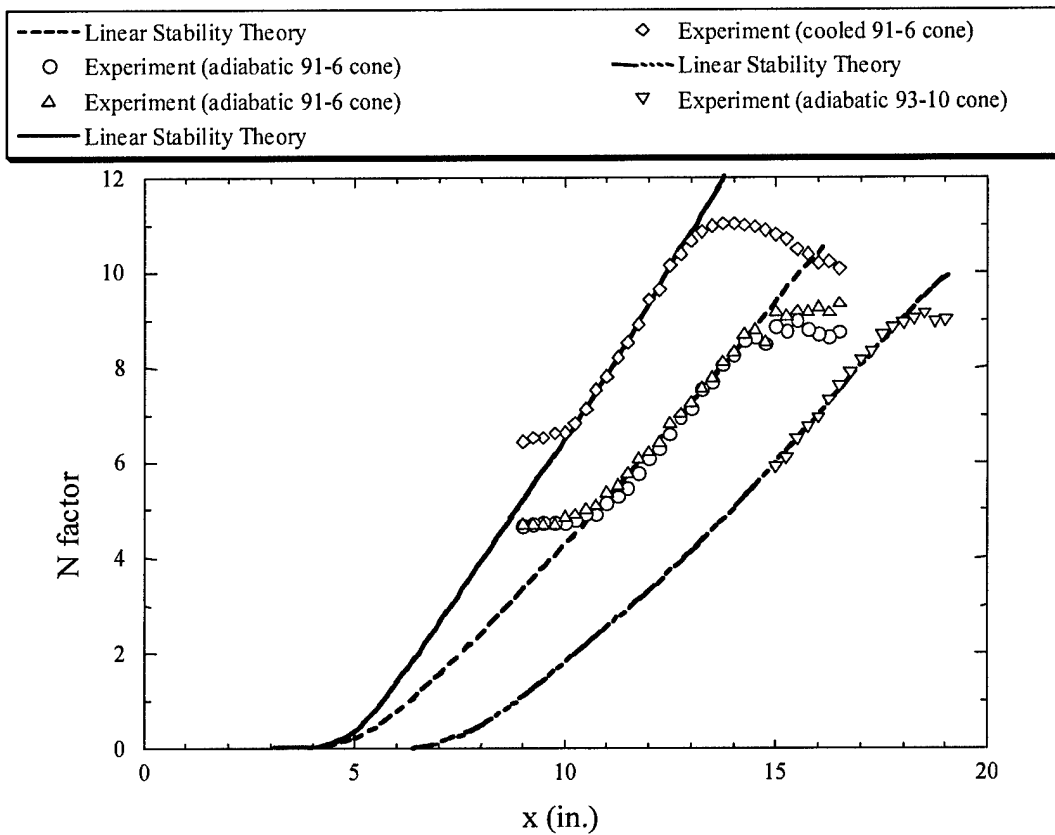


Figure 1.3 - Comparison of experimentally measured integrated growth rates with linear stability theory (Reference 10).

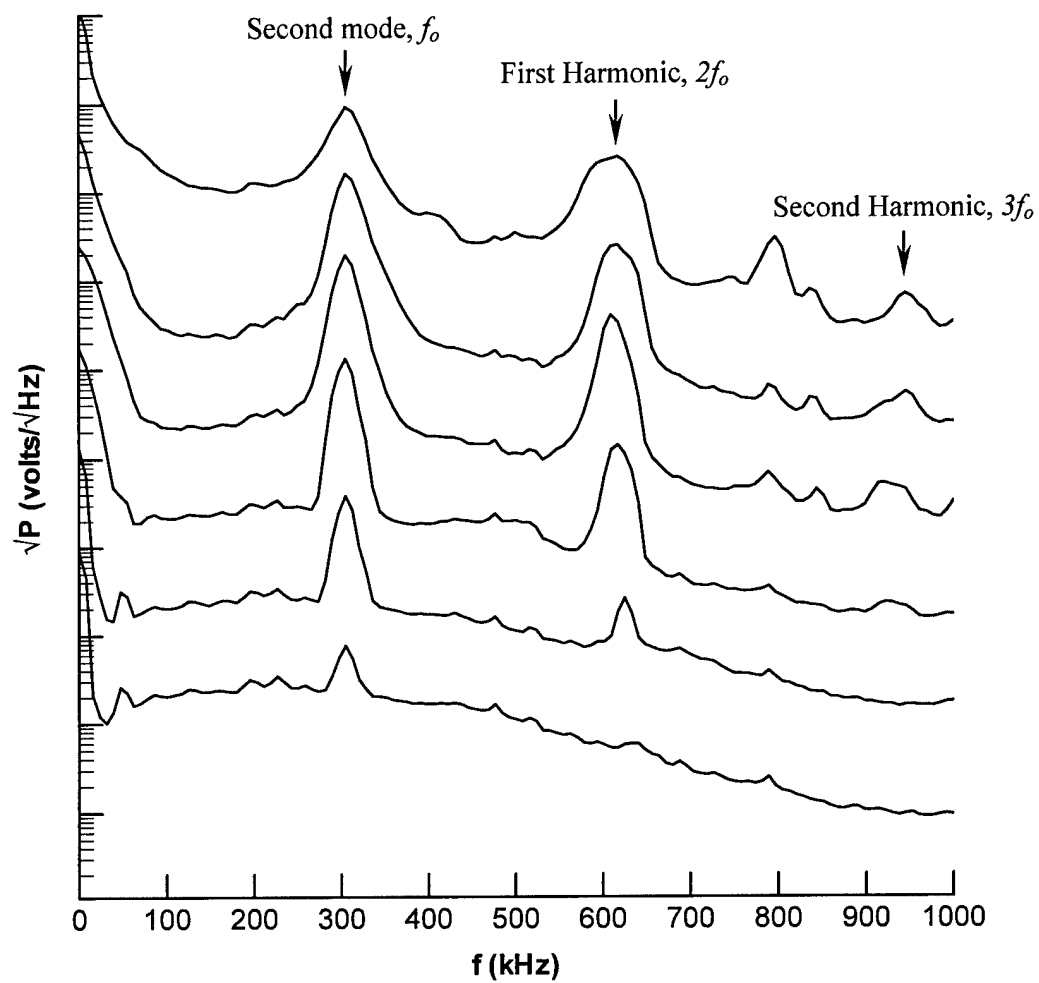


Figure 1.4 – Power spectra of disturbances measured in the Mach 6 quiet tunnel experiment of Blanchard and Shelby.

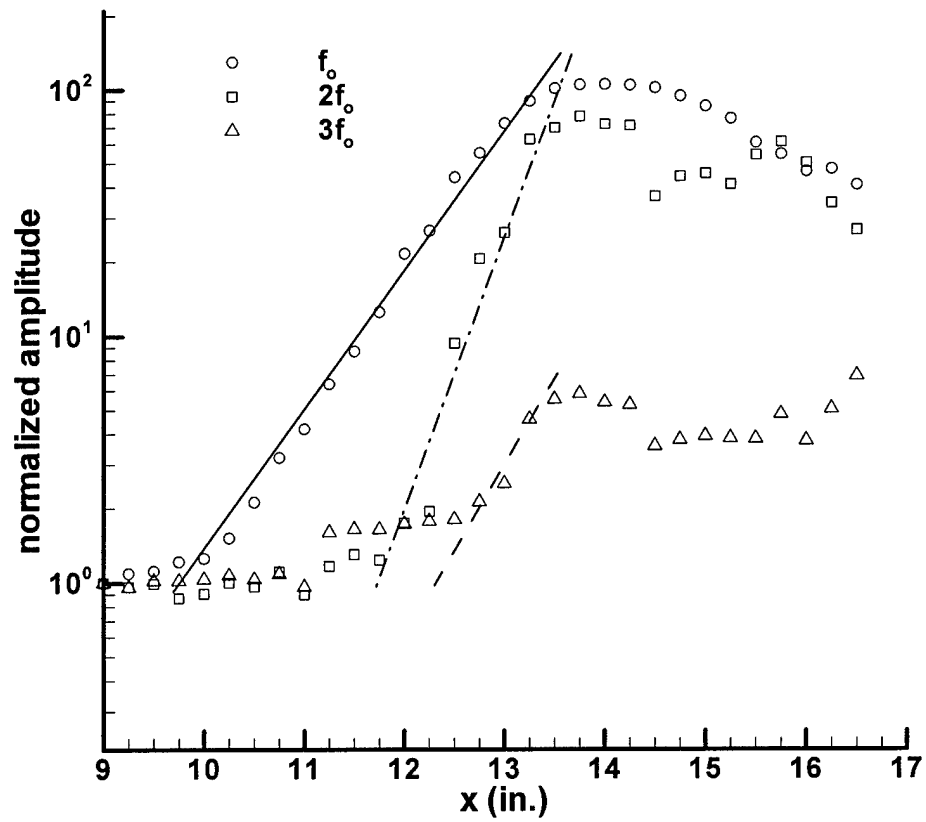


Figure 1.5 – Downstream evolution of spectral amplitudes of second-mode and harmonics (Reference 29).

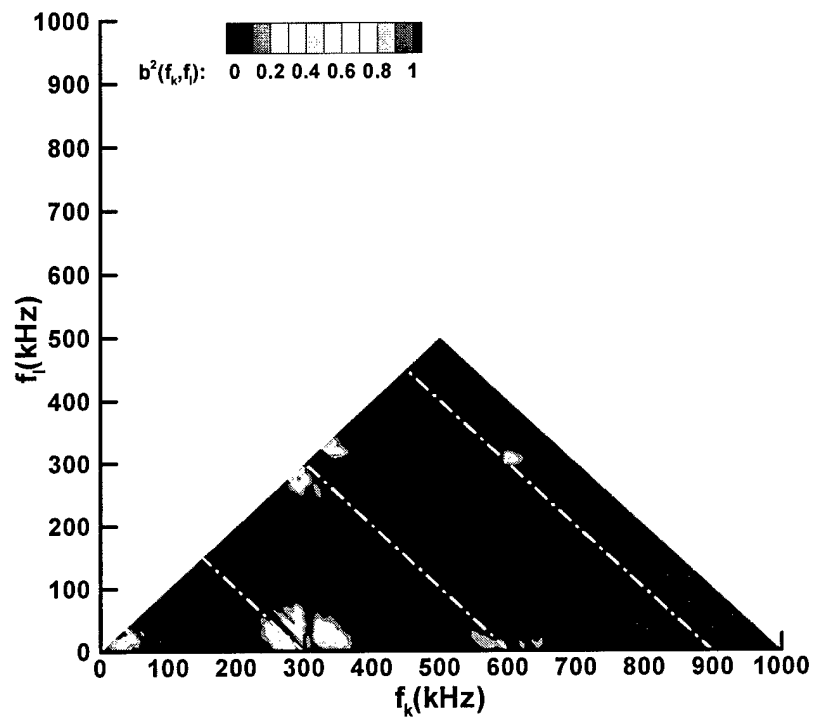


Figure 1.6 – Bispectrum (Reference 31).

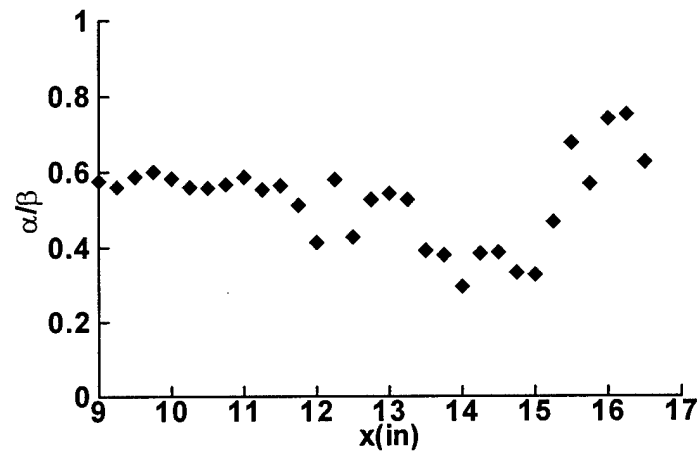


Figure 1.7 - Downstream evolution of amplitude and phase modulation indices from the digital complex demodulation technique (Reference 30).

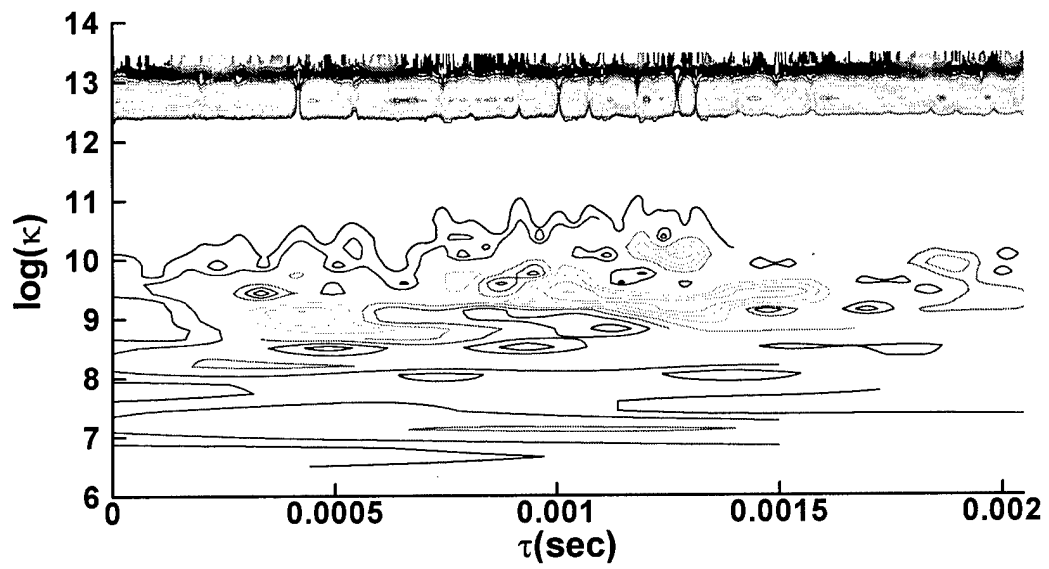


Figure 1.8 - Modulus of wavelet coefficients (Reference 31).

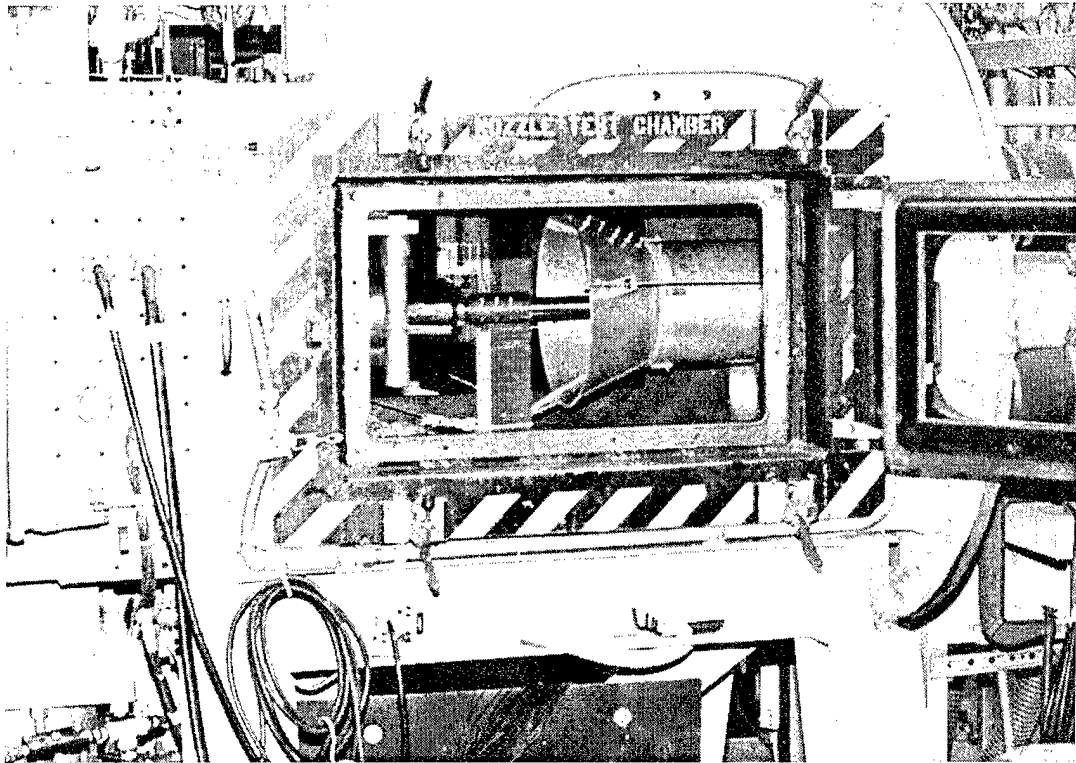


Figure 2.1 - NASA Langley Mach 6 quiet tunnel.

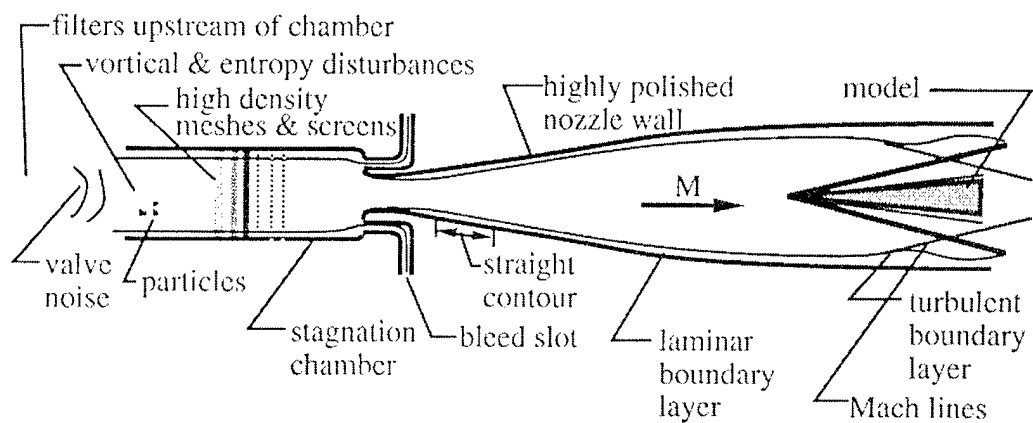


Figure 2.2 - Quiet wind tunnel design (Reference 33).

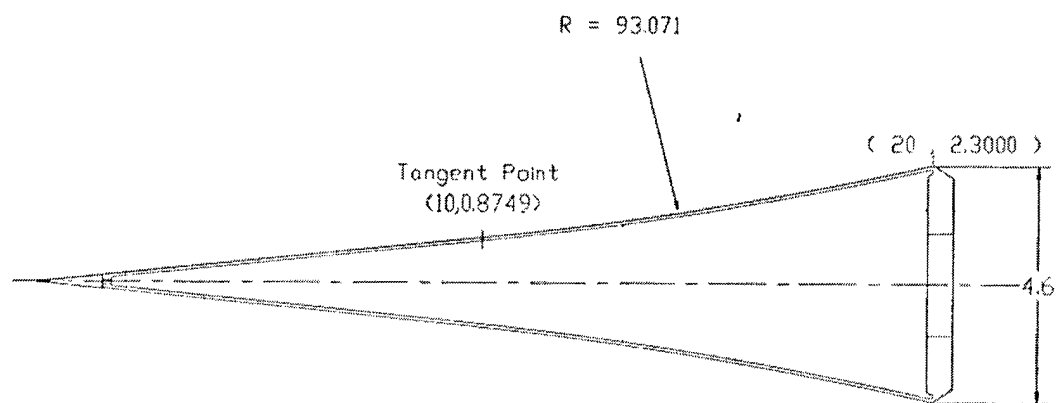


Figure 2.3 - 93-10 Adiabatic wall flared-cone model used by Lachowicz *et al* (Reference 33).

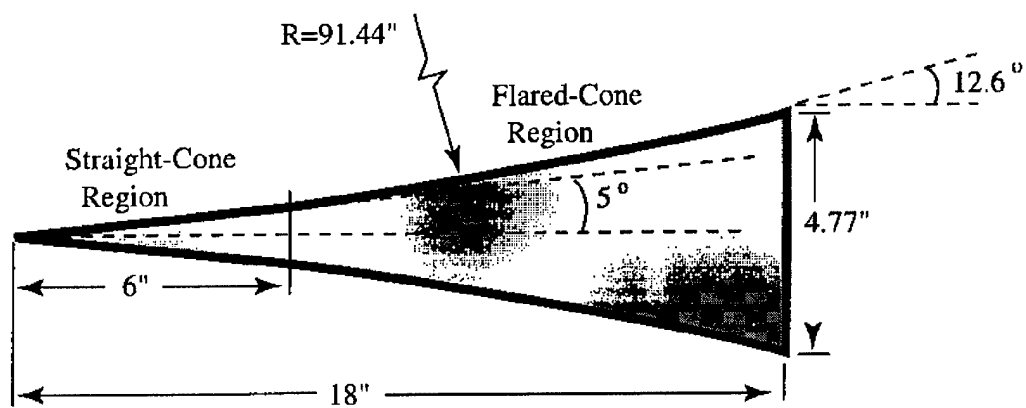


Figure 2.4 - 91-6 Adiabatic and cooled wall flared-cone model used by Blanchard and Selby (Reference 32).

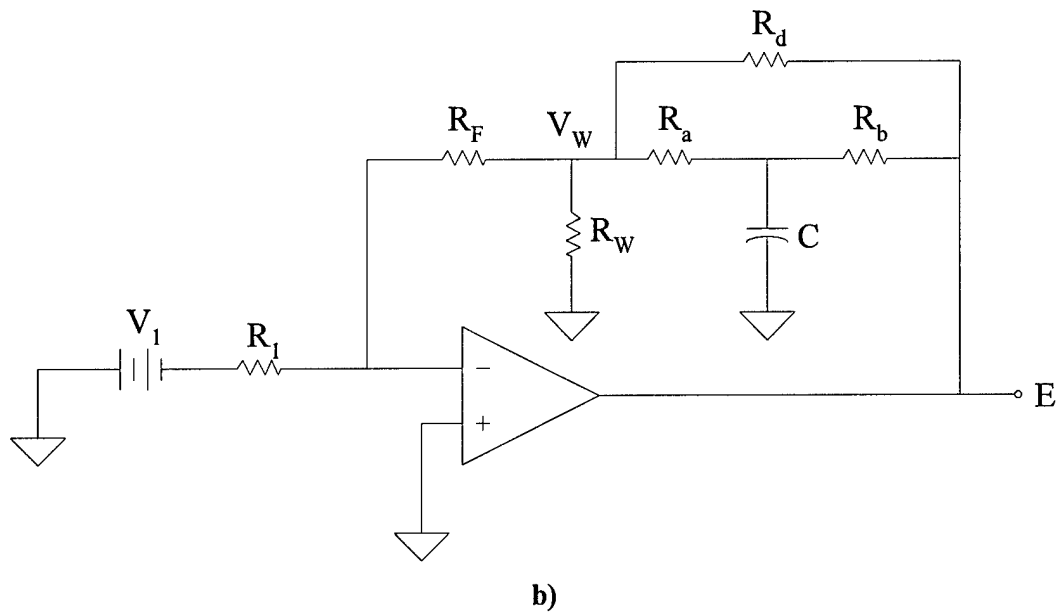
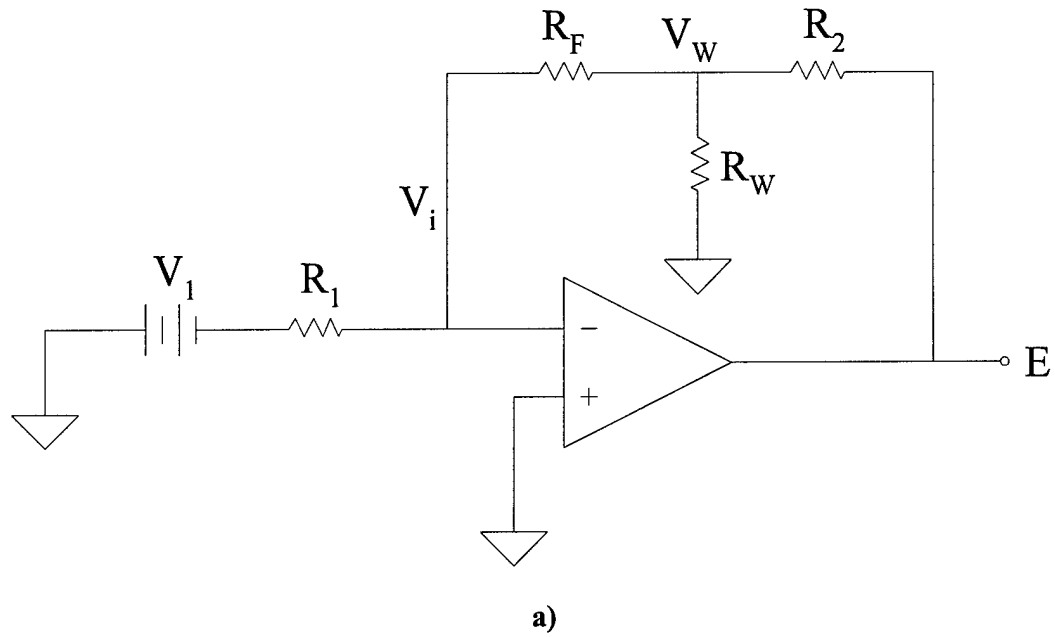


Figure 2.5 - a) Basic circuit of the constant voltage anemometer, b) circuit with frequency compensation (Reference 36).

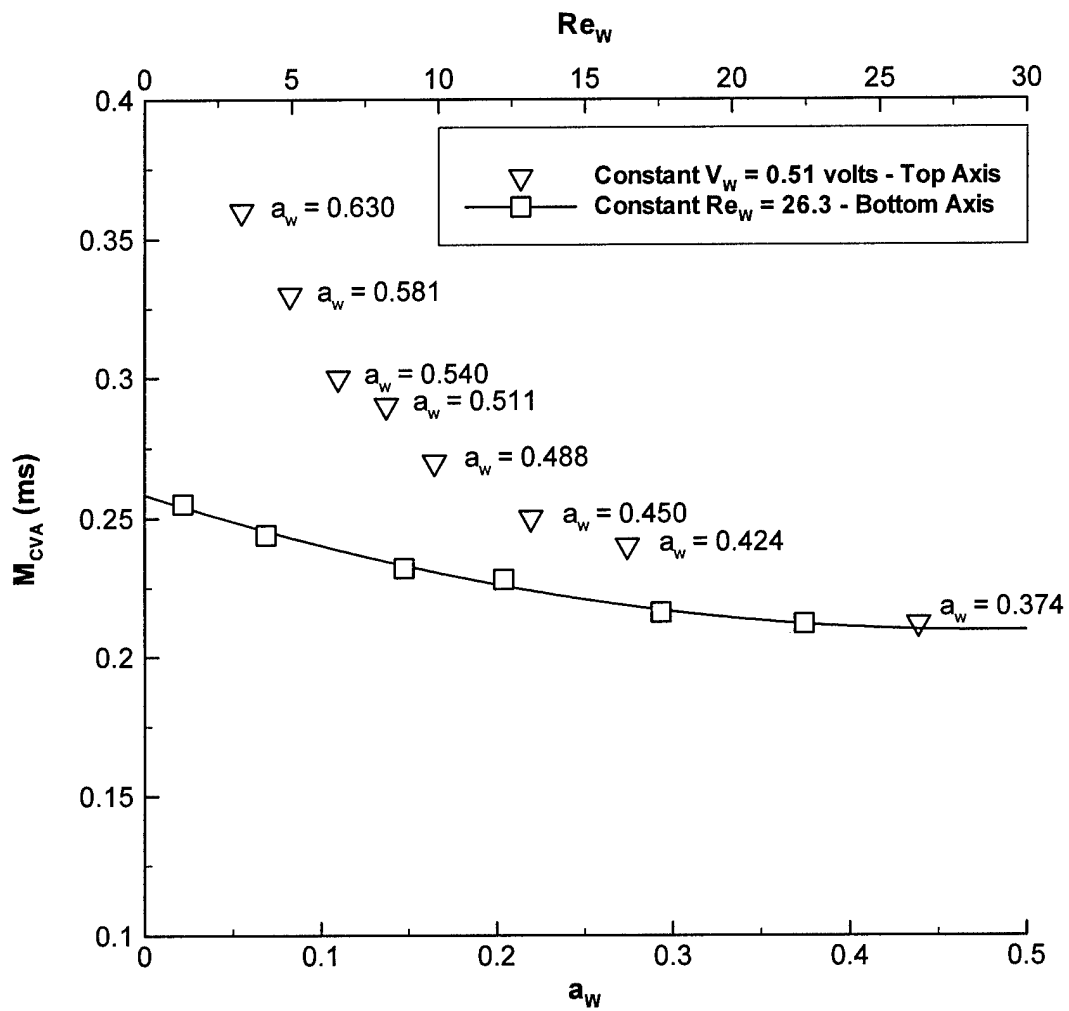


Figure 2.6 - Example of hot-wire time constant variation with Reynolds number and overheat ratio.

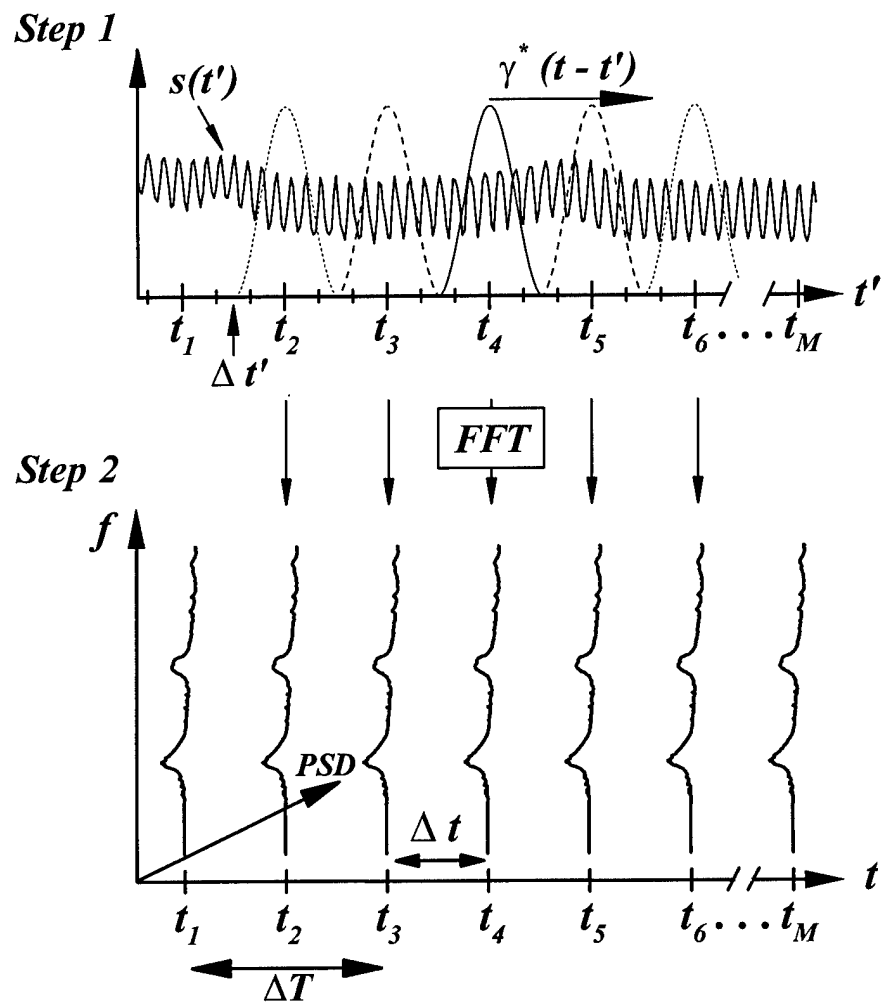


Figure 2.7 - Graphical illustration of the short-time Fourier transform.

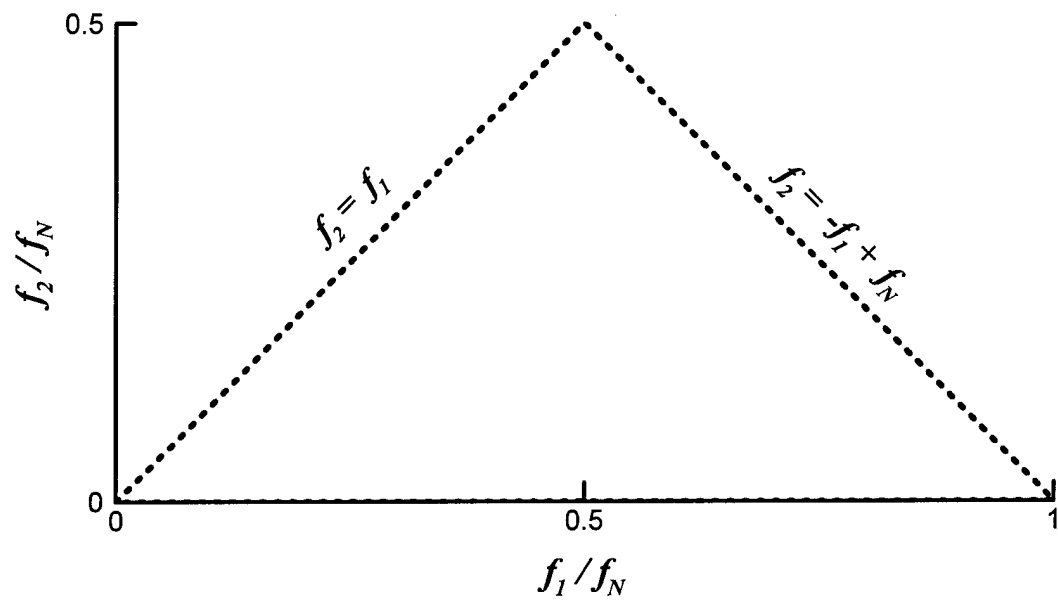


Figure 2.8 - Triangular region for Fourier bispectrum showing the sum frequency interaction region.

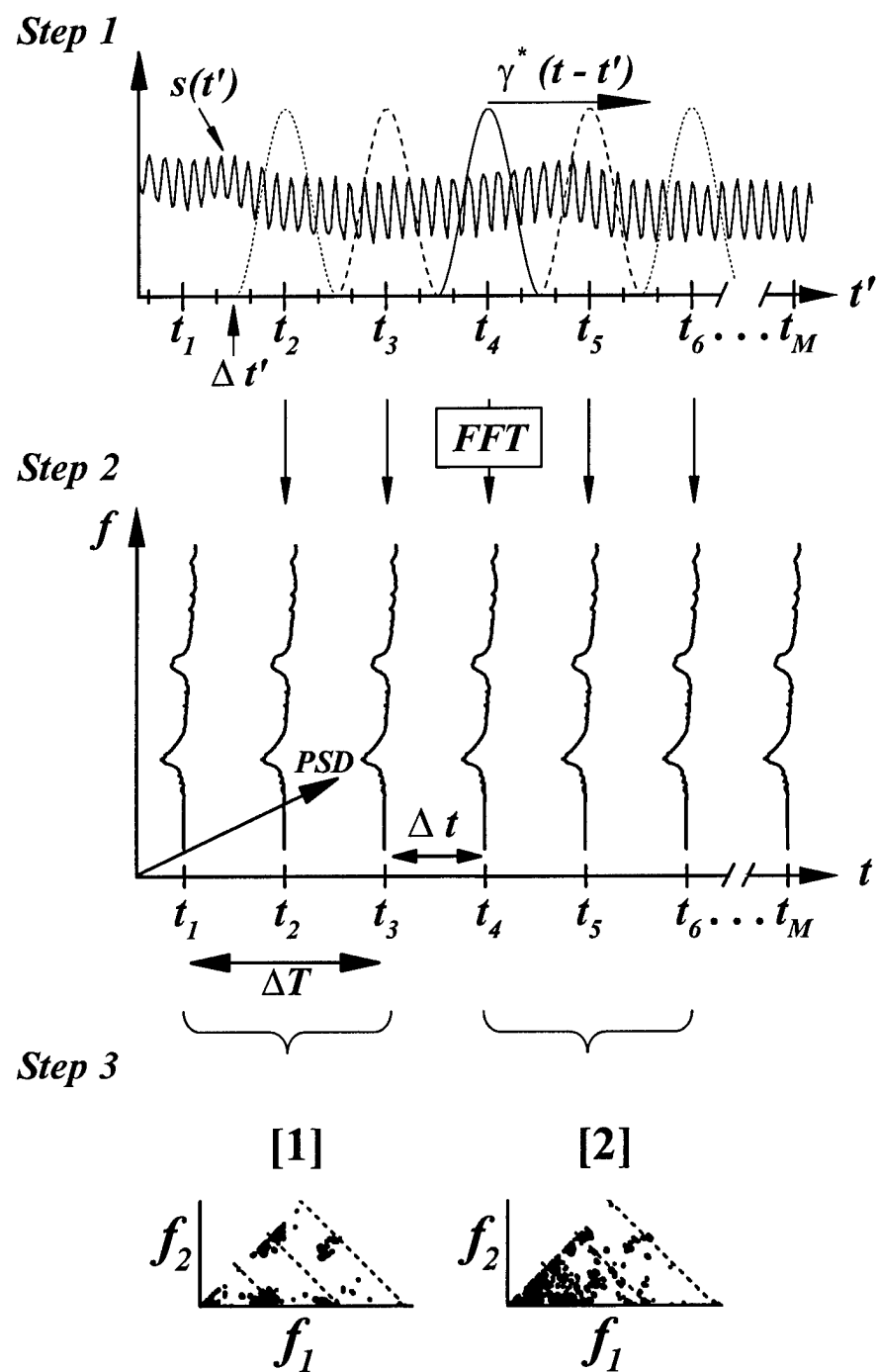


Figure 2.9 - Graphical illustration of the STFT bispectrum.

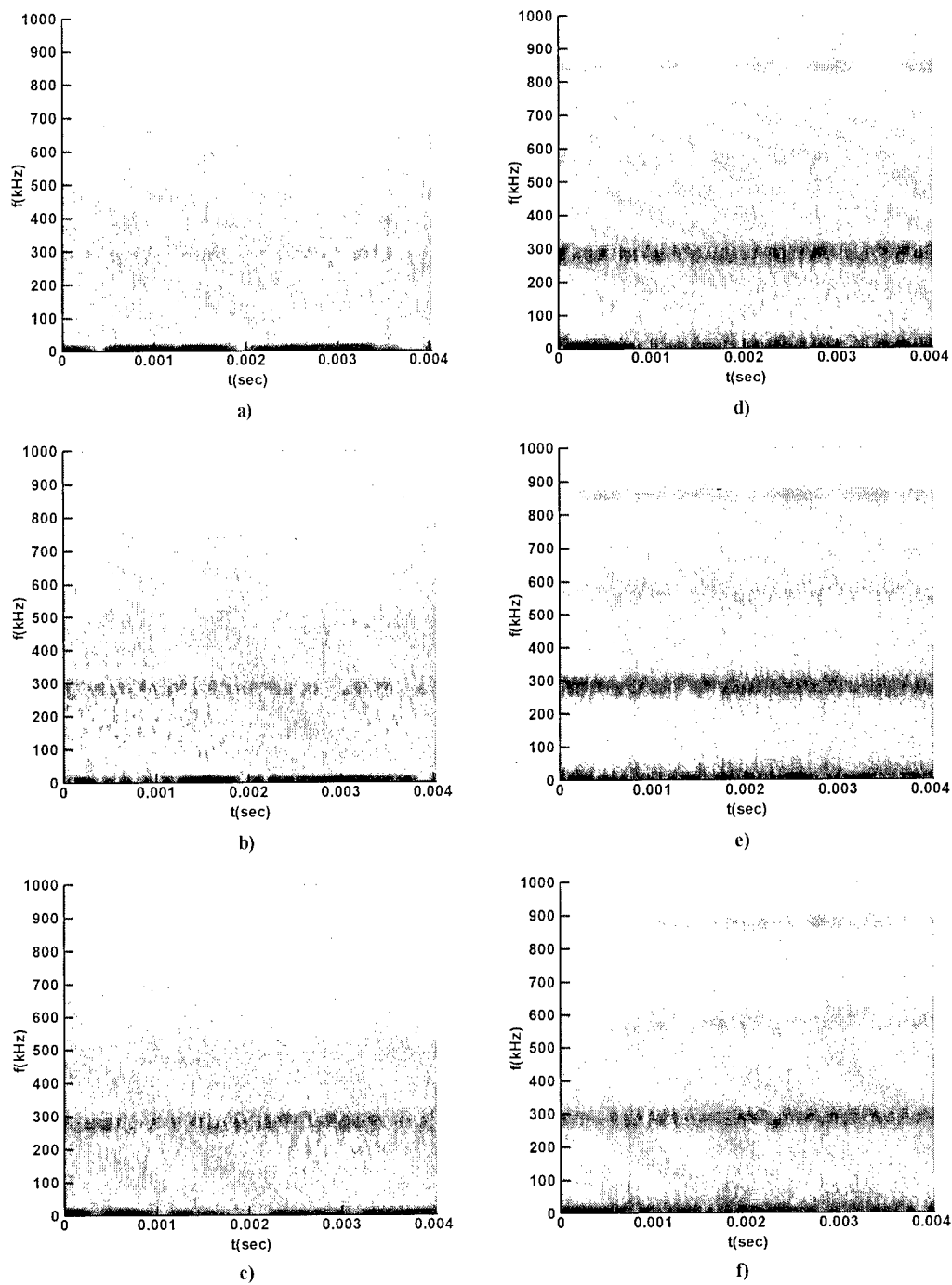


Figure 3.1 - Magnitude of STFT of hot-wire data for the baseline (91-6 adiabatic) case.

a) $R = 1609$, b) $R = 1680$, c) $R = 1749$, d) $R = 1815$, e) $R = 1879$, f) $R = 1940$.

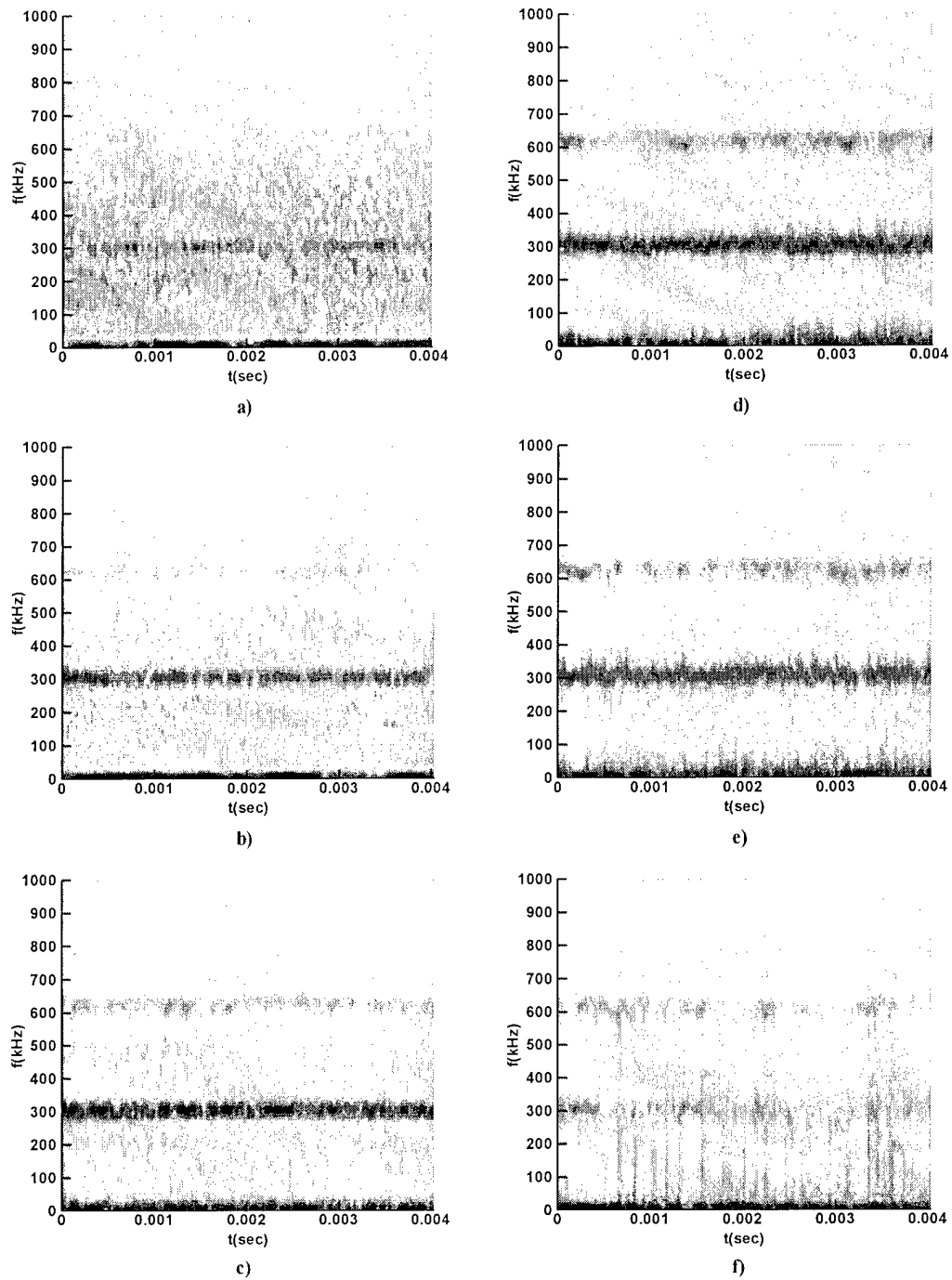


Figure 3.2 - Magnitude of STFT of hot-wire data for the cooled (91-6 cooled) case.
a) $R = 1609$, b) $R = 1680$, c) $R = 1749$, d) $R = 1815$, e) $R = 1879$, f) $R = 1940$.

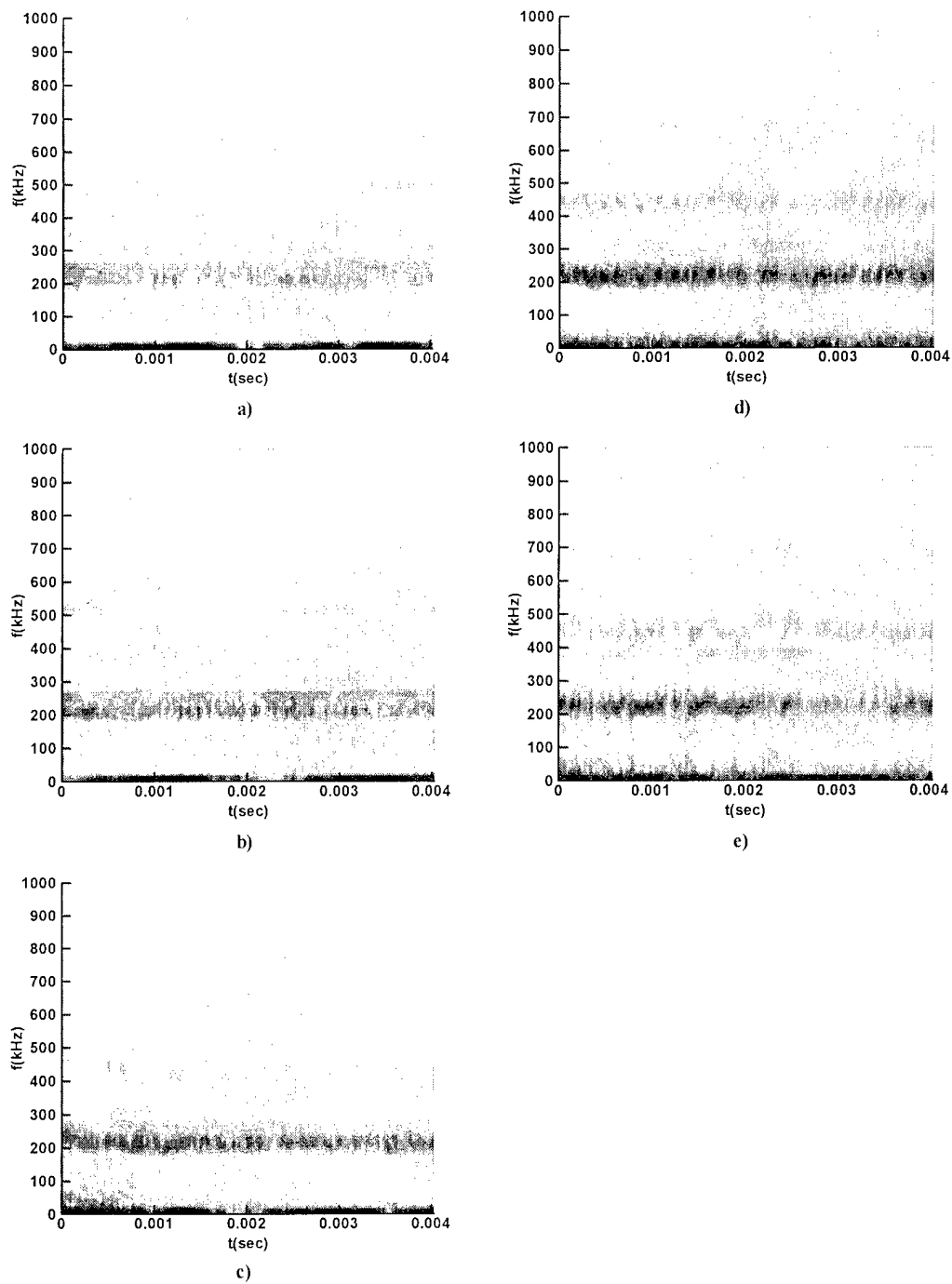


Figure 3.3 - Magnitude of STFT of hot-wire data for the 93-10 adiabatic case.
a) $R = 1879$, b) $R = 1940$, c) $R = 2000$, d) $R = 2058$, e) $R = 2114$.

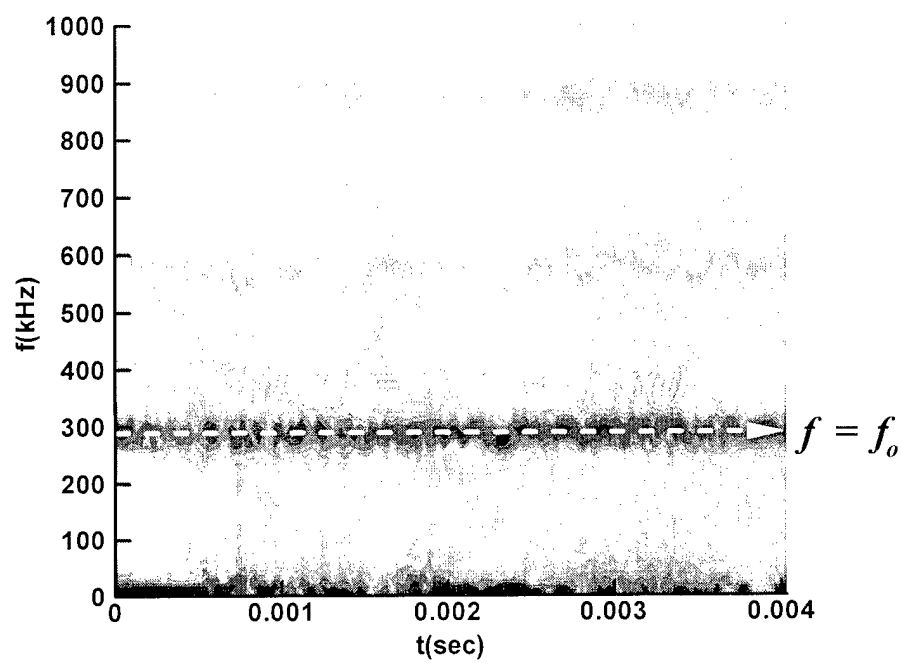


Figure 3.4 - Extraction of time series of the STFT at the second-mode frequency.

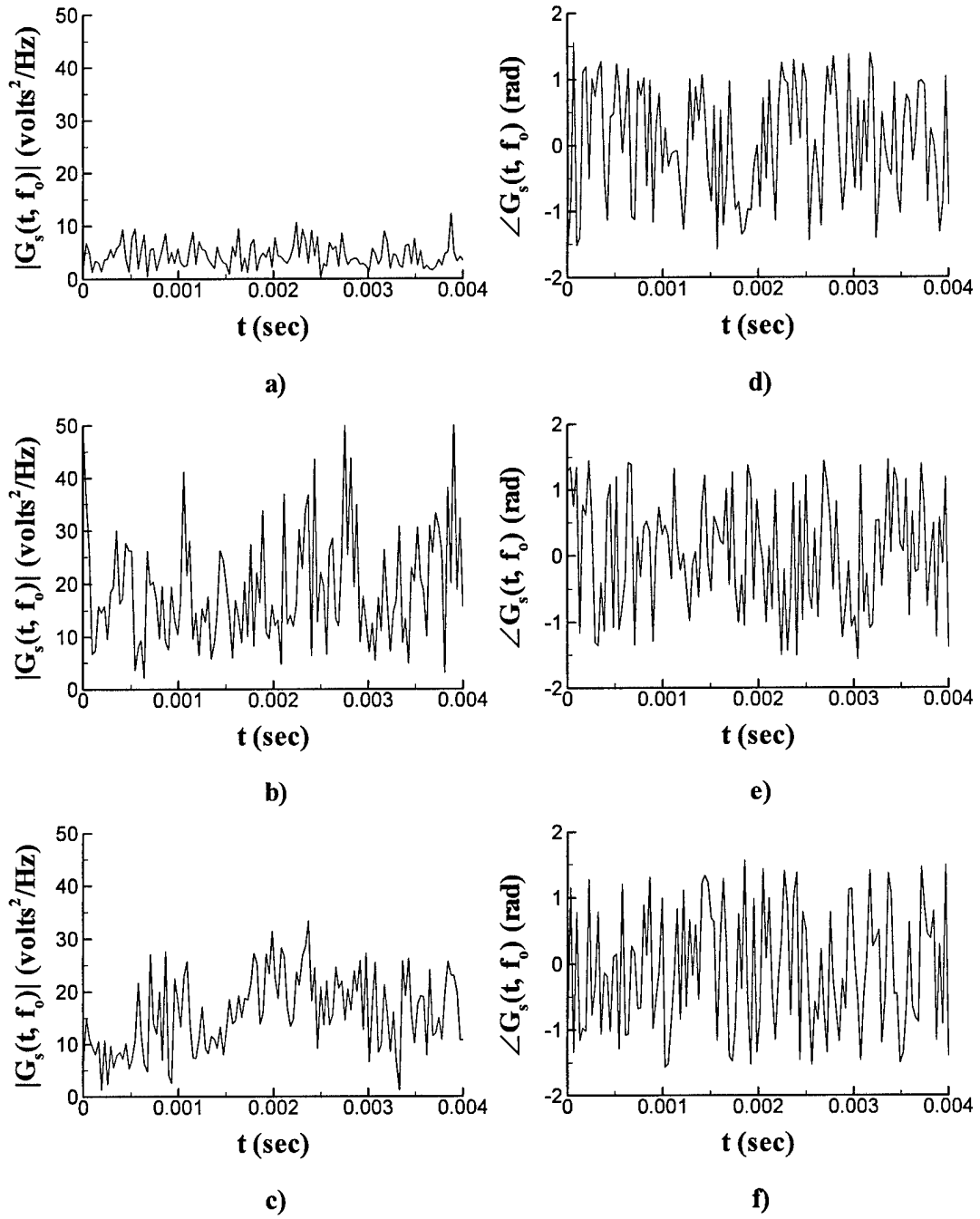


Figure 3.5 Amplitude (a-c) and phase (d-f) modulation of $G_s(t, f_0)$ for the baseline case (91-6 adiabatic cone), a) and d) $R = 1680$, b) and e) $R = 1815$, c) and f) $R = 1940$.

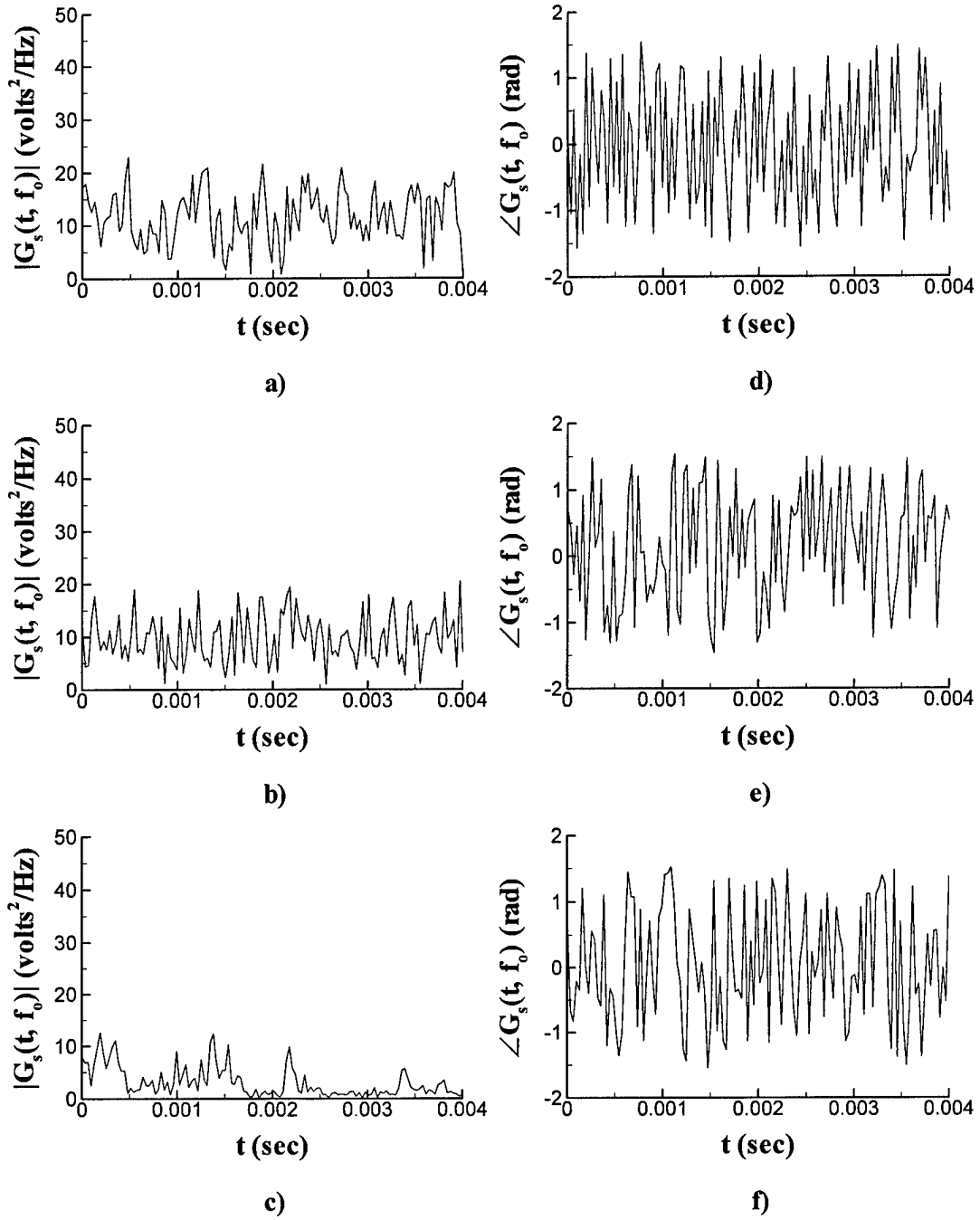


Figure 3.6 Amplitude (a-c) and phase (d-f) modulation of $G_s(t, f_0)$ for the 91-6 cooled cone, a) and d) $R = 1680$, b) and e) $R = 1815$, c) and f) $R = 1940$.

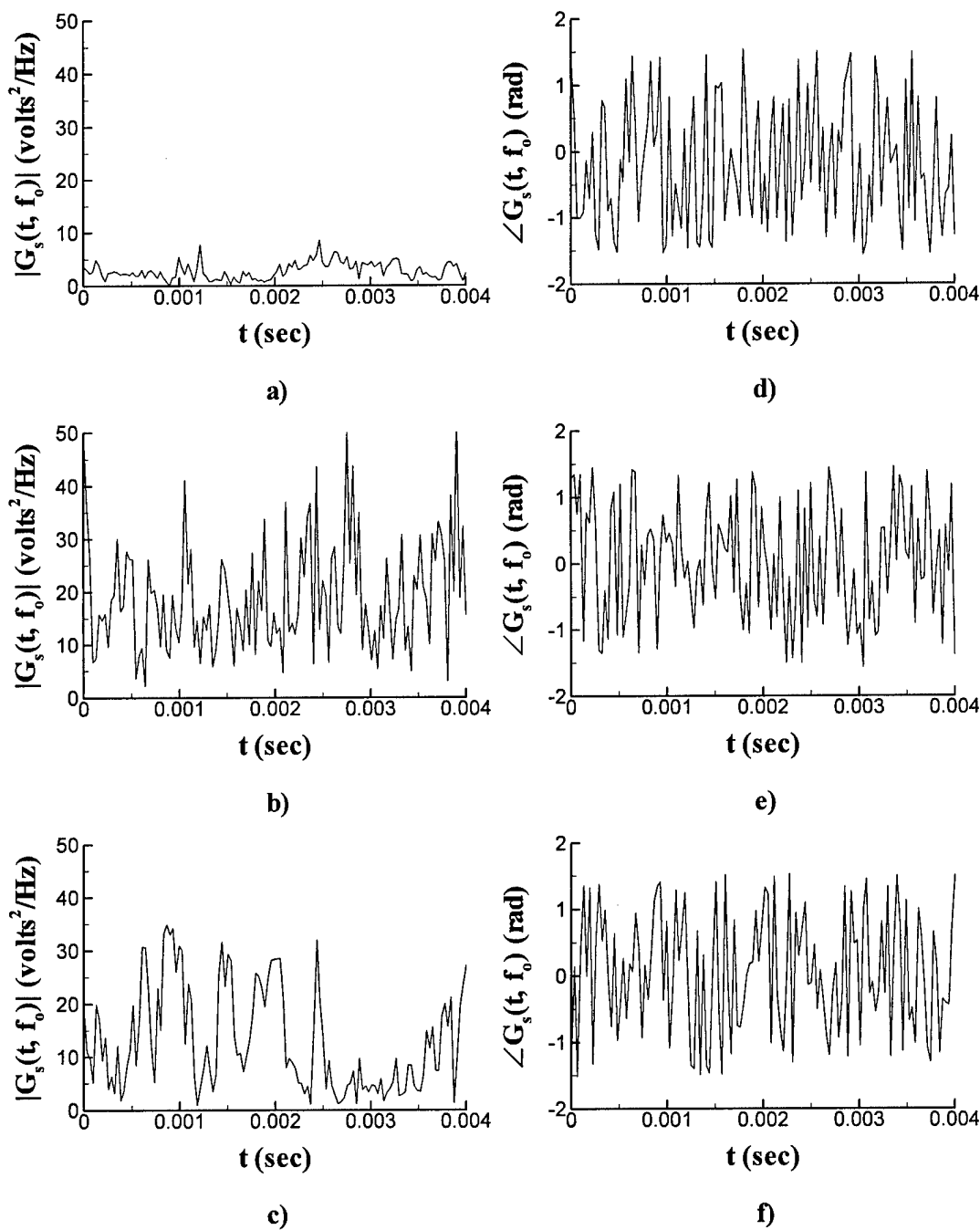
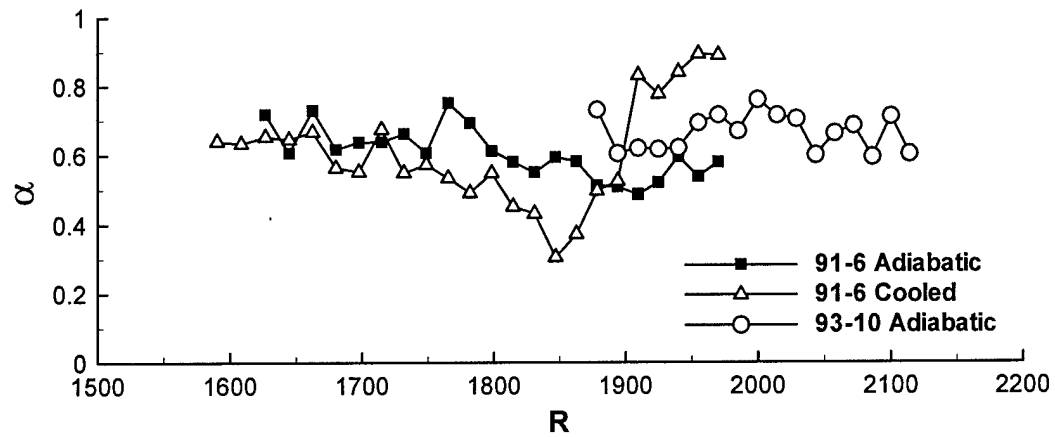
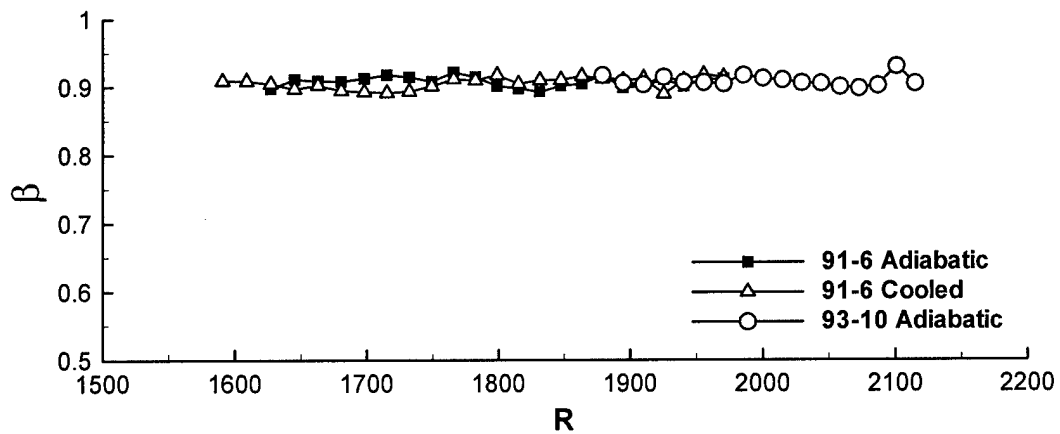


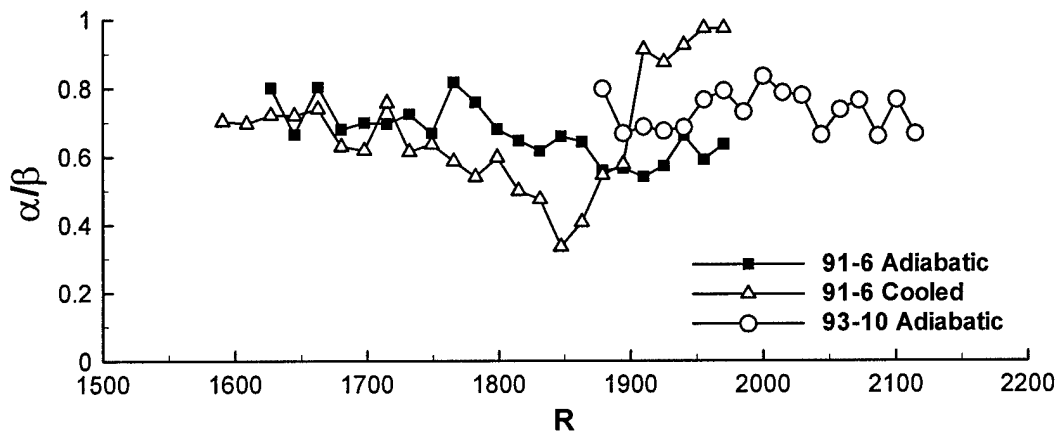
Figure 3.7 Amplitude (a-c) and phase (d-f) modulation of $G_s(t, f_0)$ for the 93-10 adiabatic cone, a) and d) $R = 1680$, b) and e) $R = 1815$, c) and f) $R = 1940$.



a)

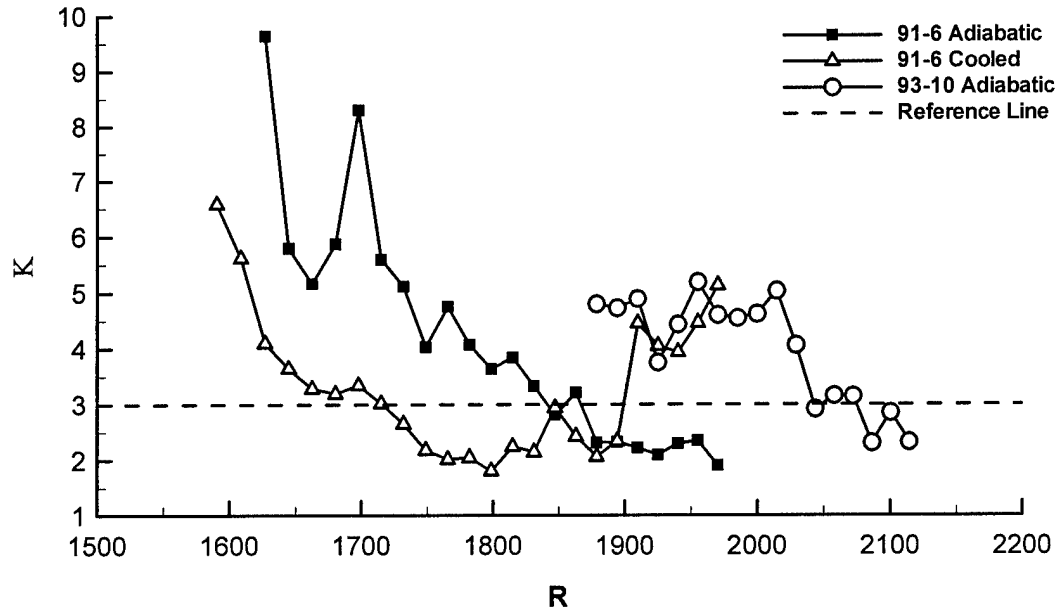


b)

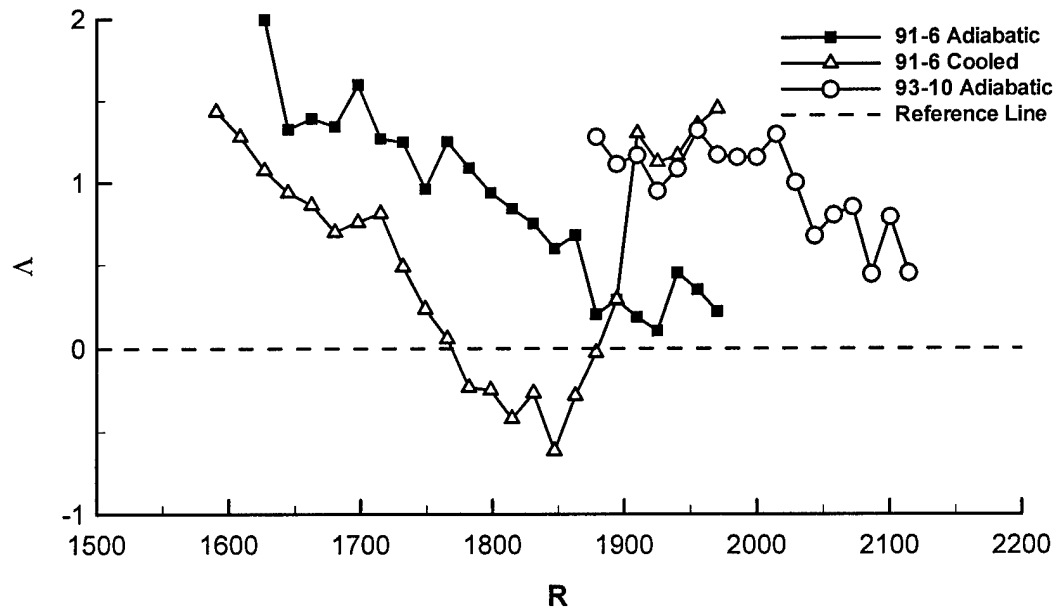


c)

Figure 3.8 - Effect of wall cooling and adverse pressure gradient on α , β , and α/β for $G_s(t, f_o)$.



a)



b)

Figure 3.9 - Effect of wall cooling and adverse pressure gradient on kurtosis and skewness of $G_s(t, f_o)$.

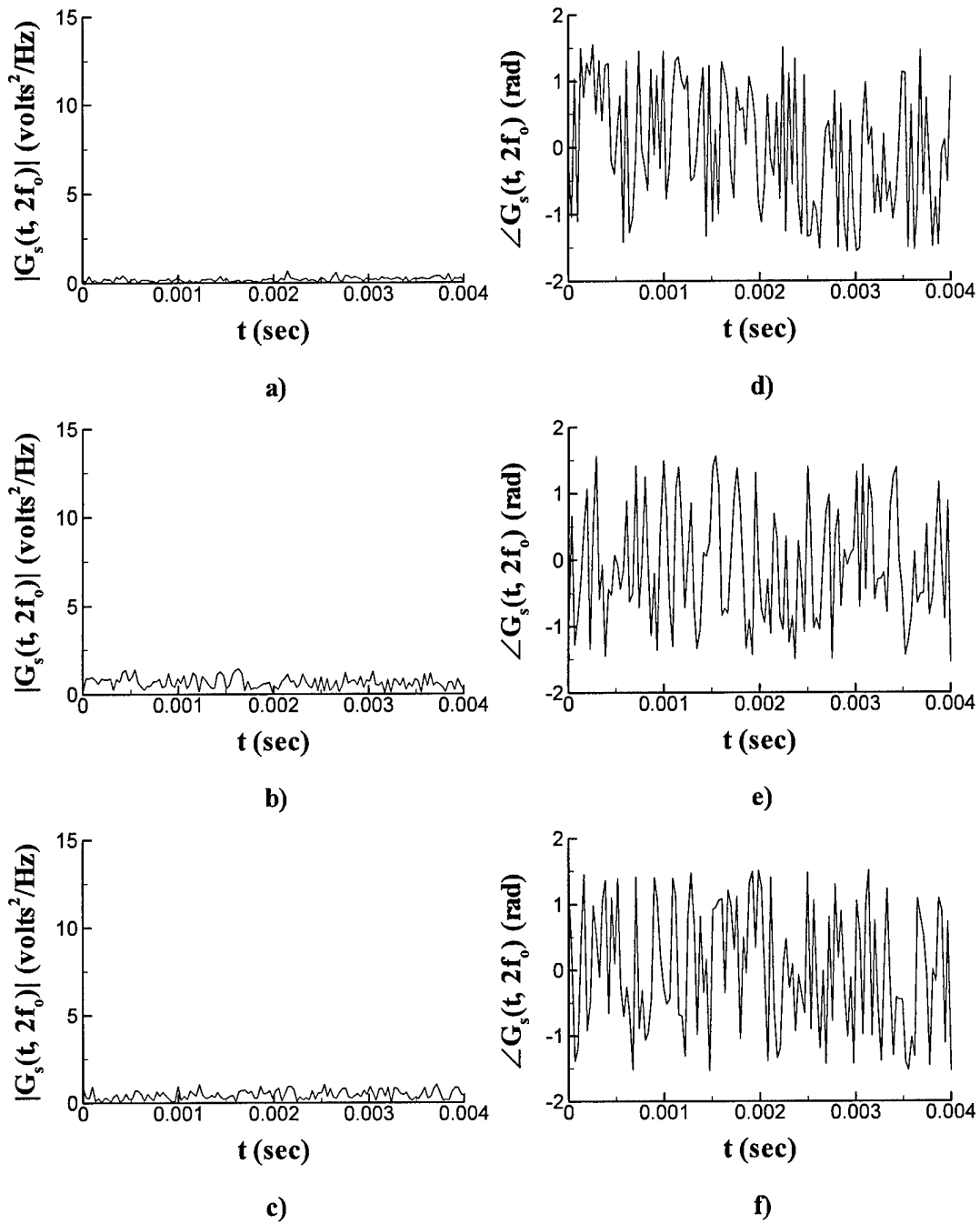


Figure 3.10 Amplitude (a-c) and phase (d-f) modulation of $G_s(t, 2f_0)$ for the baseline case (91-6 adiabatic cone), a) and d) $R = 1815$, b) and e) $R = 1879$, c) and f) $R = 1940$.

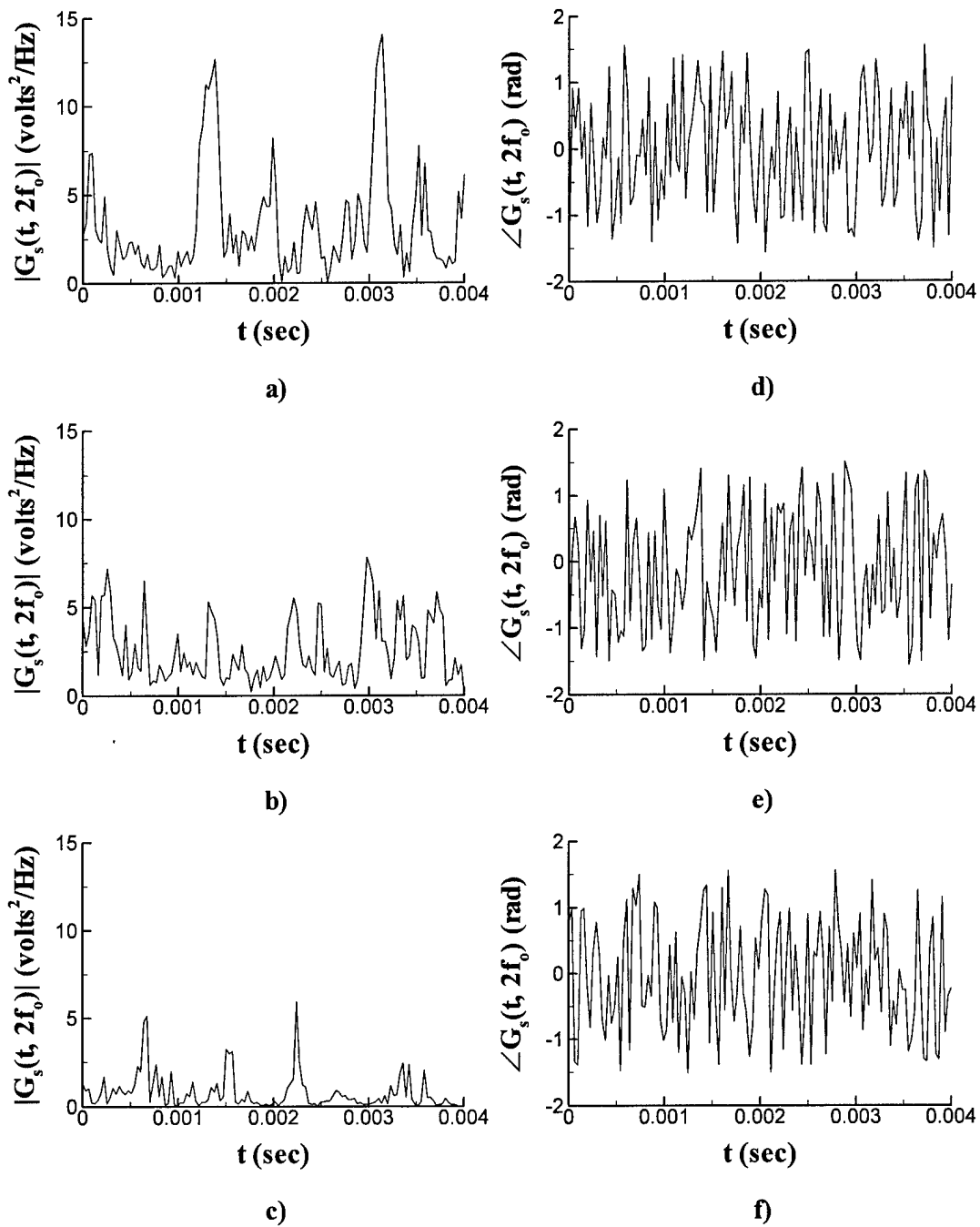


Figure 3.11 Amplitude (a-c) and phase (d-f) modulation of $G_s(t, f_0)$ for the 91-6 cooled cone, a) and d) $R = 1815$, b) and e) $R = 1879$, c) and f) $R = 1940$.

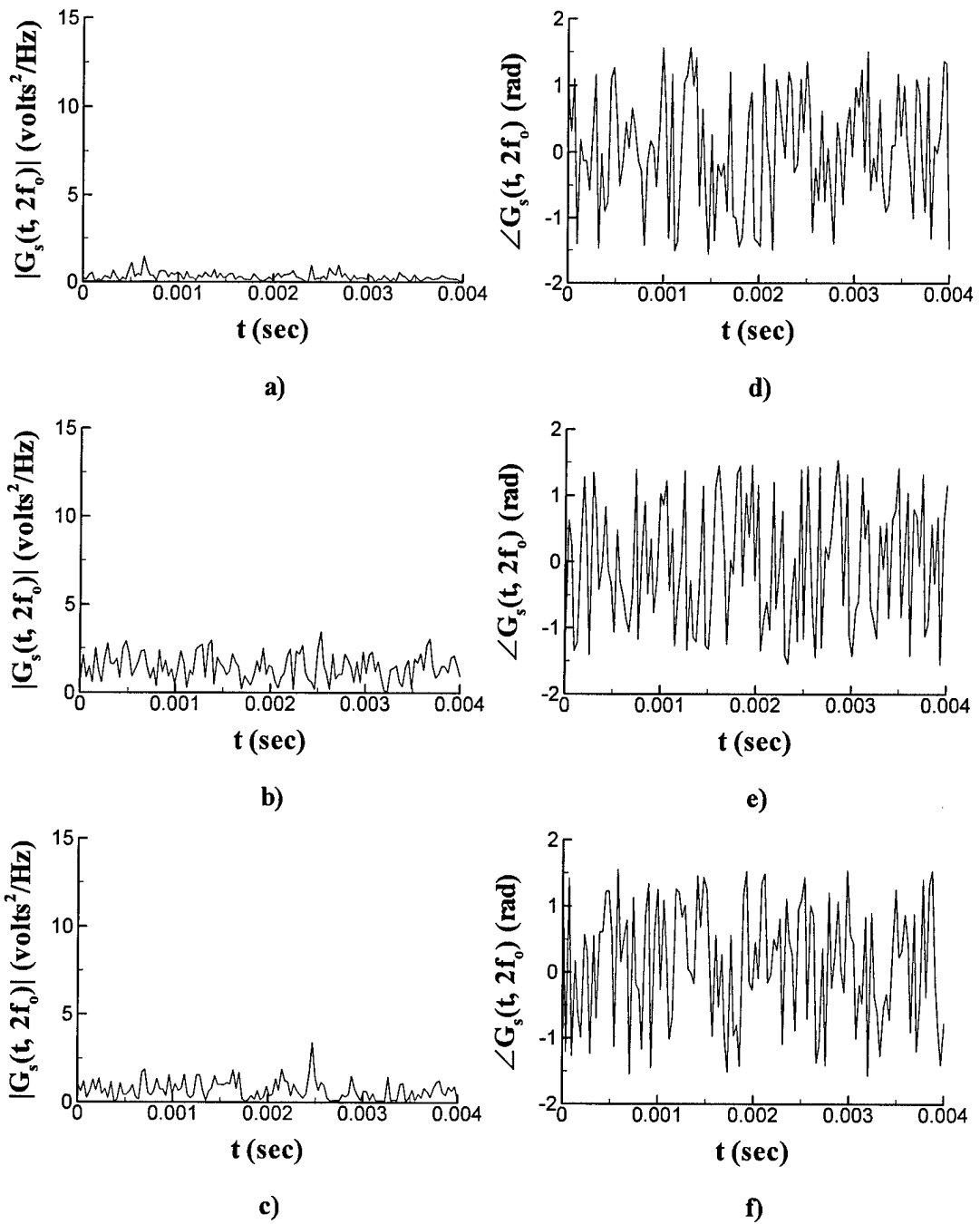
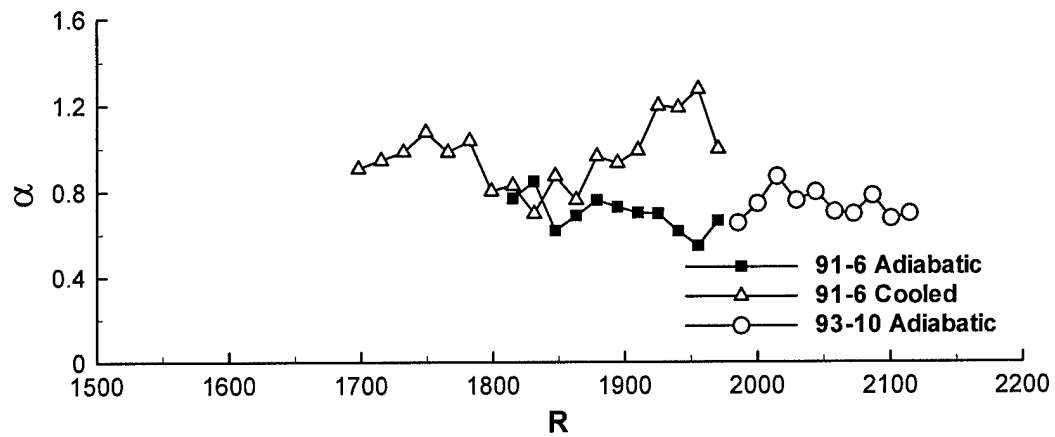
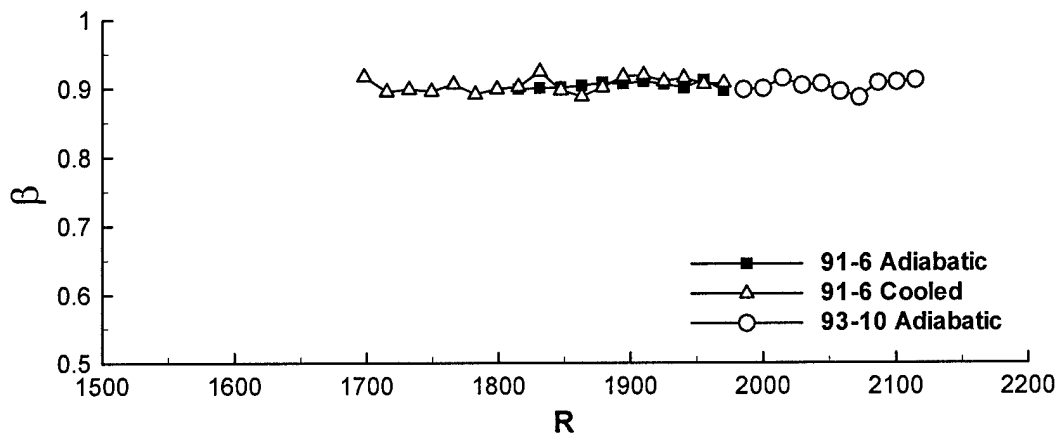


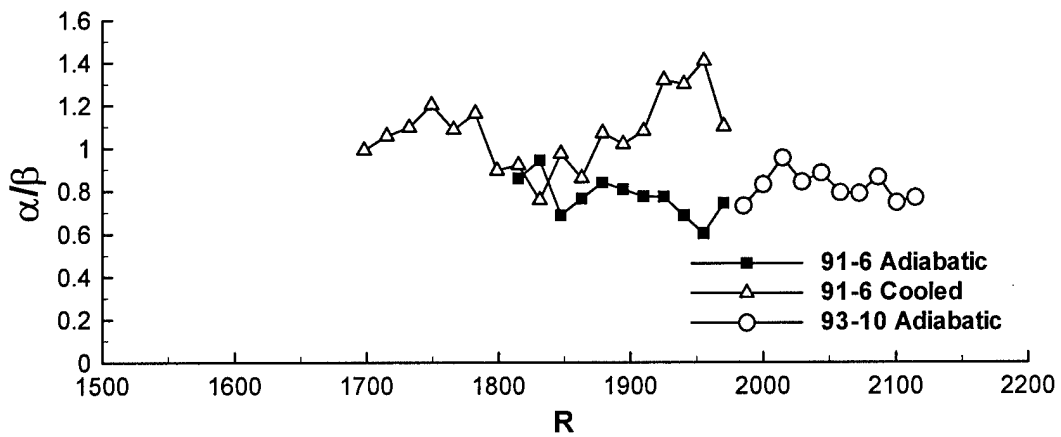
Figure 3.12 Amplitude (a-c) and phase (d-f) modulation of $G_s(t, f_0)$ for the 93-10 adiabatic cone, a) and d) $R = 2000$, b) and e) $R = 2058$, c) and f) $R = 2114$.



a)

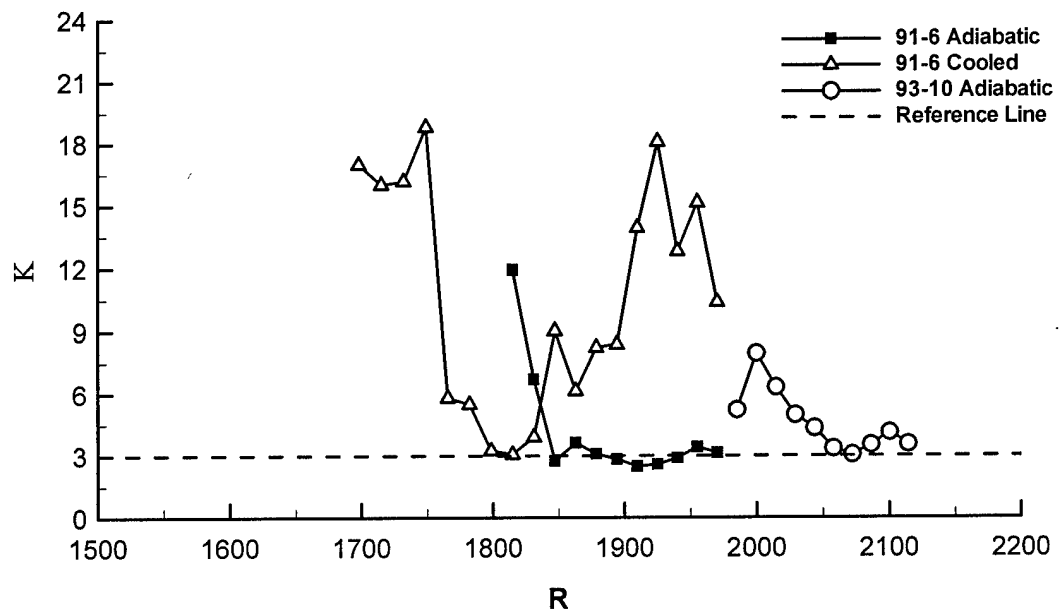


b)

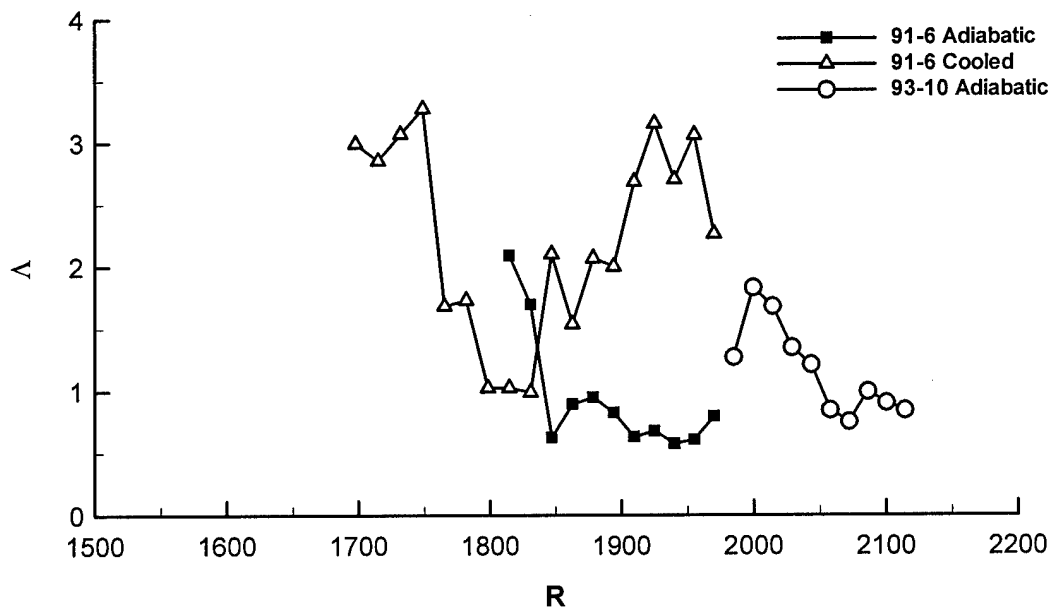


c)

Figure 3.13 - Effect of wall cooling and adverse pressure gradient on α , β , and α/β for $G_s(t, 2f_o)$.



a)



b)

Figure 3.14 - Effect of wall cooling and adverse pressure gradient on kurtosis and skewness $G_s(t, 2f_o)$.

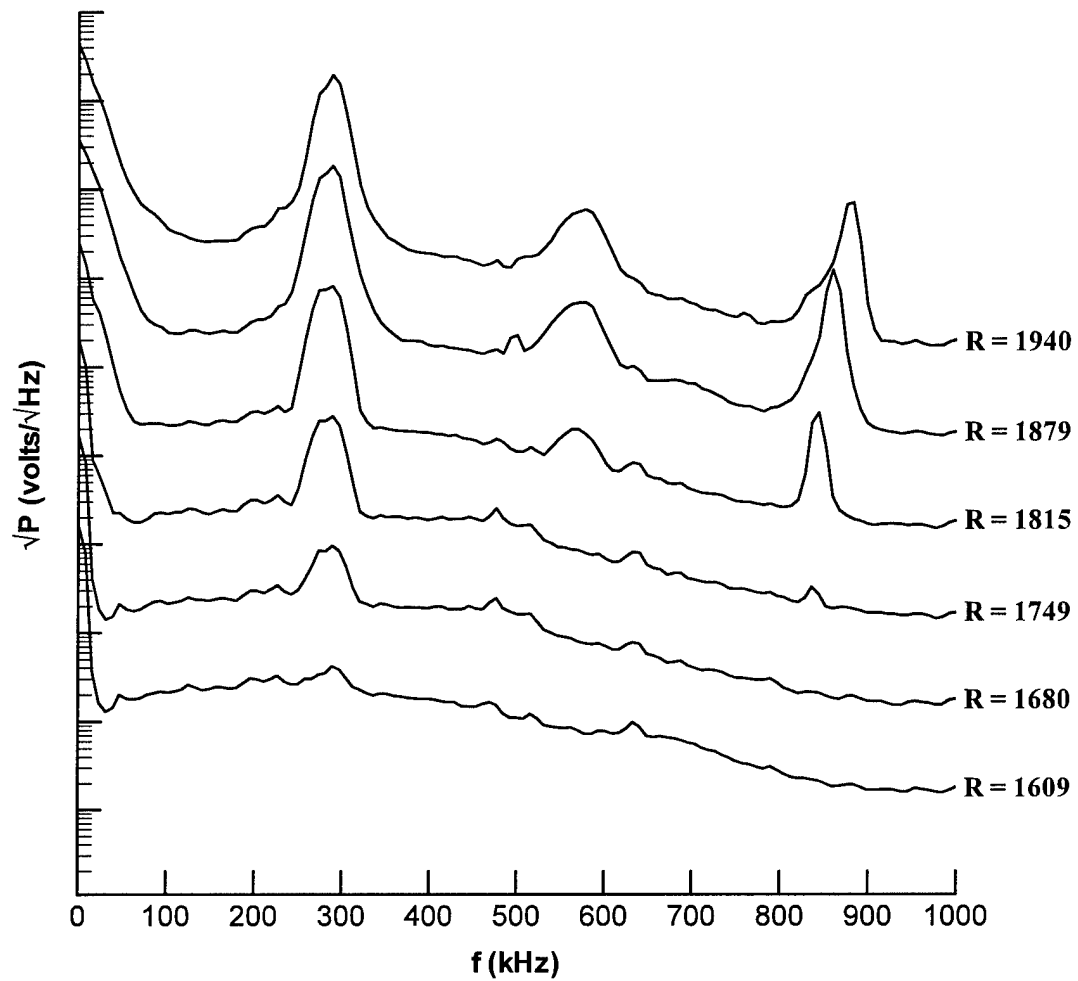


Figure 3.15 - Power Spectra of the baseline (91-6 adiabatic) case. Subsequent spectra are shifted up one decade for clarity.

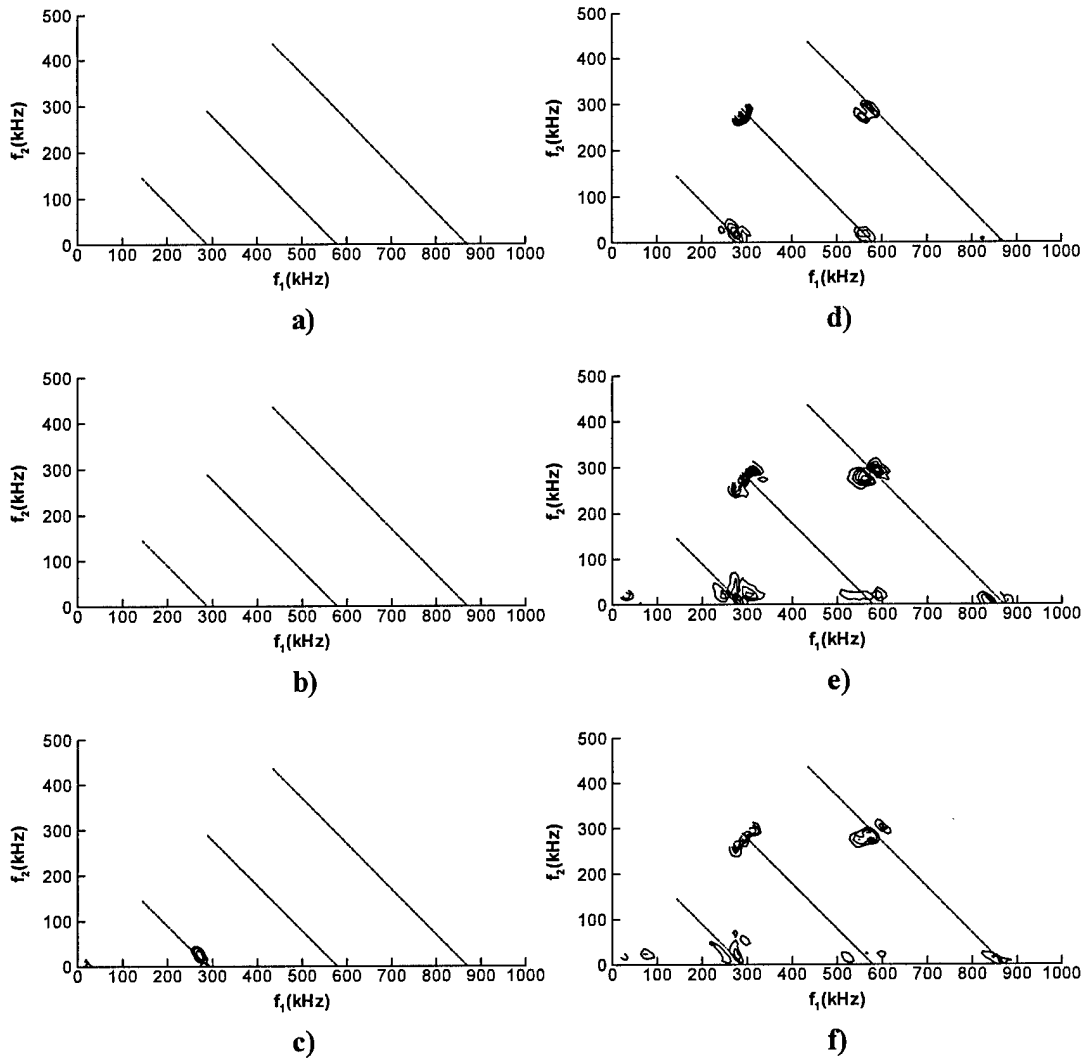


Figure 3.16 - Fourier bispectrum of the baseline (91-6 adiabatic) case.
a) $R = 1609$, b) $R = 1680$, c) $R = 1749$, d) $R = 1815$, e) $R = 1879$, f) $R = 1940$.

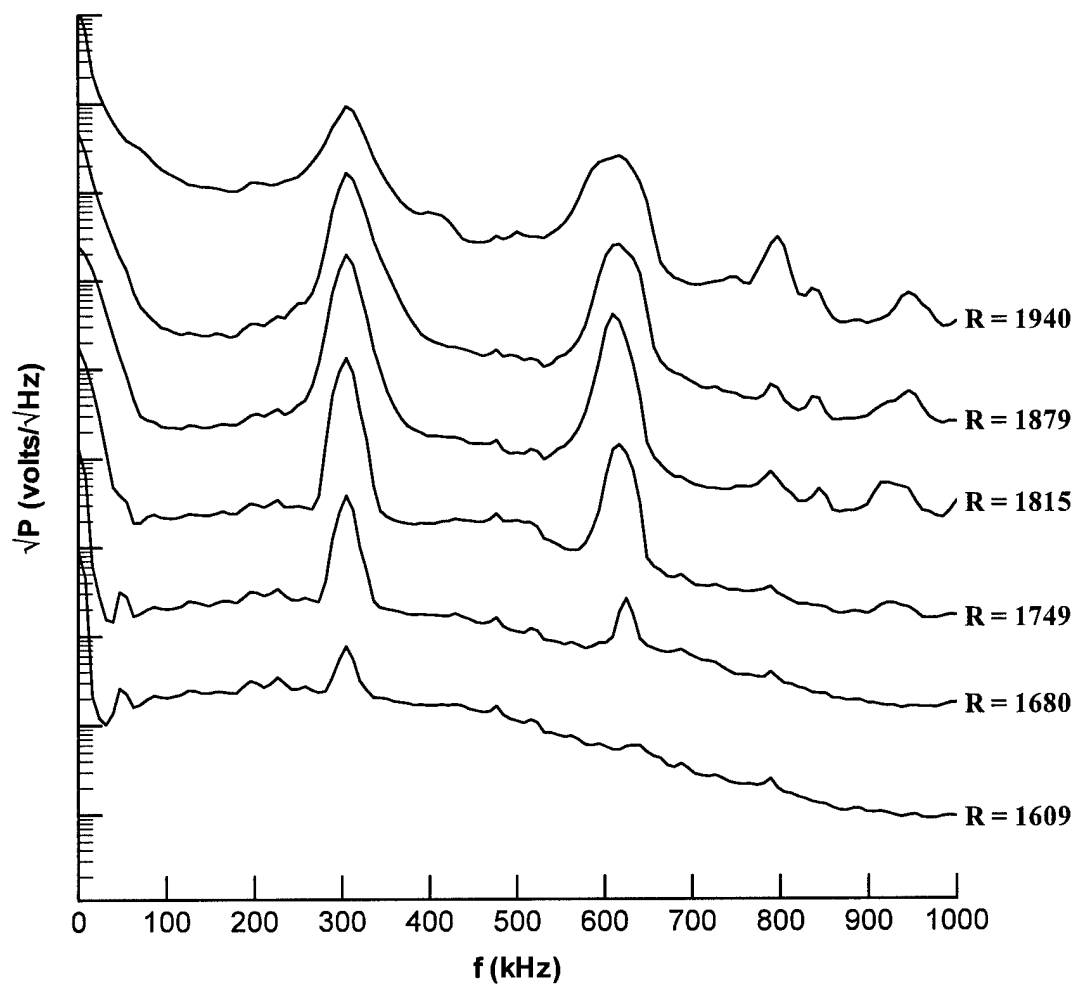


Figure 3.17 - Power Spectra of the 91-6 cooled wall model. Subsequent spectra are shifted up one decade for clarity.

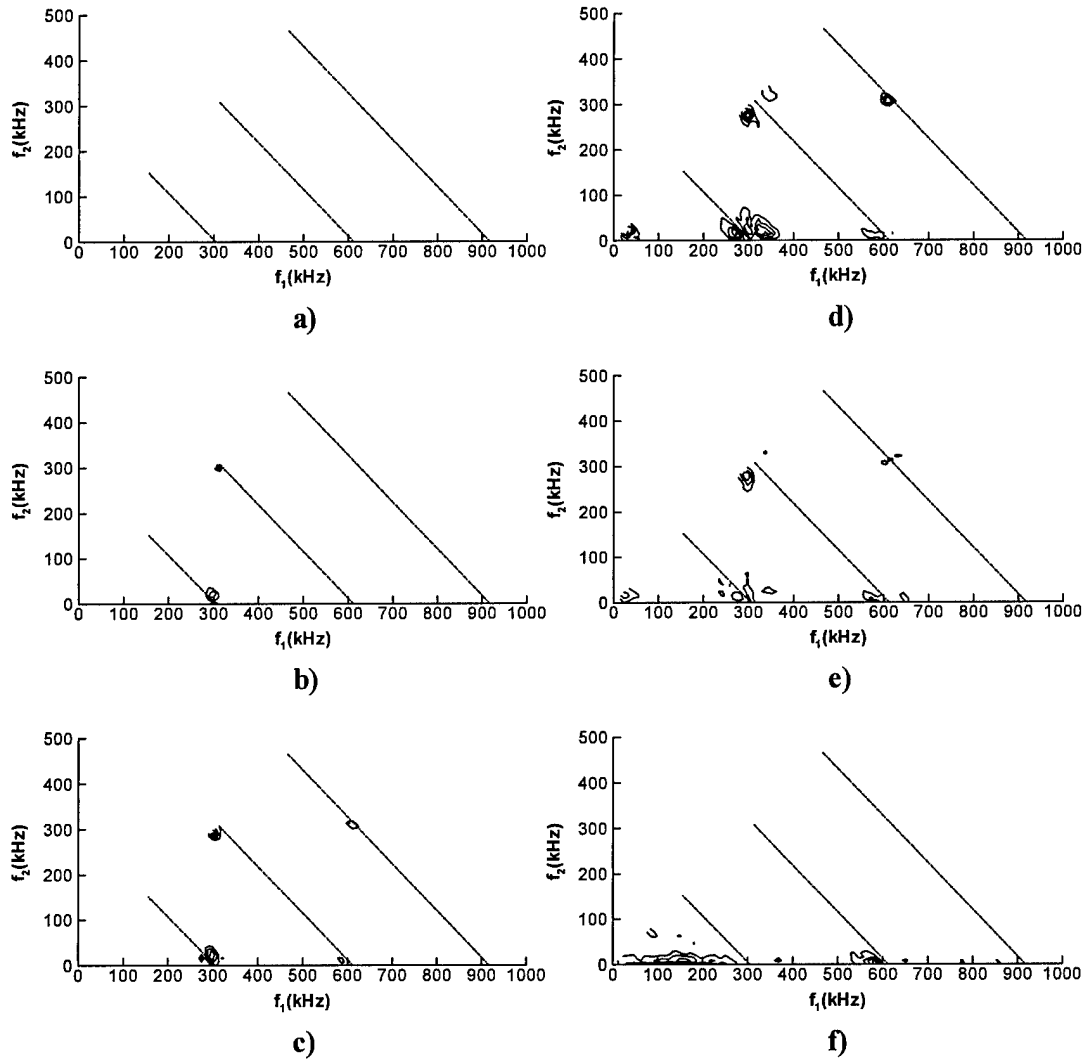


Figure 3.18 - Fourier bispectrum of the 91-6 cooled wall model.
a) $R = 1609$, b) $R = 1680$, c) $R = 1749$, d) $R = 1815$, e) $R = 1879$, f) $R = 1940$.

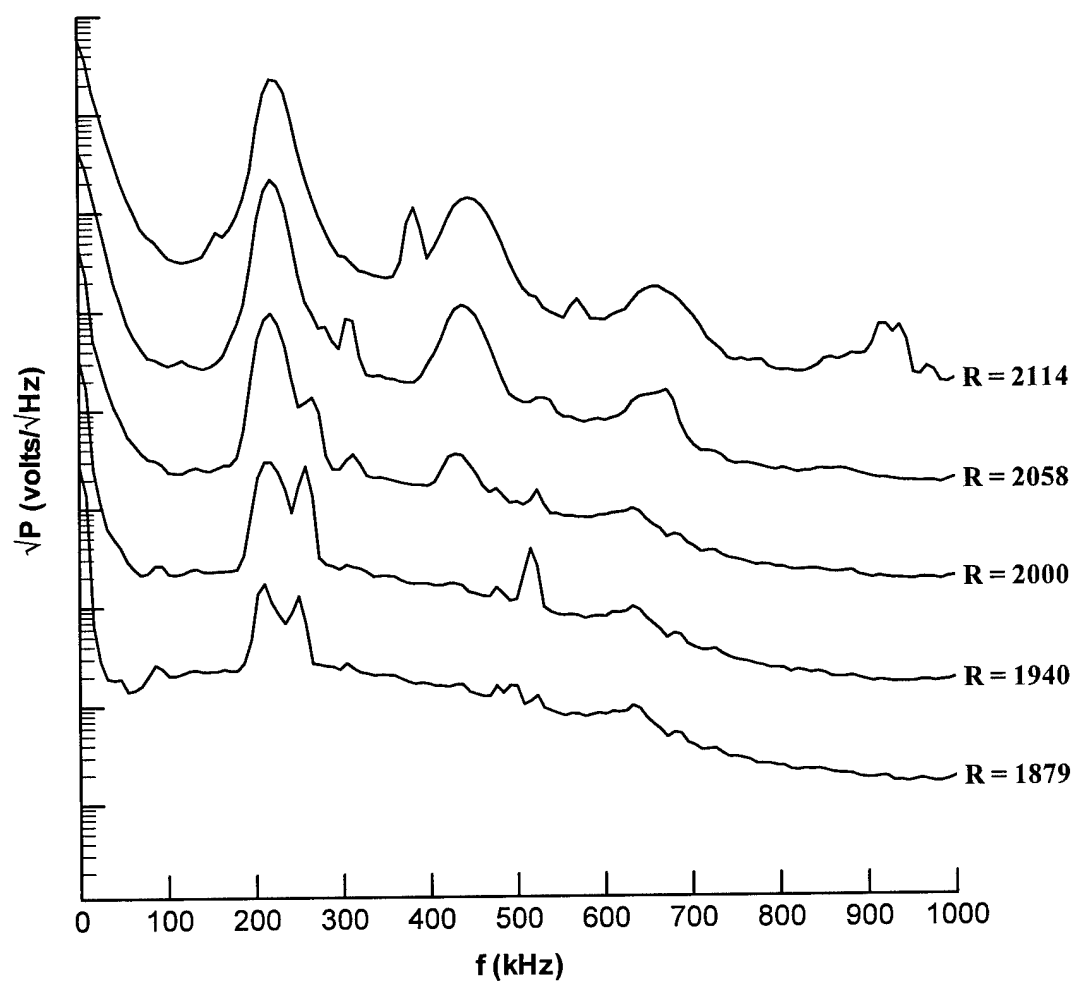


Figure 3.19 - Power Spectra of the 93-10 Adiabatic model. Subsequent spectra are shifted up one decade for clarity.

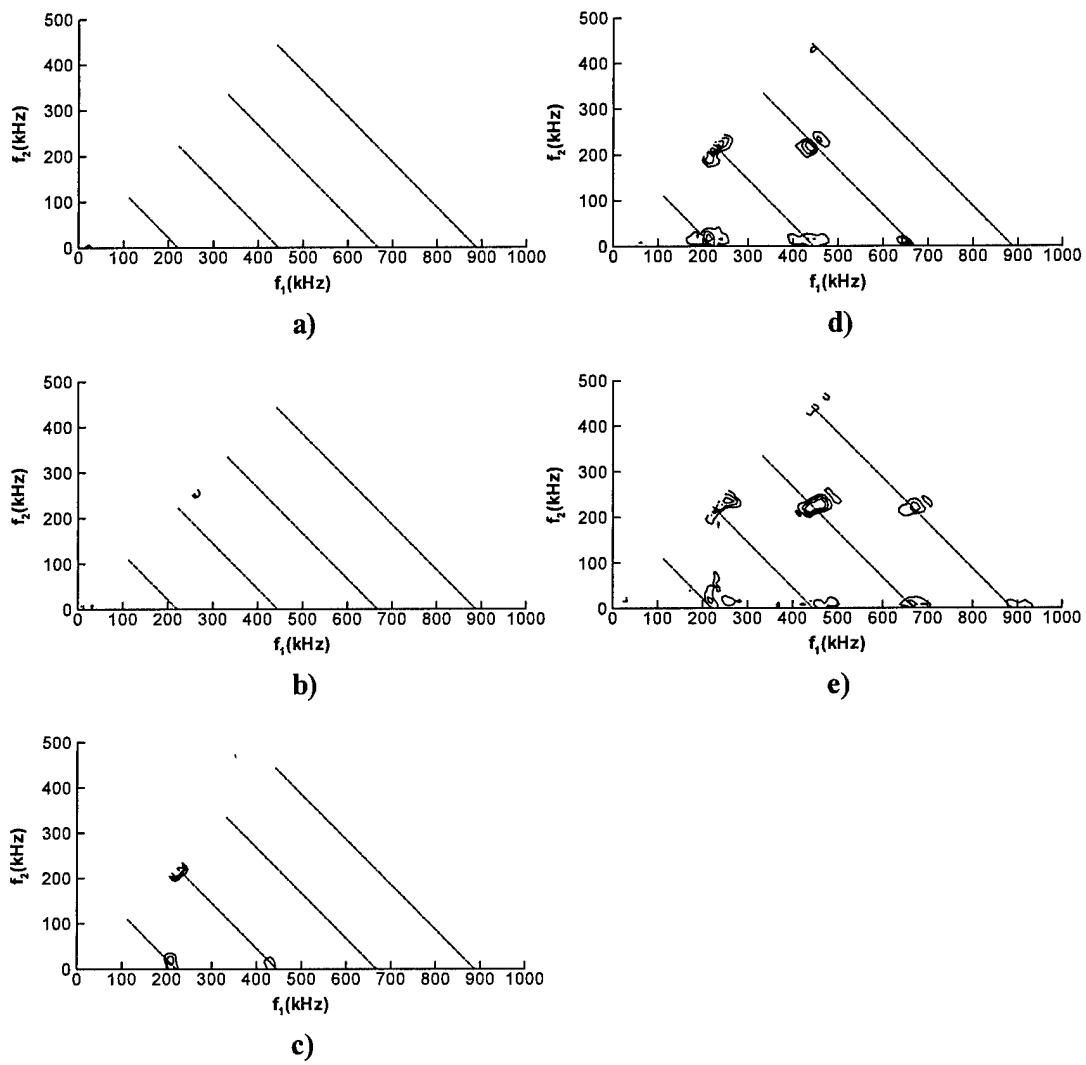


Figure 3.20 - Fourier bispectrum of the 93-10 Adiabatic model.
a) $R = 1879$, b) $R = 1940$, c) $R = 2000$, d) $R = 2058$, e) $R = 2114$.

This page deliberately left blank.

Next numbered page is page 98.

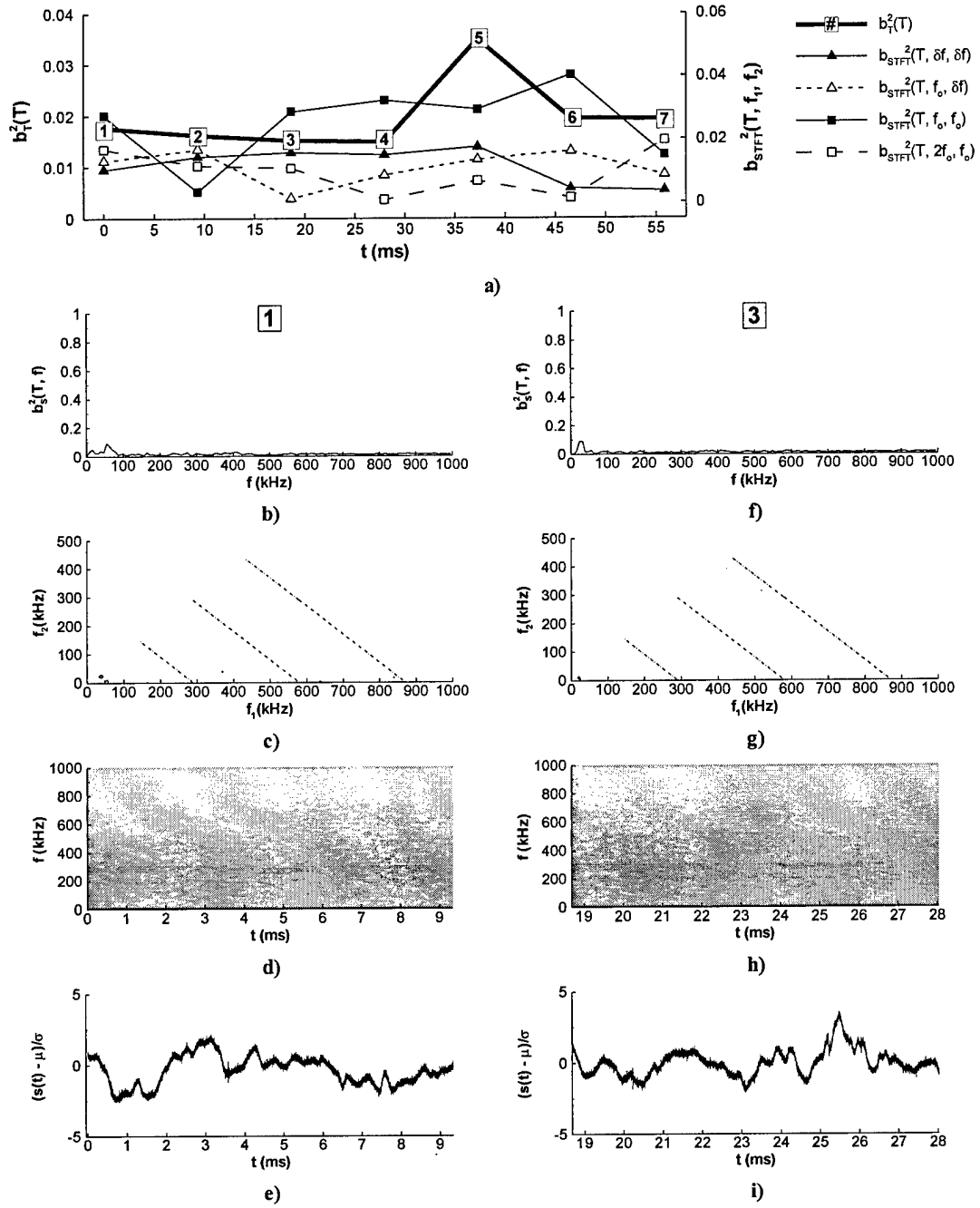


Figure 3.21 - Baseline case (91-6 adiabatic model), $R = 1609$, a) total bispectrum, b) and f) summed bispectrum, c) and g) STFT bispectrum, d) and h) magnitude of STFT, e) and i) normalized time series.

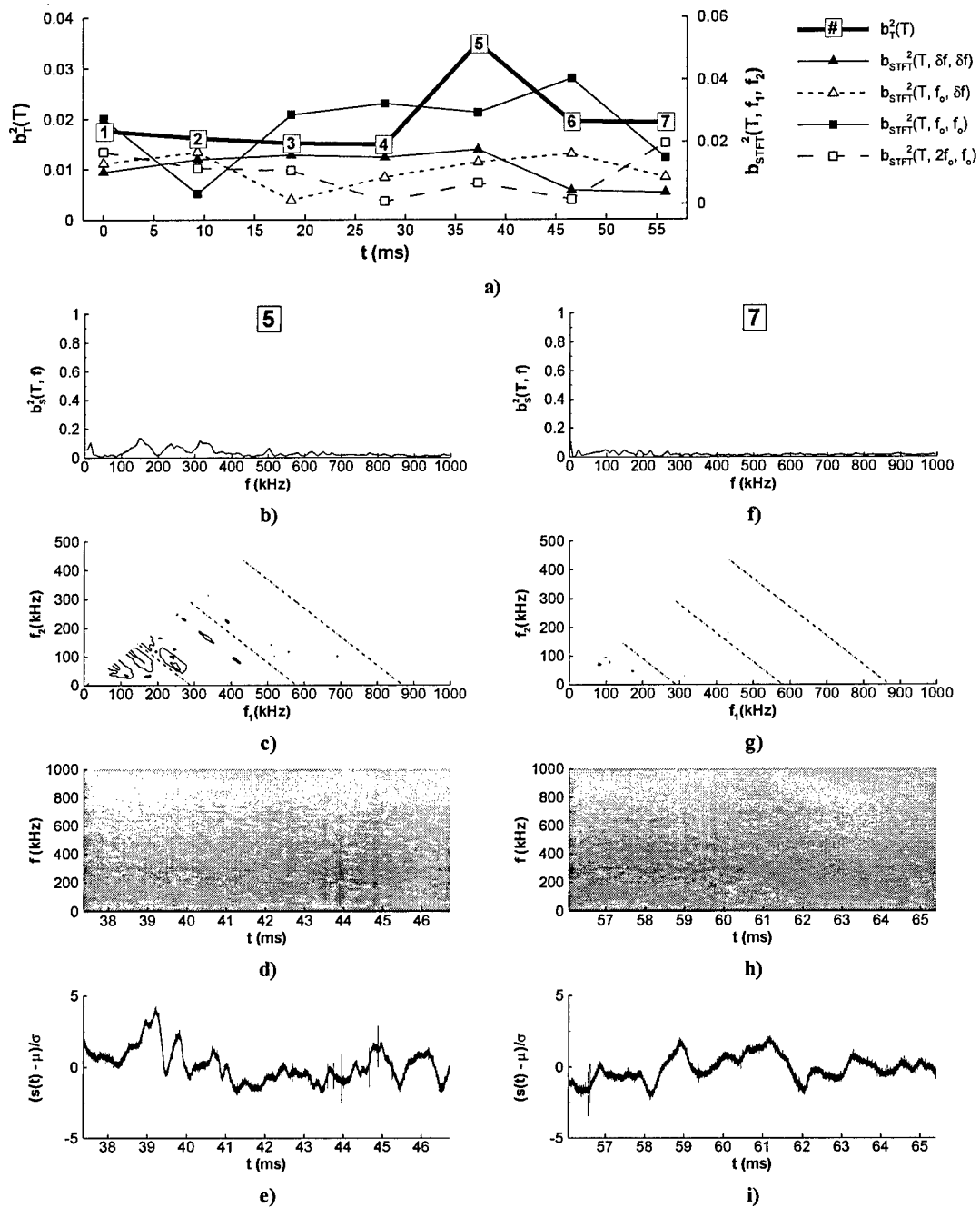


Figure 3.22 - Baseline case (91-6 adiabatic model), $R = 1609$, a) total bispectrum, b) and f) summed bispectrum, c) and g) STFT bispectrum, d) and h) magnitude of STFT, e) and i) normalized time series.

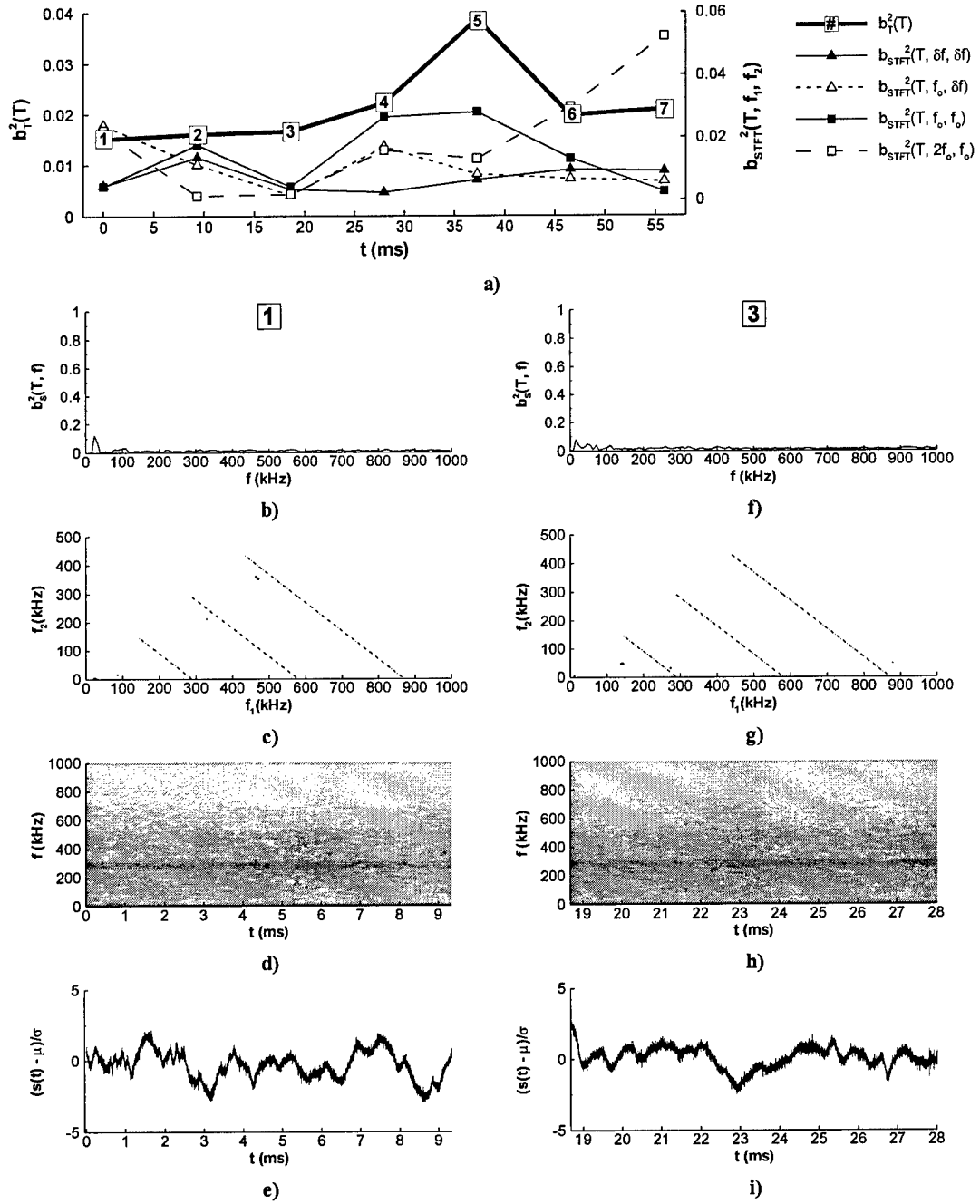


Figure 3.23 - Baseline case (91-6 adiabatic model), $R = 1680$, a) total bispectrum, b) and f) summed bispectrum, c) and g) STFT bispectrum, d) and h) magnitude of STFT, e) and i) normalized time series.

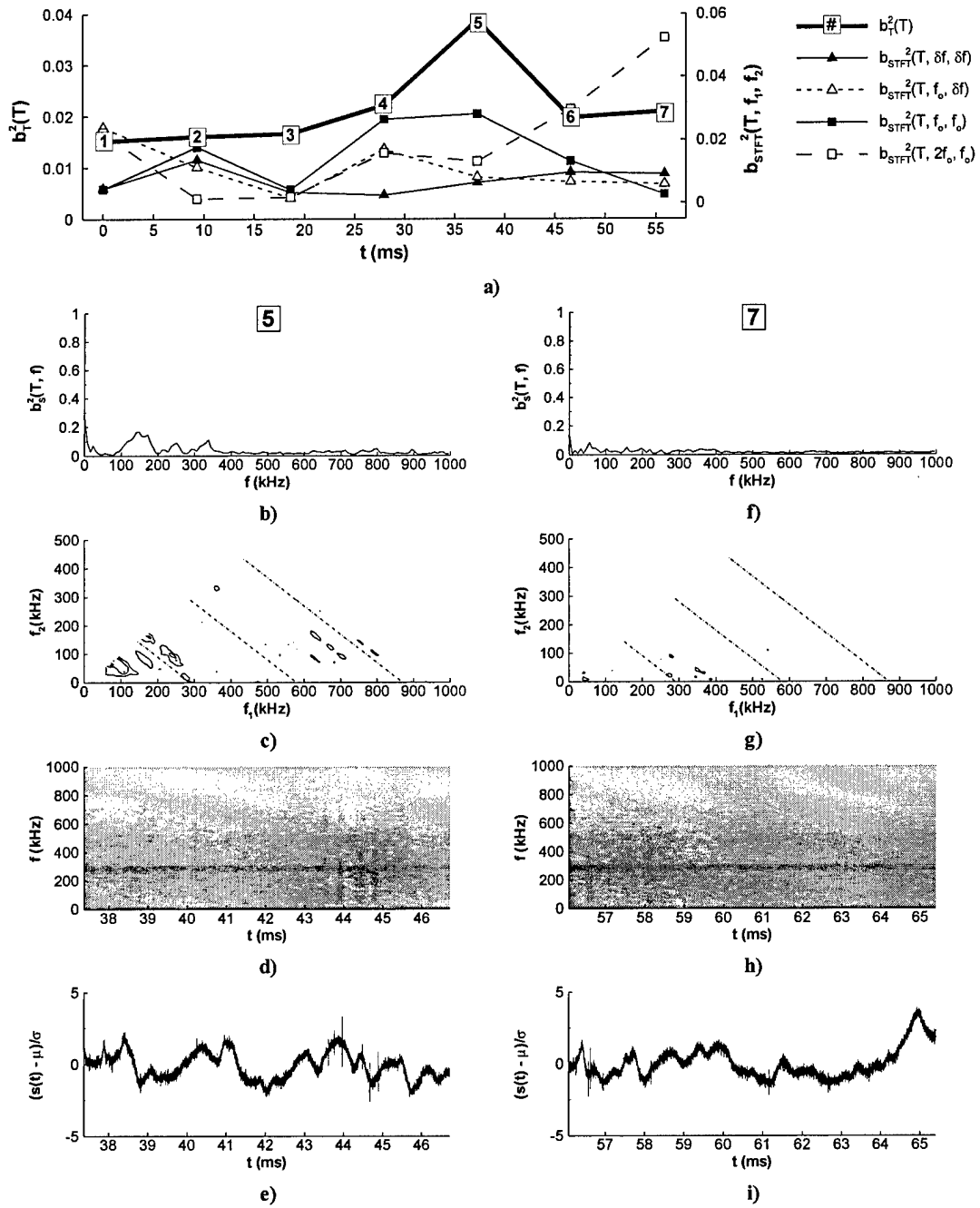


Figure 3.24 - Baseline case (91-6 adiabatic model), $R = 1680$, a) total bispectrum, b) and f) summed bispectrum, c) and g) STFT bispectrum, d) and h) magnitude of STFT, e) and i) normalized time series.

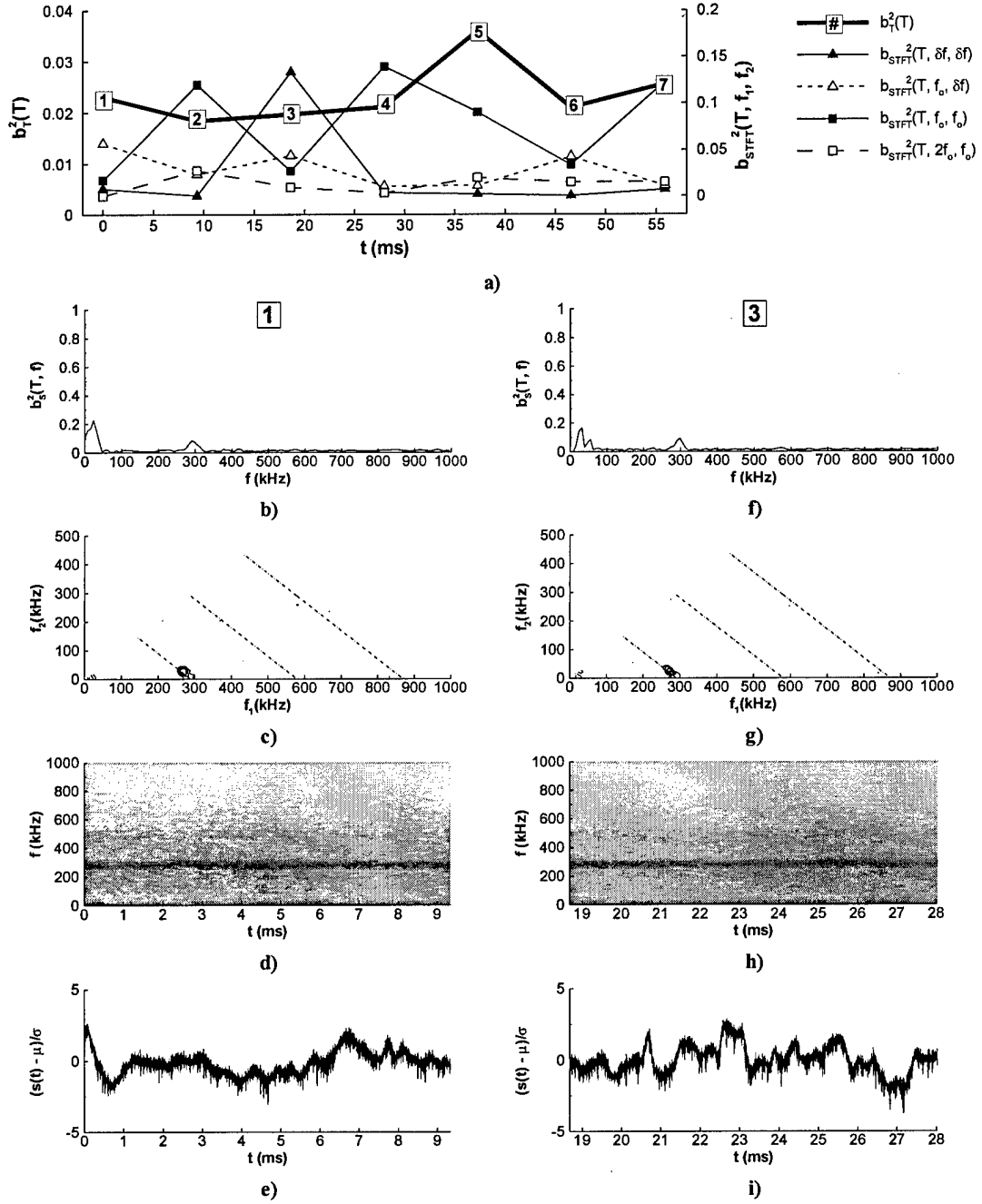


Figure 3.25 - Baseline case (91-6 adiabatic model), $R = 1749$, a) total bispectrum, b) and f) summed bispectrum, c) and g) STFT bispectrum, d) and h) magnitude of STFT, e) and i) normalized time series.

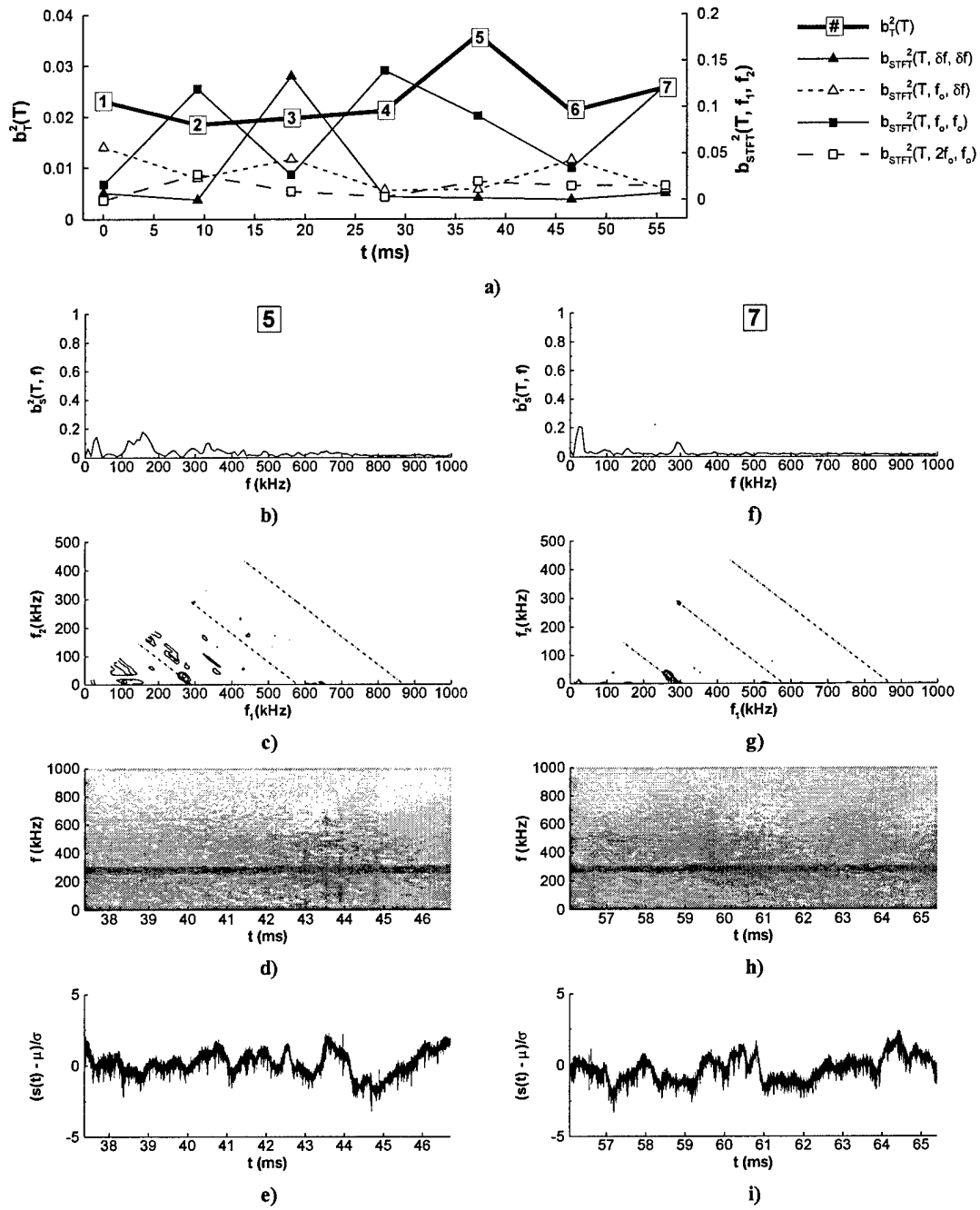


Figure 3.26 - Baseline case (91-6 adiabatic model), $R = 1749$, a) total bispectrum, b) and f) summed bispectrum, c) and g) STFT bispectrum, d) and h) magnitude of STFT, e) and i) normalized time series.

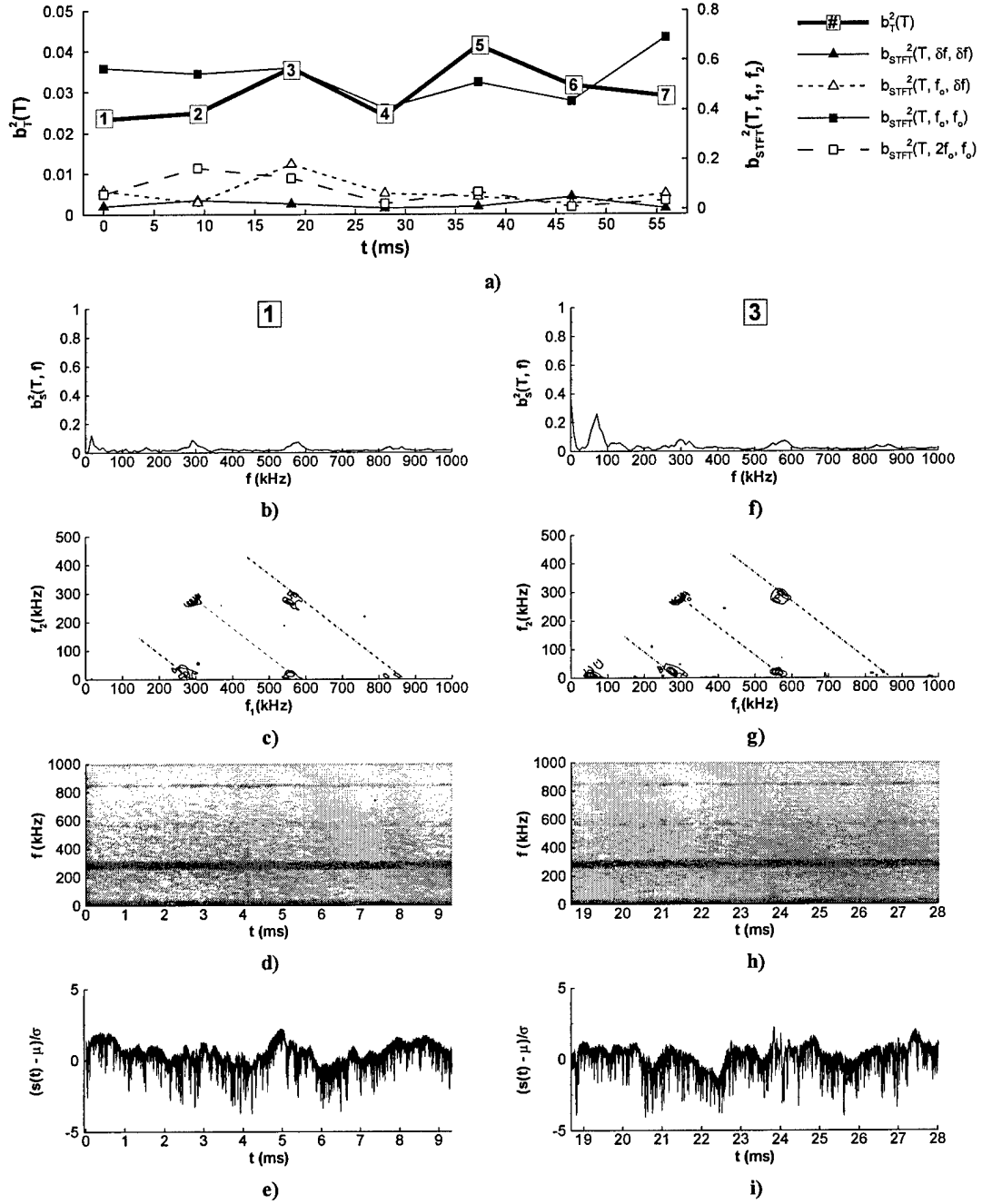


Figure 3.27 - Baseline case (91-6 adiabatic model), $R = 1815$, a) total bispectrum, b) and f) summed bispectrum, c) and g) STFT bispectrum, d) and h) magnitude of STFT, e) and i) normalized time series.

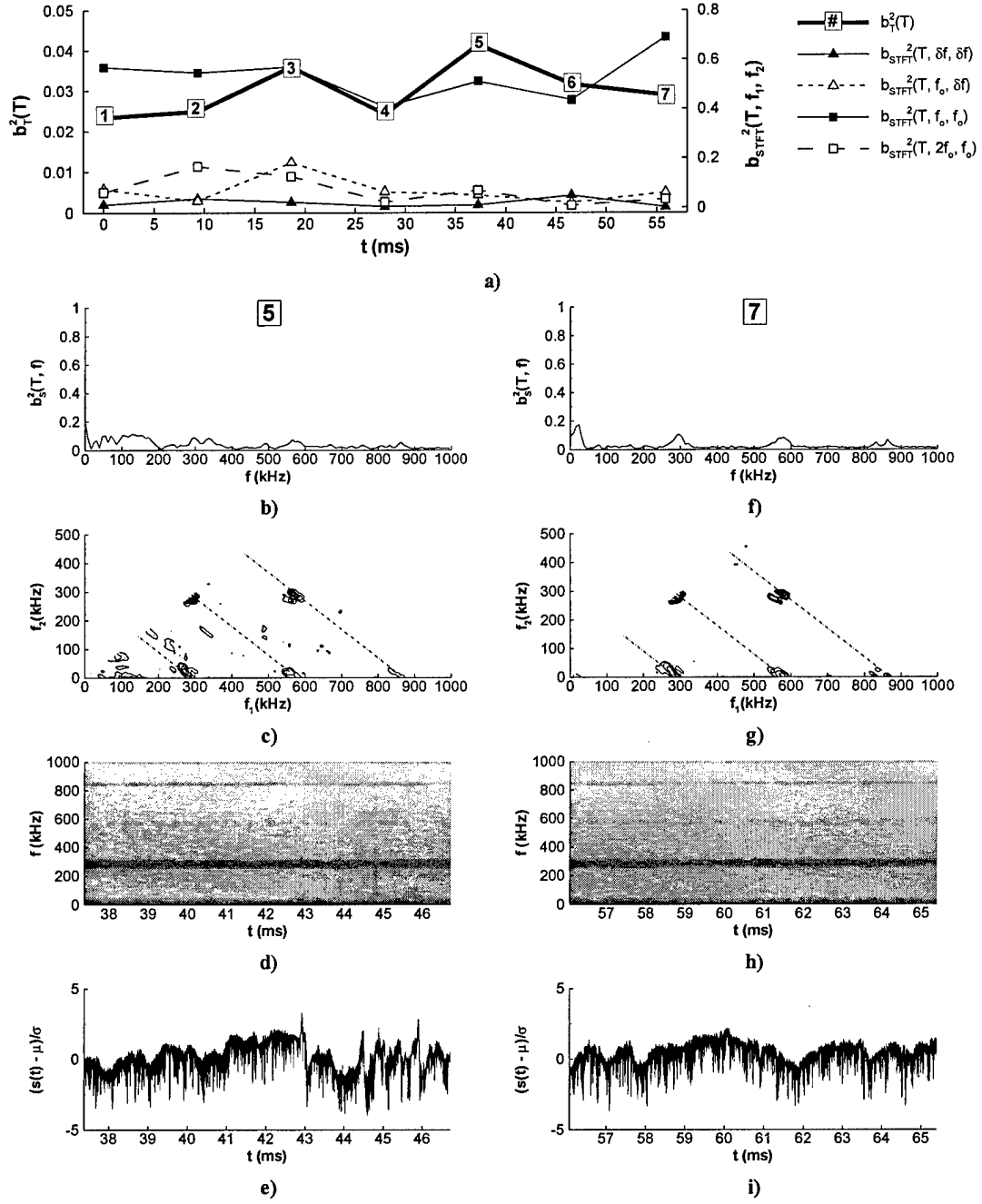


Figure 3.28 - Baseline case (91-6 adiabatic model), $R = 1815$, a) total bispectrum, b) and f) summed bispectrum, c) and g) STFT bispectrum, d) and h) magnitude of STFT, e) and i) normalized time series.

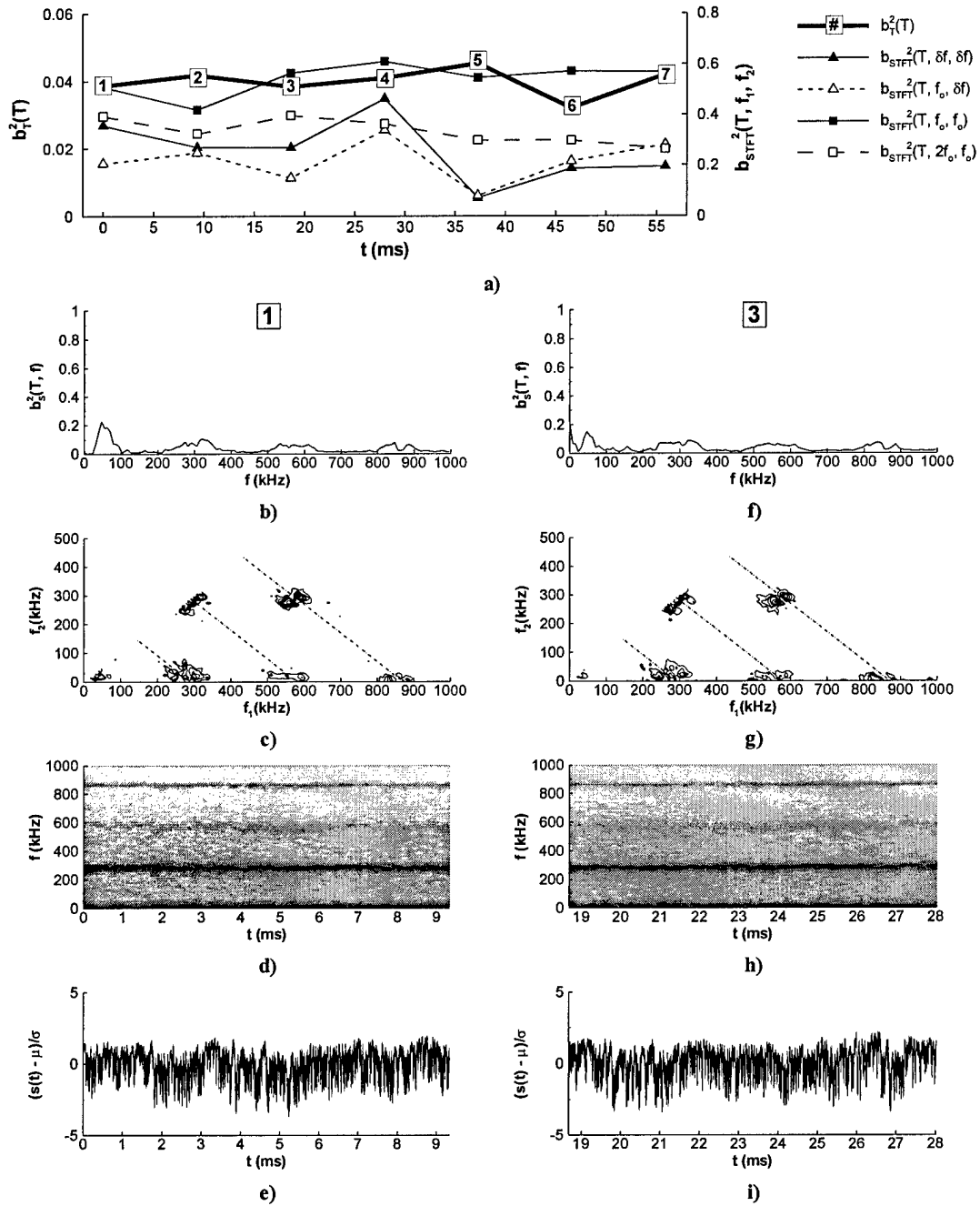


Figure 3.29 - Baseline case (91-6 adiabatic model), $R = 1879$, a) total bispectrum, b) and f) summed bispectrum, c) and g) STFT bispectrum, d) and h) magnitude of STFT, e) and i) normalized time series.

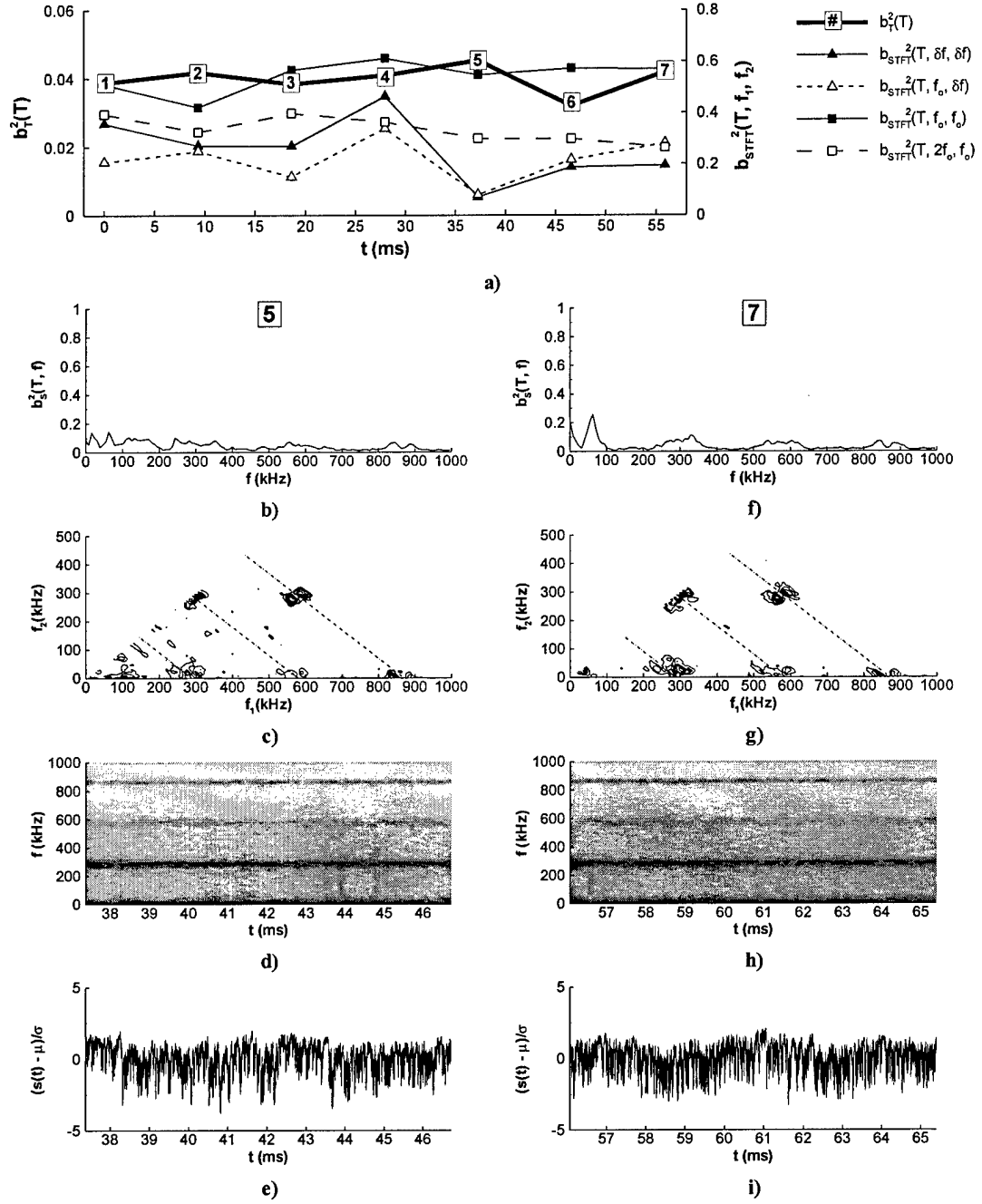


Figure 3.30 - Baseline case (91-6 adiabatic model), $R = 1879$, a) total bispectrum, b) and f) summed bispectrum, c) and g) STFT bispectrum, d) and h) magnitude of STFT, e) and i) normalized time series.

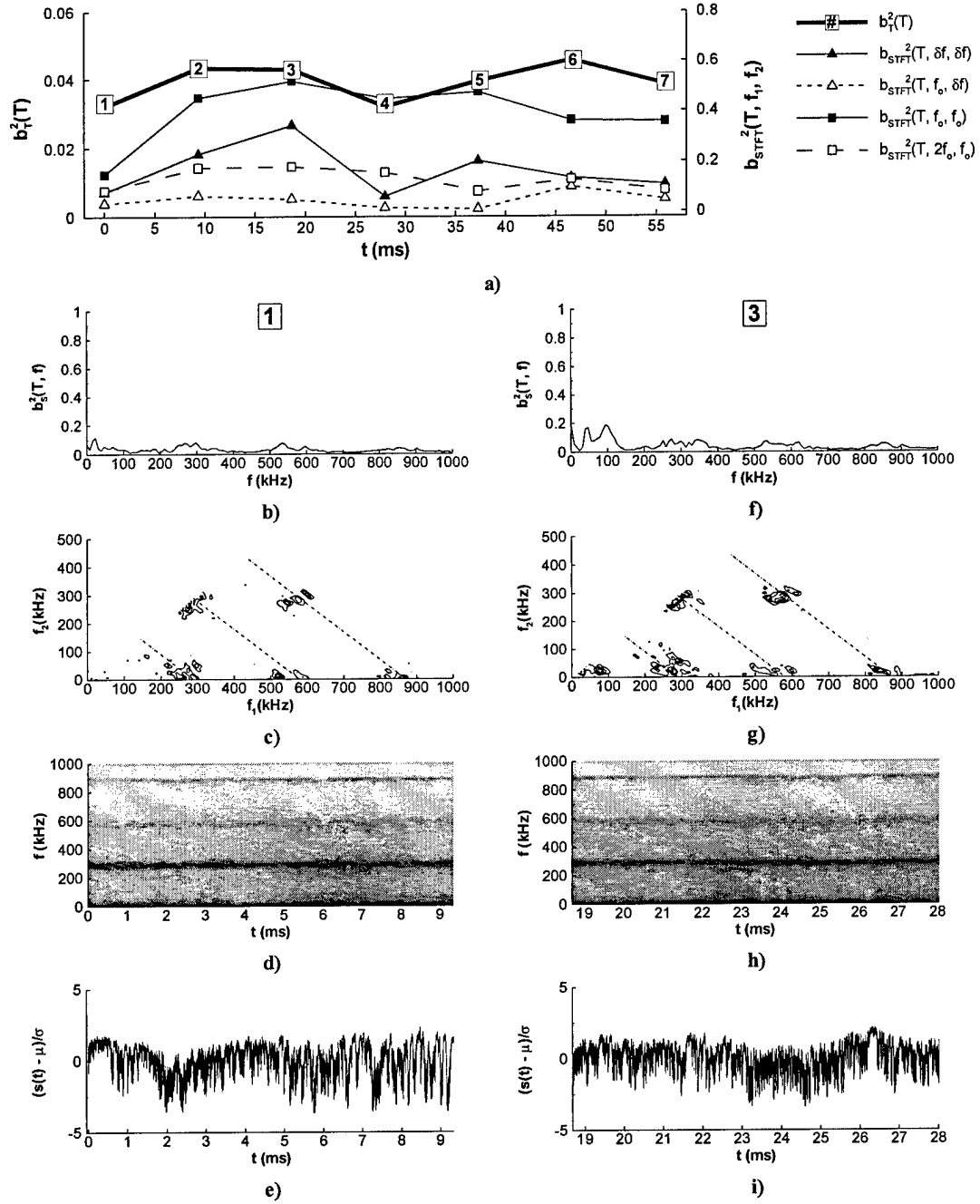


Figure 3.31 - Baseline case (91-6 adiabatic model), $R = 1940$, a) total bispectrum, b) and f) summed bispectrum, c) and g) STFT bispectrum, d) and h) magnitude of STFT, e) and i) normalized time series.

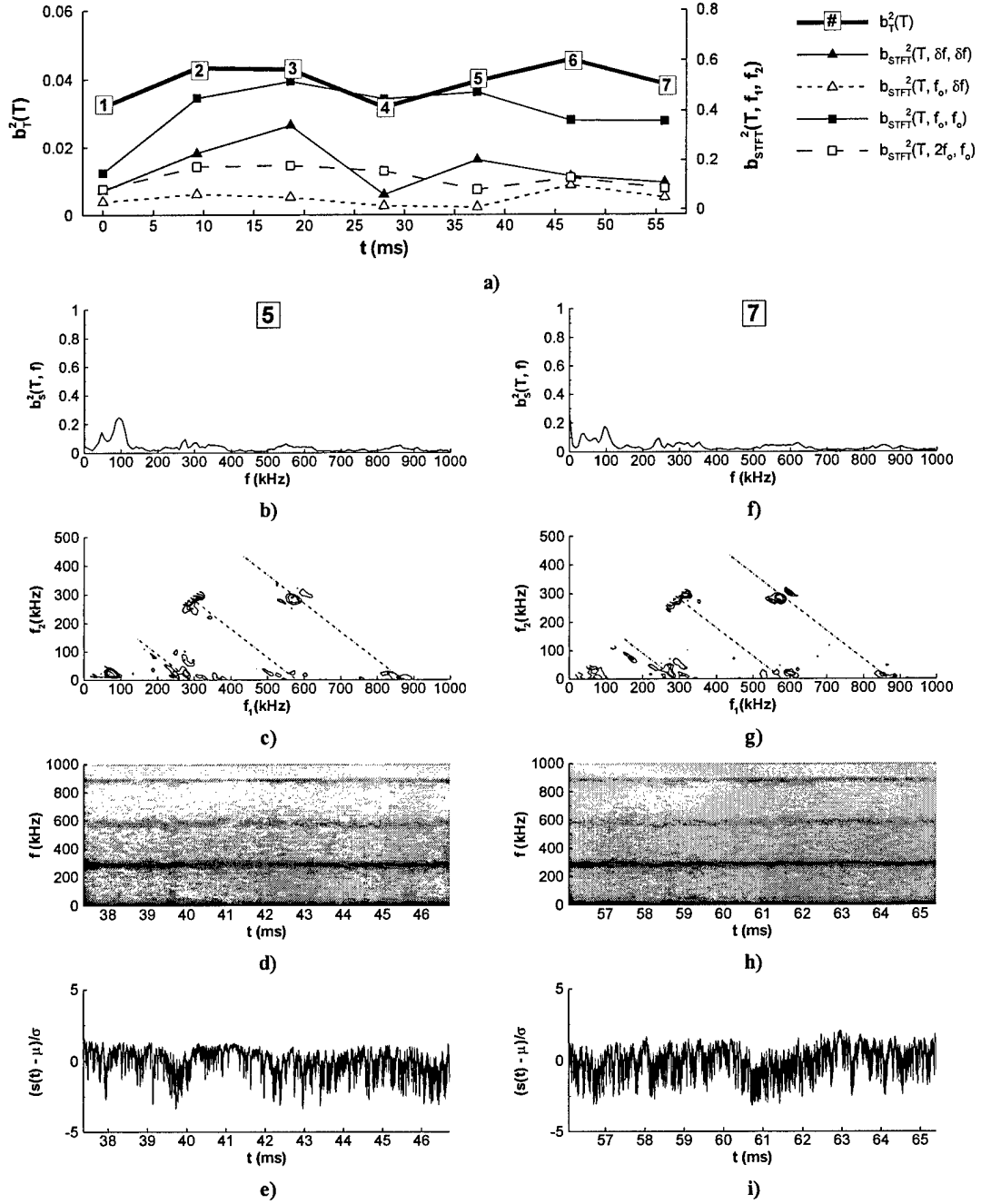


Figure 3.32 - Baseline case (91-6 adiabatic model), $R = 1940$, a) total bispectrum, b) and f) summed bispectrum, c) and g) STFT bispectrum, d) and h) magnitude of STFT, e) and i) normalized time series.

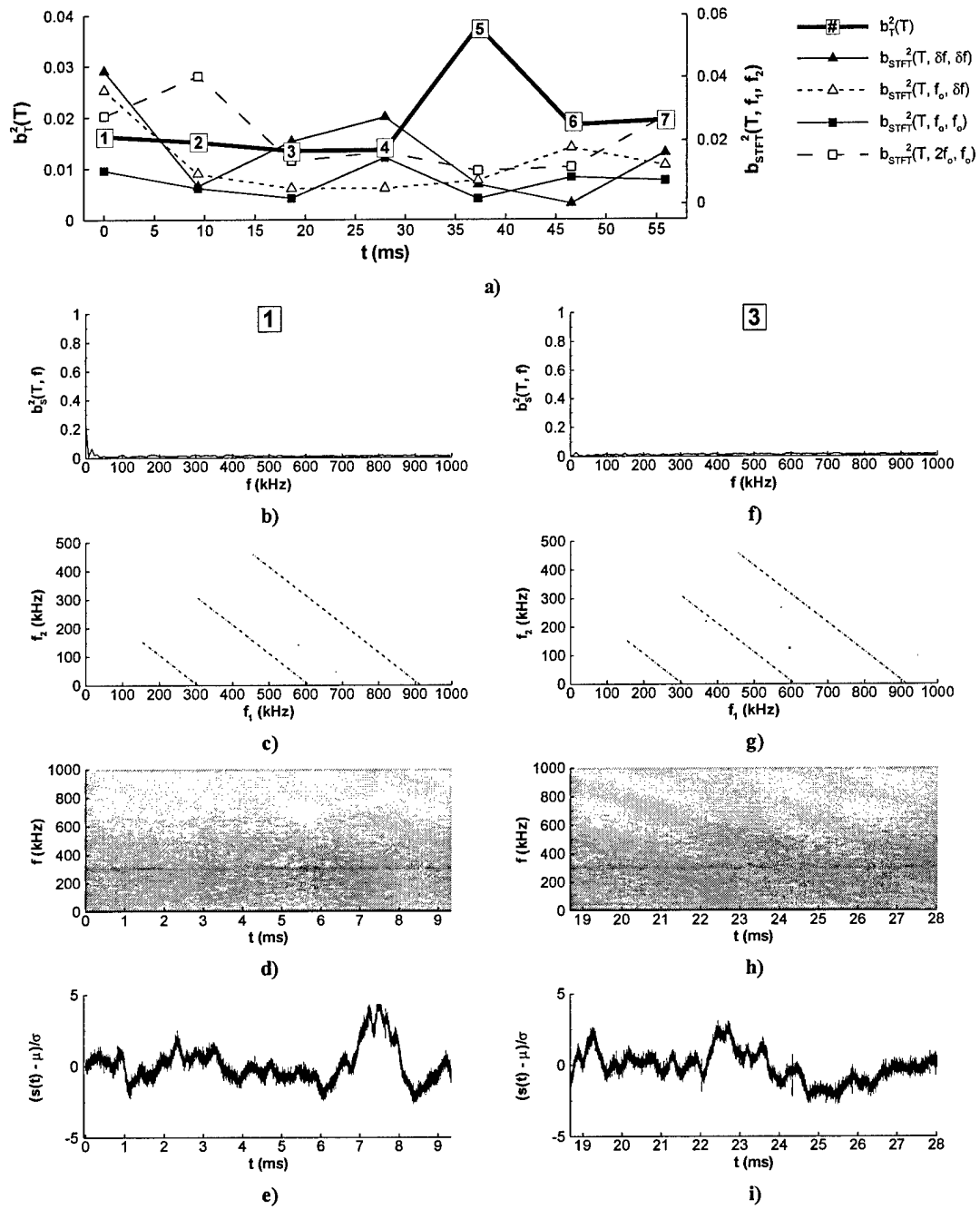


Figure 3.33 - 91-6 cooled wall model, $R = 1609$, a) total bispectrum, b) and f) summed bispectrum, c) and g) STFT bispectrum, d) and h) magnitude of STFT, e) and i) normalized time series.

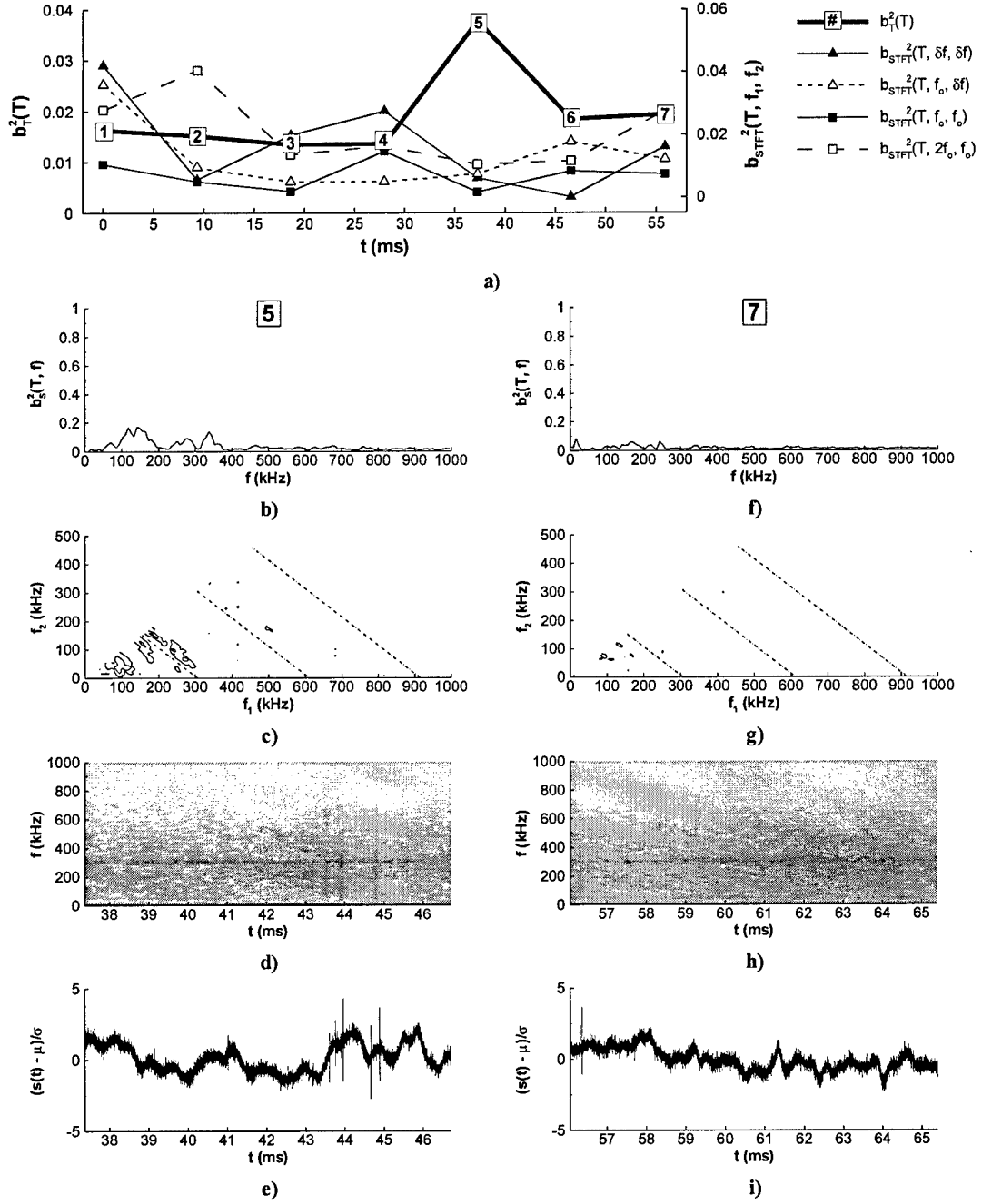


Figure 3.34 - 91-6 cooled wall model, $R = 1609$, a) total bispectrum, b) and f) summed bispectrum, c) and g) STFT bispectrum, d) and h) magnitude of STFT, e) and i) normalized time series.

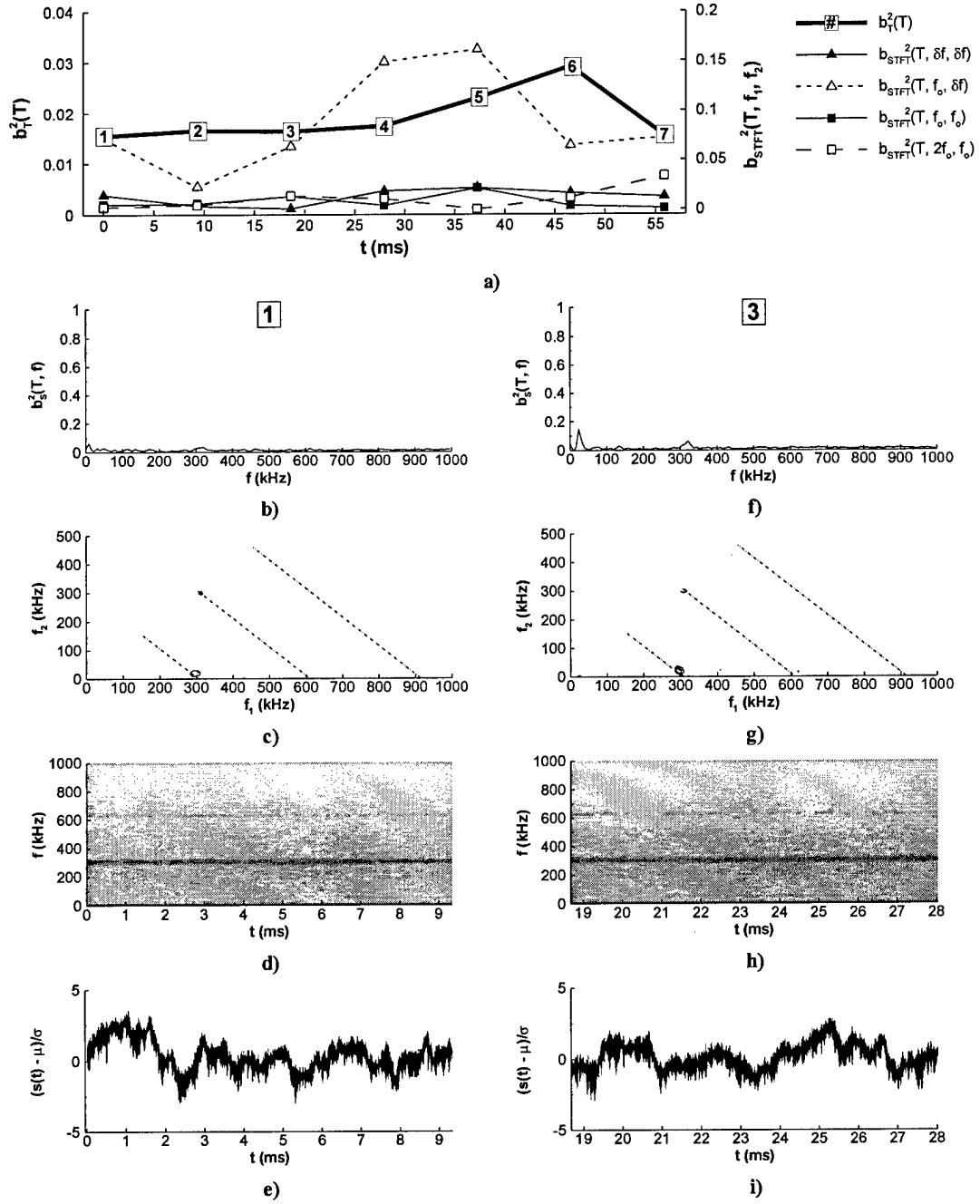


Figure 3.35 - 91-6 cooled wall model, $R = 1680$, a) total bispectrum, b) and f) summed bispectrum, c) and g) STFT bispectrum, d) and h) magnitude of STFT, e) and i) normalized time series.

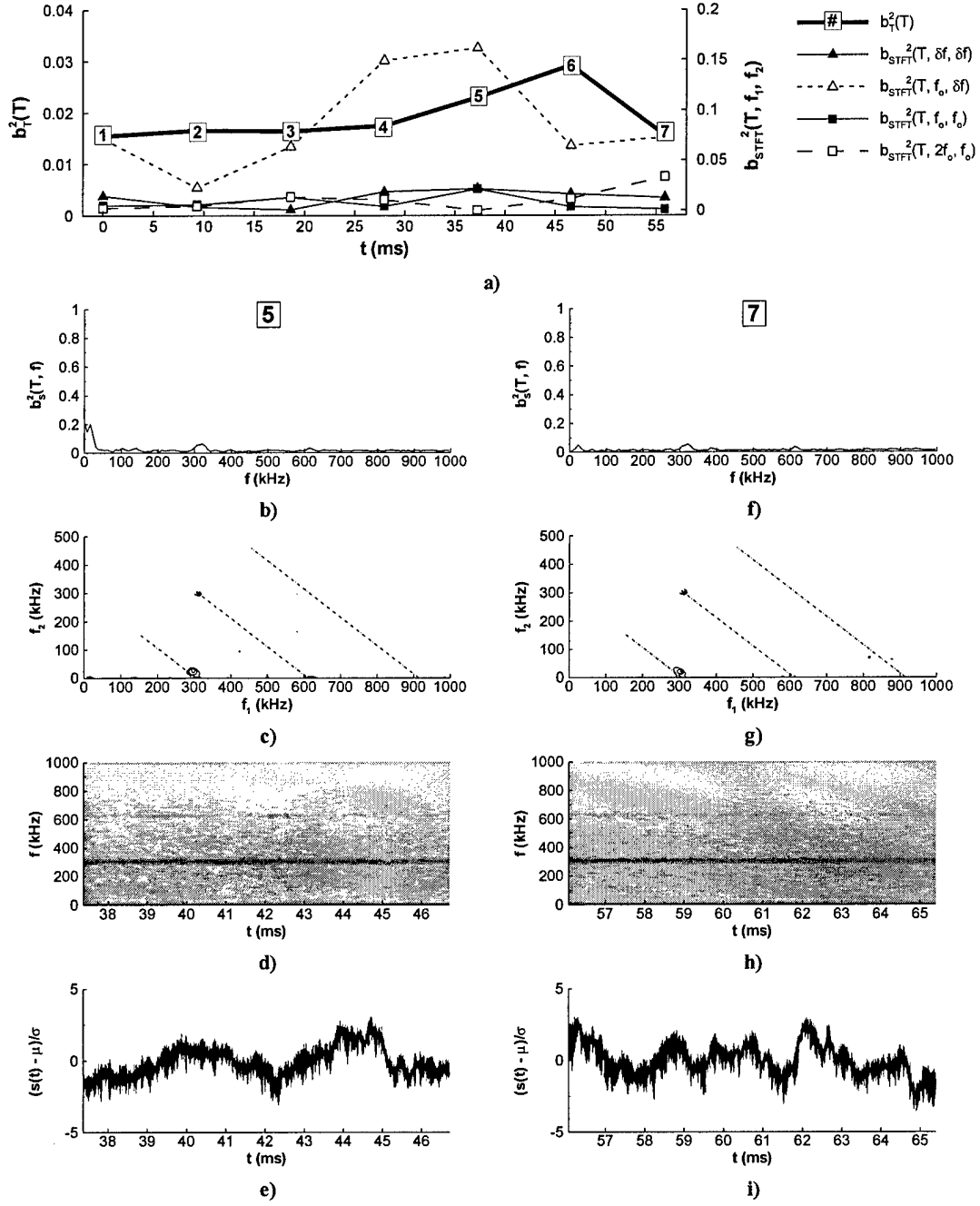


Figure 3.36 - 91-6 cooled wall model, $R = 1680$, a) total bispectrum, b) and f) summed bispectrum, c) and g) STFT bispectrum, d) and h) magnitude of STFT, e) and i) normalized time series.

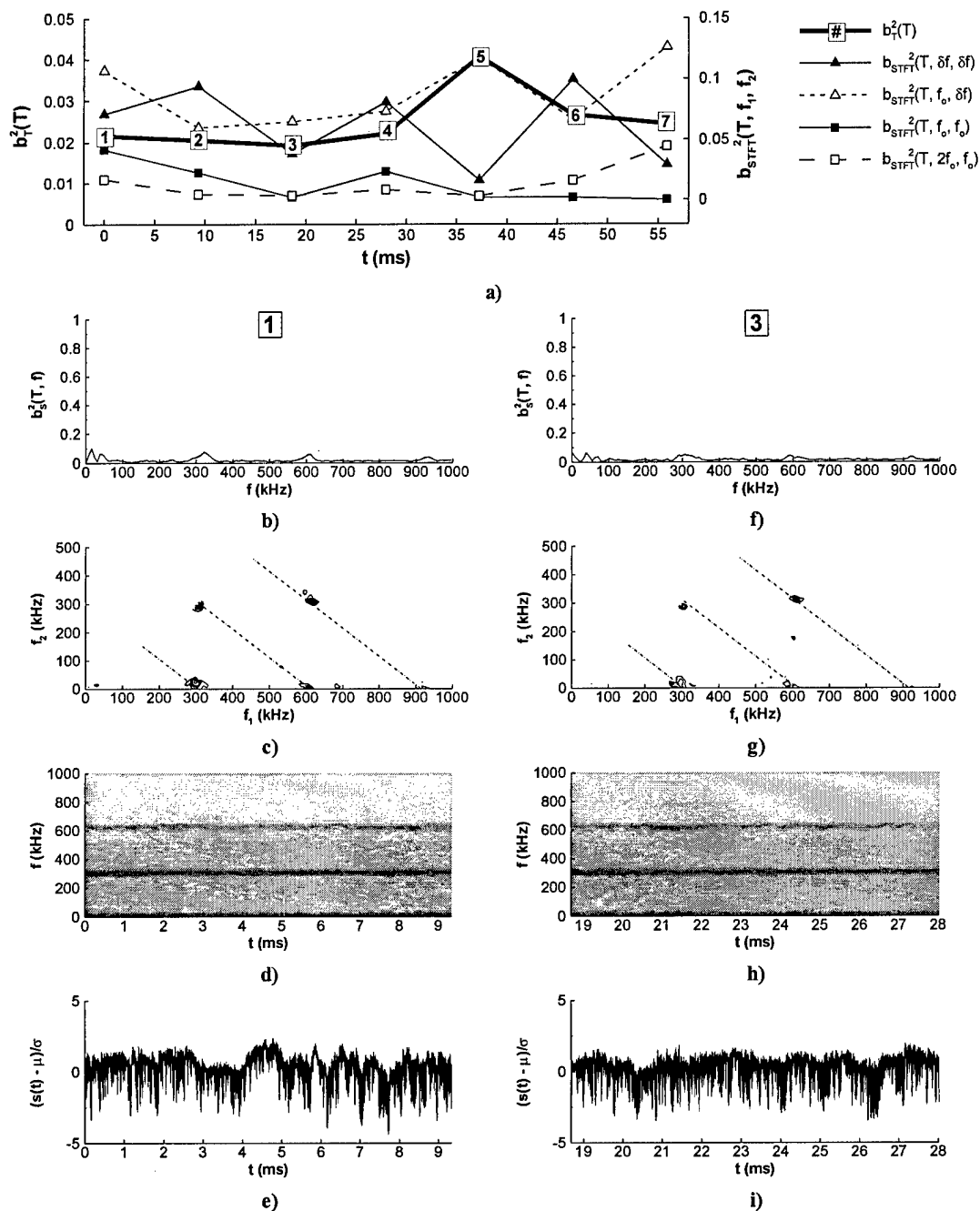


Figure 3.37 - 91-6 cooled wall model, $R = 1749$, a) total bispectrum, b) and f) summed bispectrum, c) and g) STFT bispectrum, d) and h) magnitude of STFT, e) and i) normalized time series.

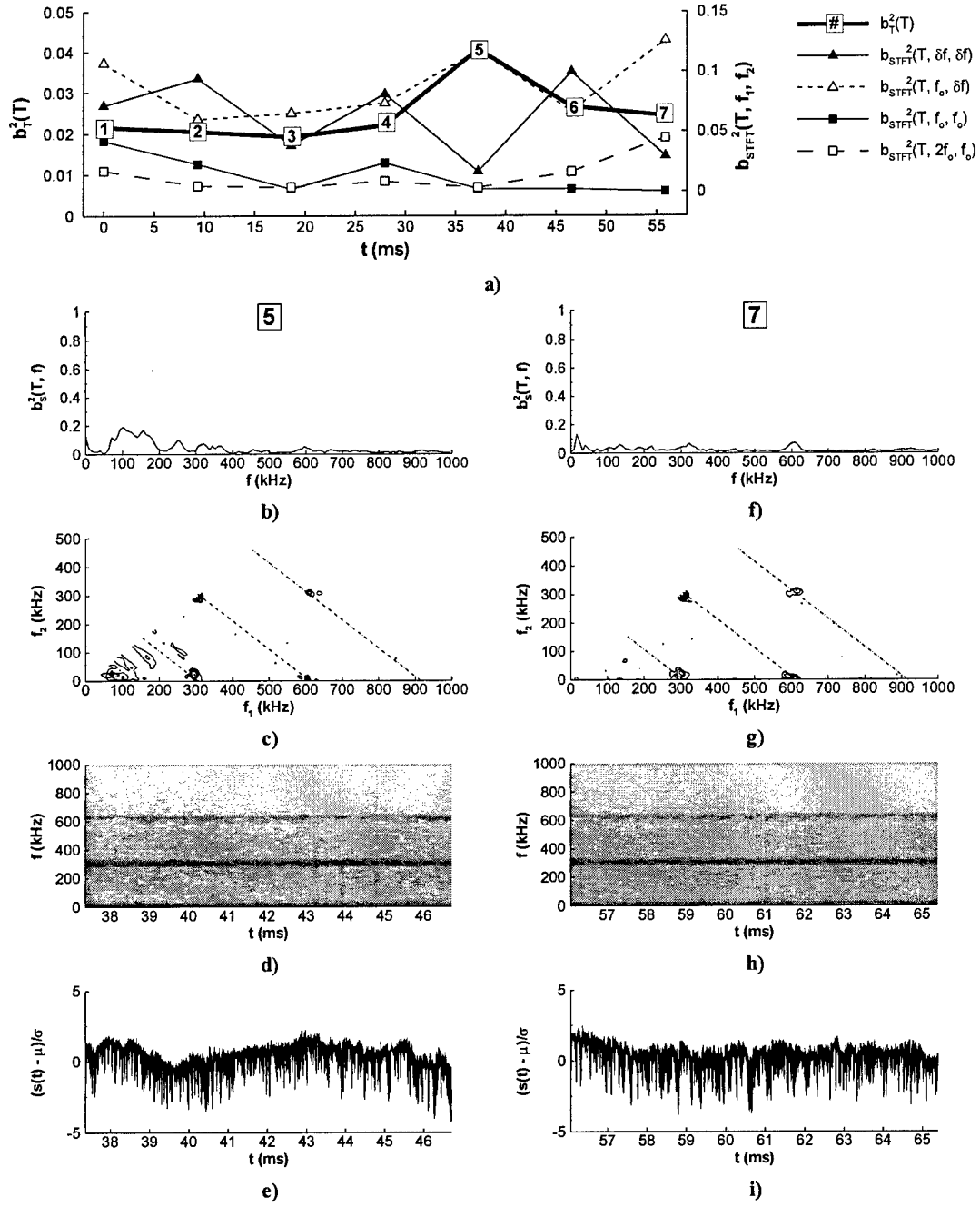


Figure 3.38 - 91-6 cooled wall model, $R = 1749$, a) total bispectrum, b) and f) summed bispectrum, c) and g) STFT bispectrum, d) and h) magnitude of STFT, e) and i) normalized time series.

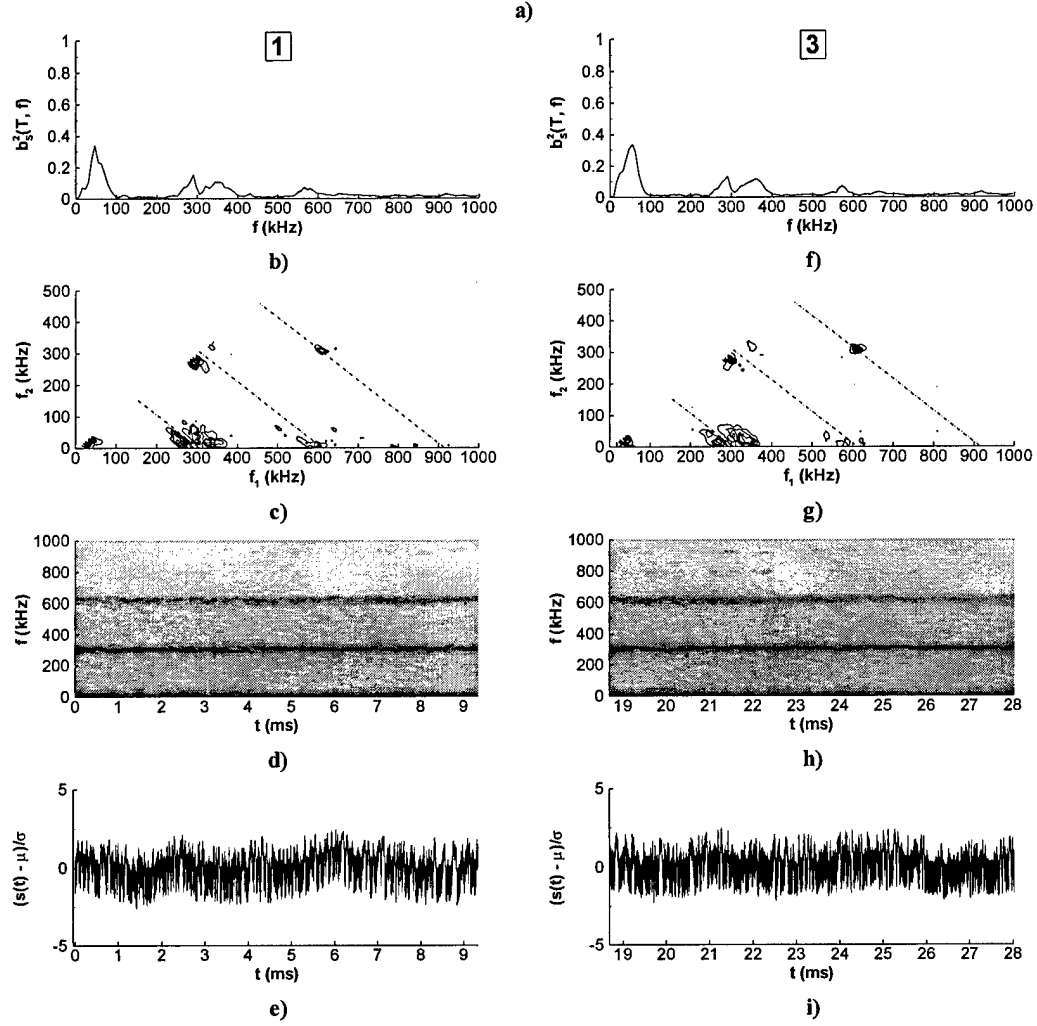
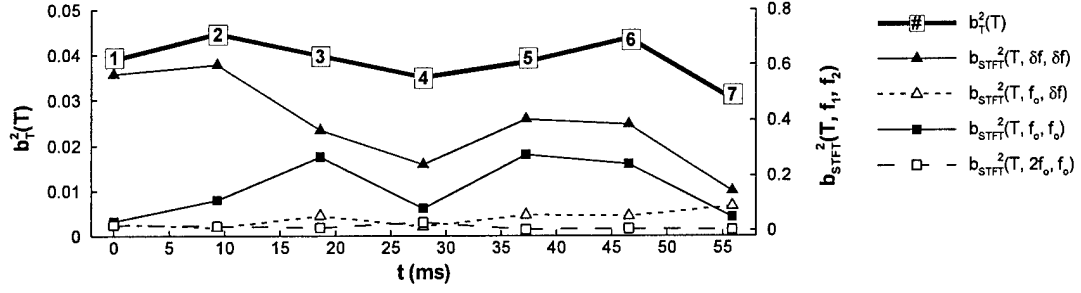


Figure 3.39 - 91-6 cooled wall model, $R = 1815$, a) total bispectrum, b) and f) summed bispectrum, c) and g) STFT bispectrum, d) and h) magnitude of STFT, e) and i) normalized time series.

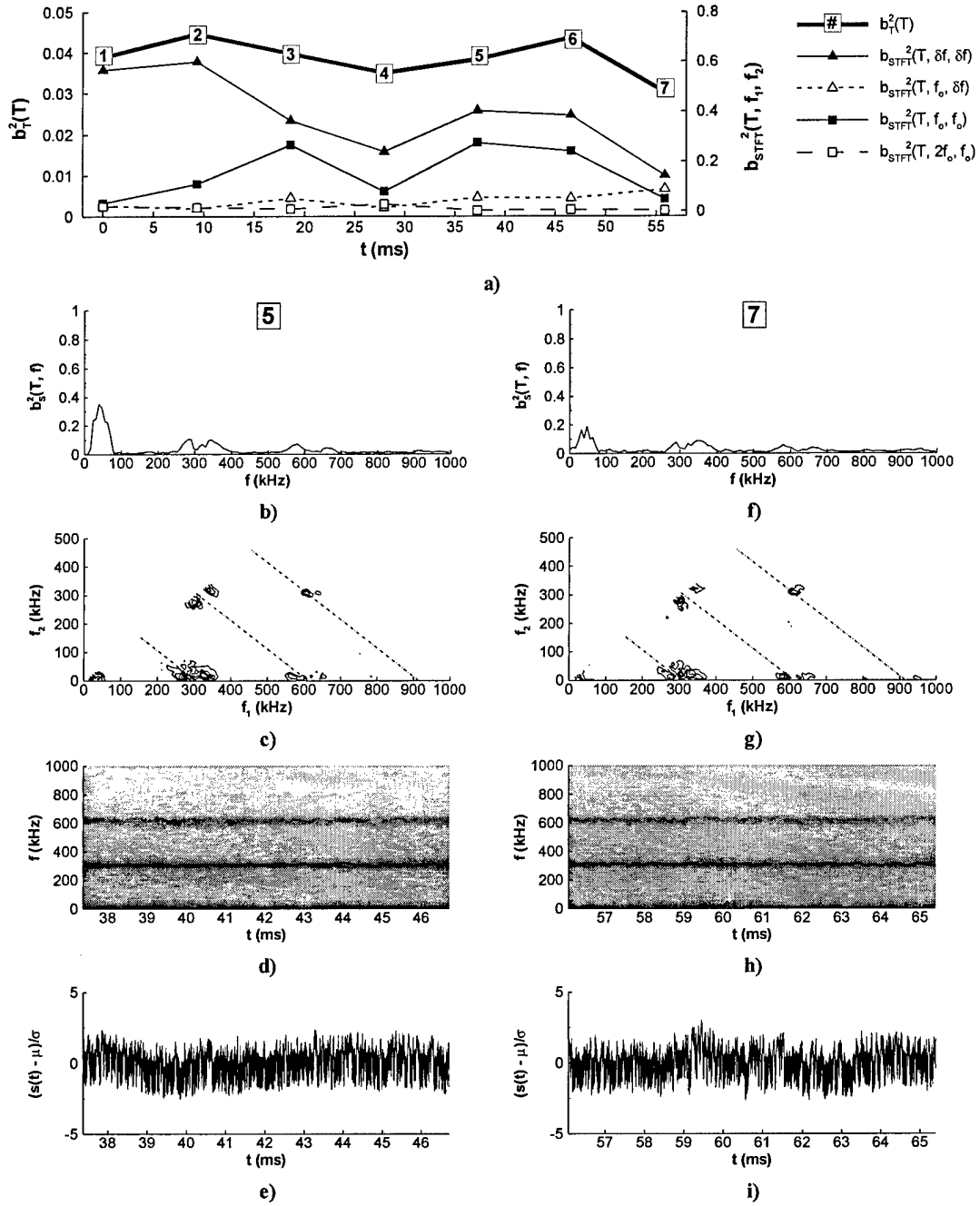


Figure 3.40 - 91-6 cooled wall model, $R = 1815$, a) total bispectrum, b) and f) summed bispectrum, c) and g) STFT bispectrum, d) and h) magnitude of STFT, e) and i) normalized time series.

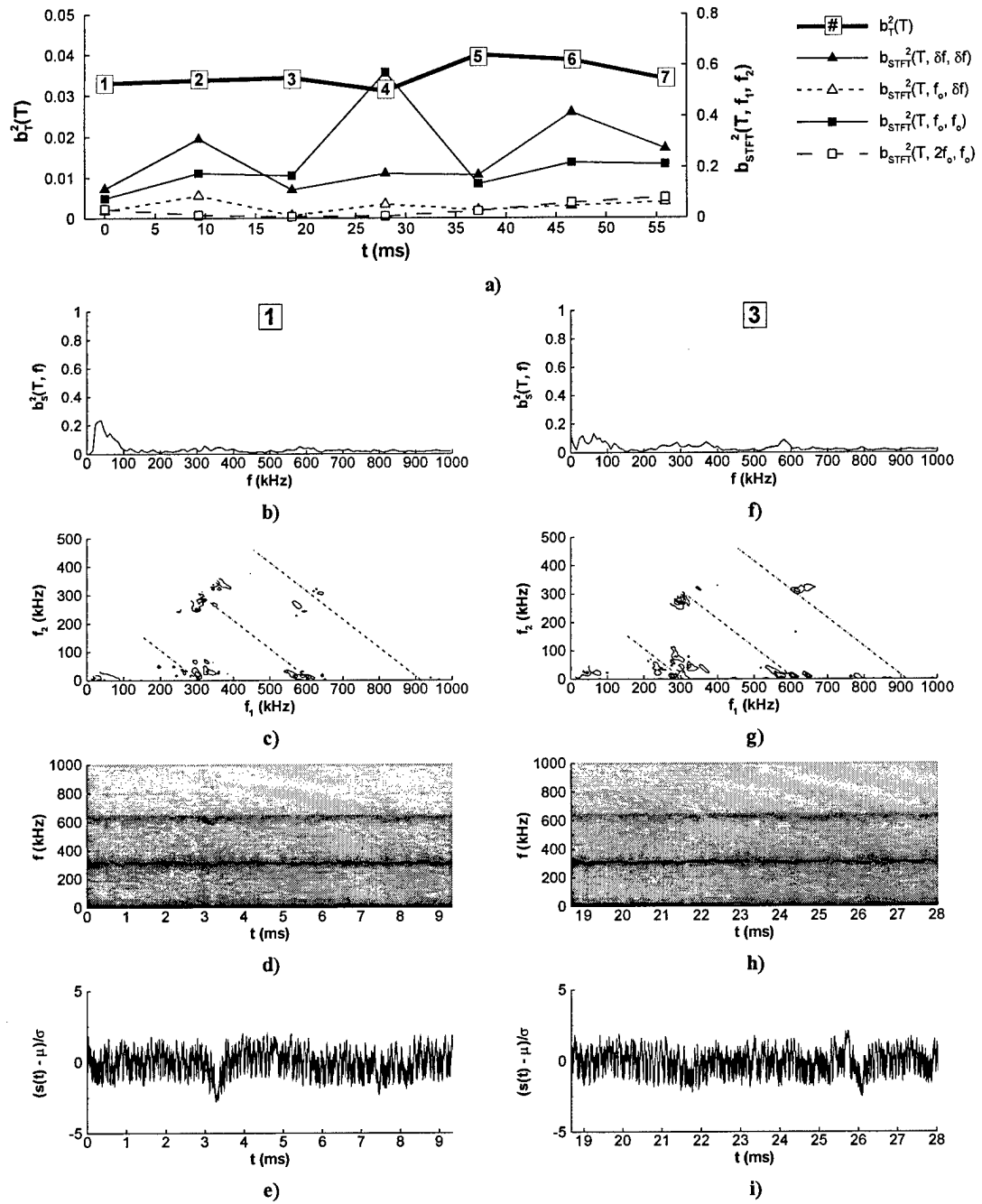


Figure 3.41 - 91-6 cooled wall model, $R = 1879$, a) total bispectrum, b) and f) summed bispectrum, c) and g) STFT bispectrum, d) and h) magnitude of STFT, e) and i) normalized time series.

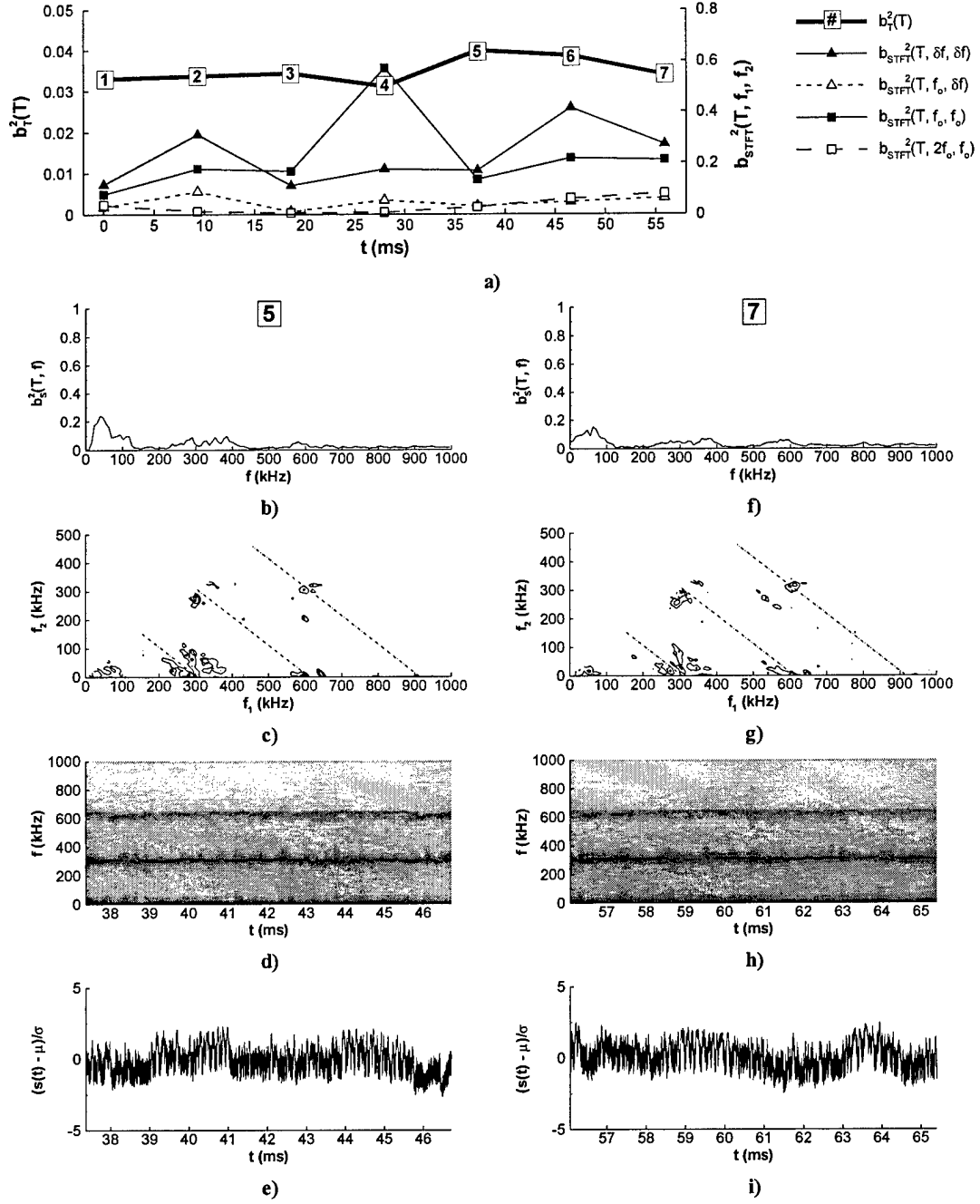


Figure 3.42 - 91-6 cooled wall model, $R = 1879$, a) total bispectrum, b) and f) summed bispectrum, c) and g) STFT bispectrum, d) and h) magnitude of STFT, e) and i) normalized time series.

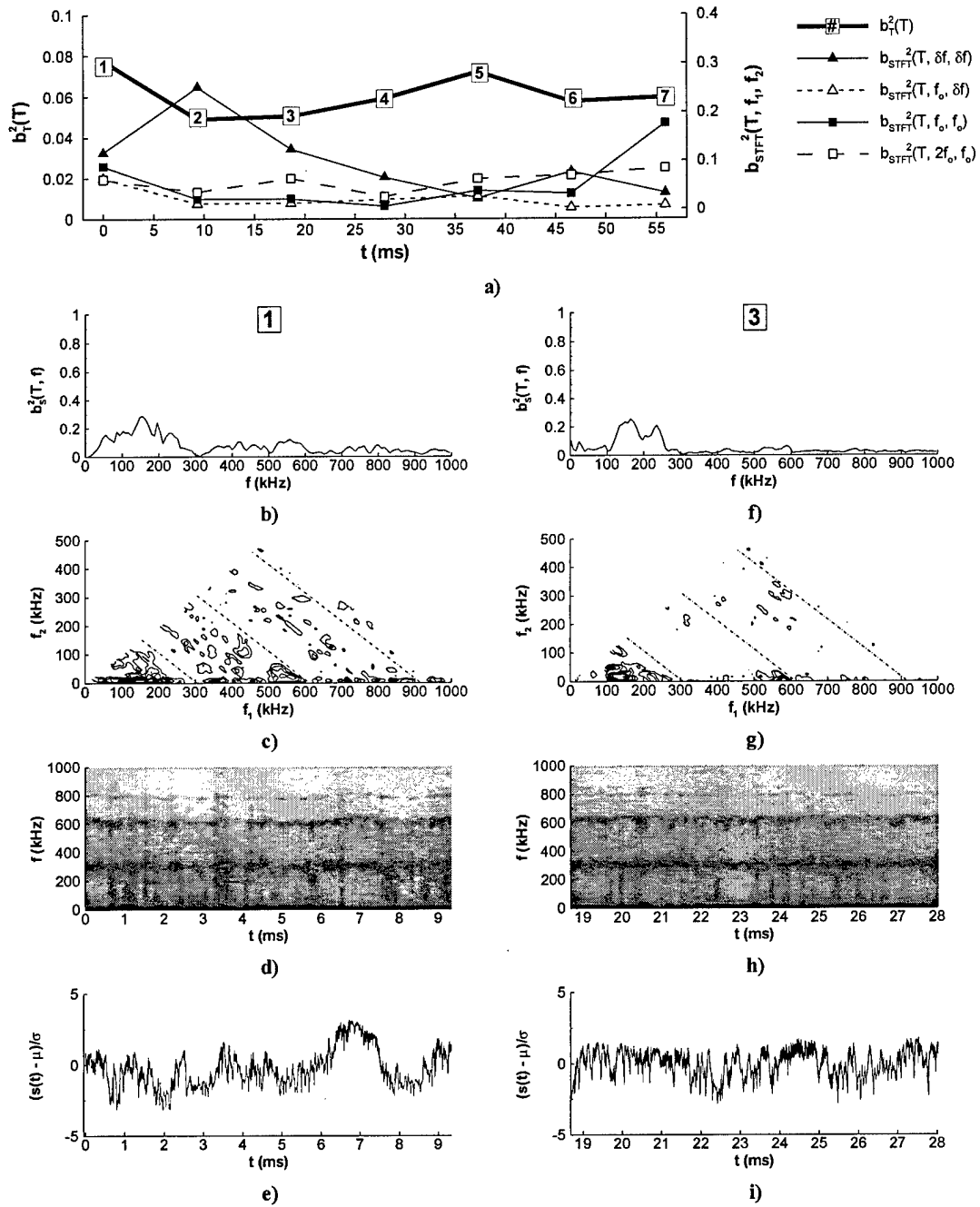


Figure 3.43 - 91-6 cooled wall model, $R = 1940$, a) total bispectrum, b) and f) summed bispectrum, c) and g) STFT bispectrum, d) and h) magnitude of STFT, e) and i) normalized time series.

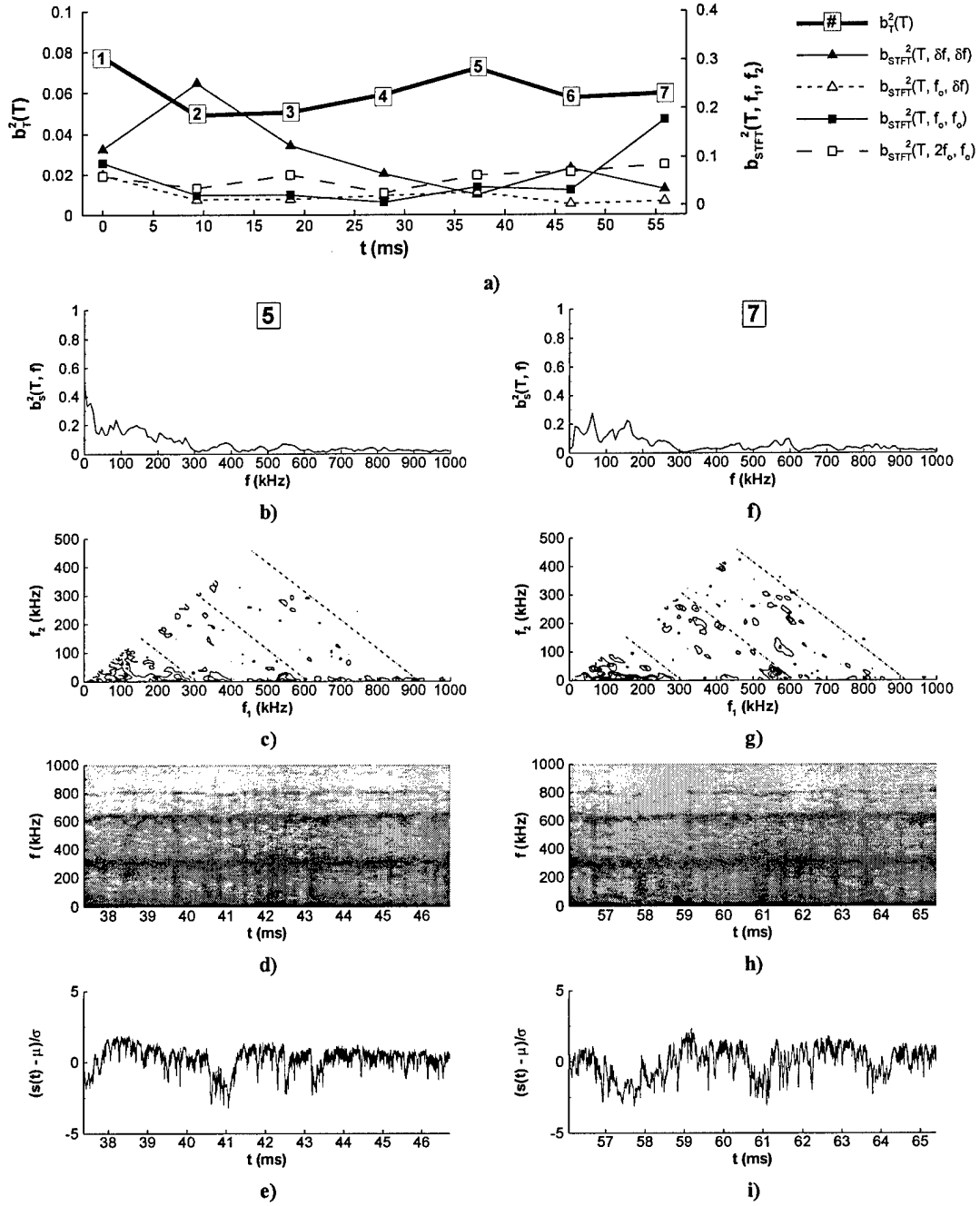


Figure 3.44 - 91-6 cooled wall model, $R = 1940$, a) total bispectrum, b) and f) summed bispectrum, c) and g) STFT bispectrum, d) and h) magnitude of STFT, e) and i) normalized time series.

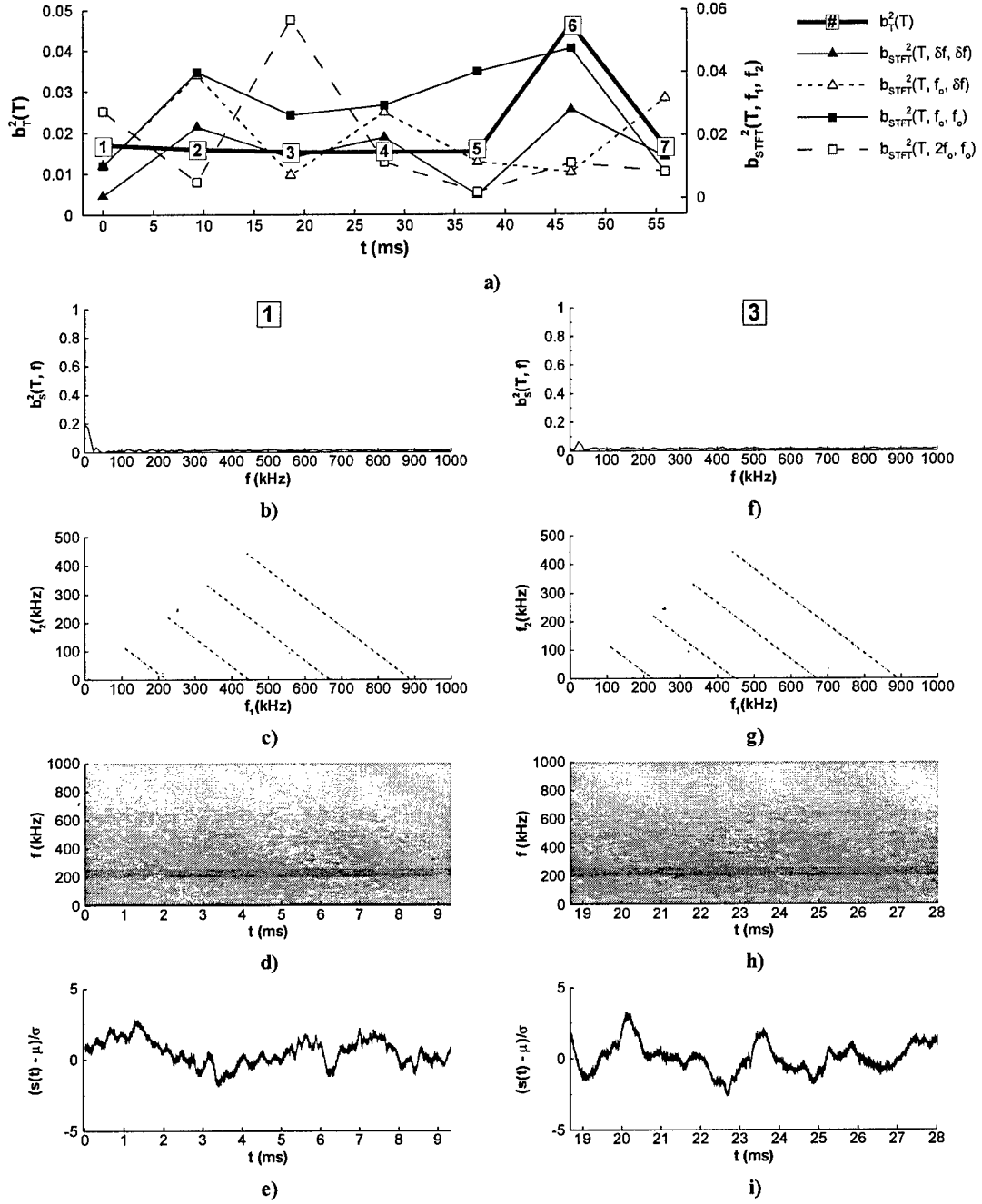


Figure 3.45 - 93-10 adiabatic wall model, $R = 1879$, a) total bispectrum, b) and f) summed bispectrum, c) and g) STFT bispectrum, d) and h) magnitude of STFT, e) and i) normalized time series.

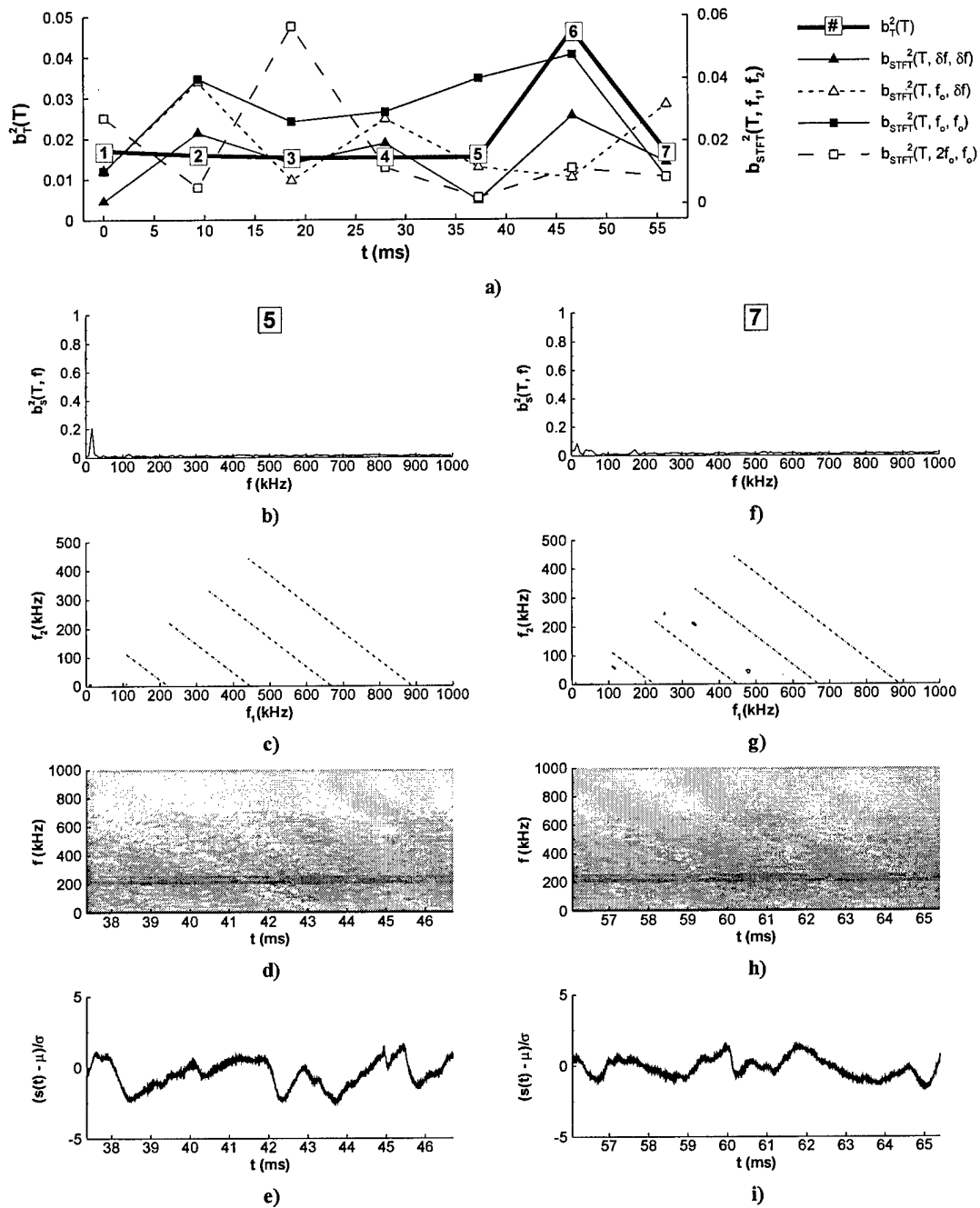


Figure 3.46 - 93-10 adiabatic wall model, $R = 1879$, a) total bispectrum, b) and f) summed bispectrum, c) and g) STFT bispectrum, d) and h) magnitude of STFT, e) and i) normalized time series.

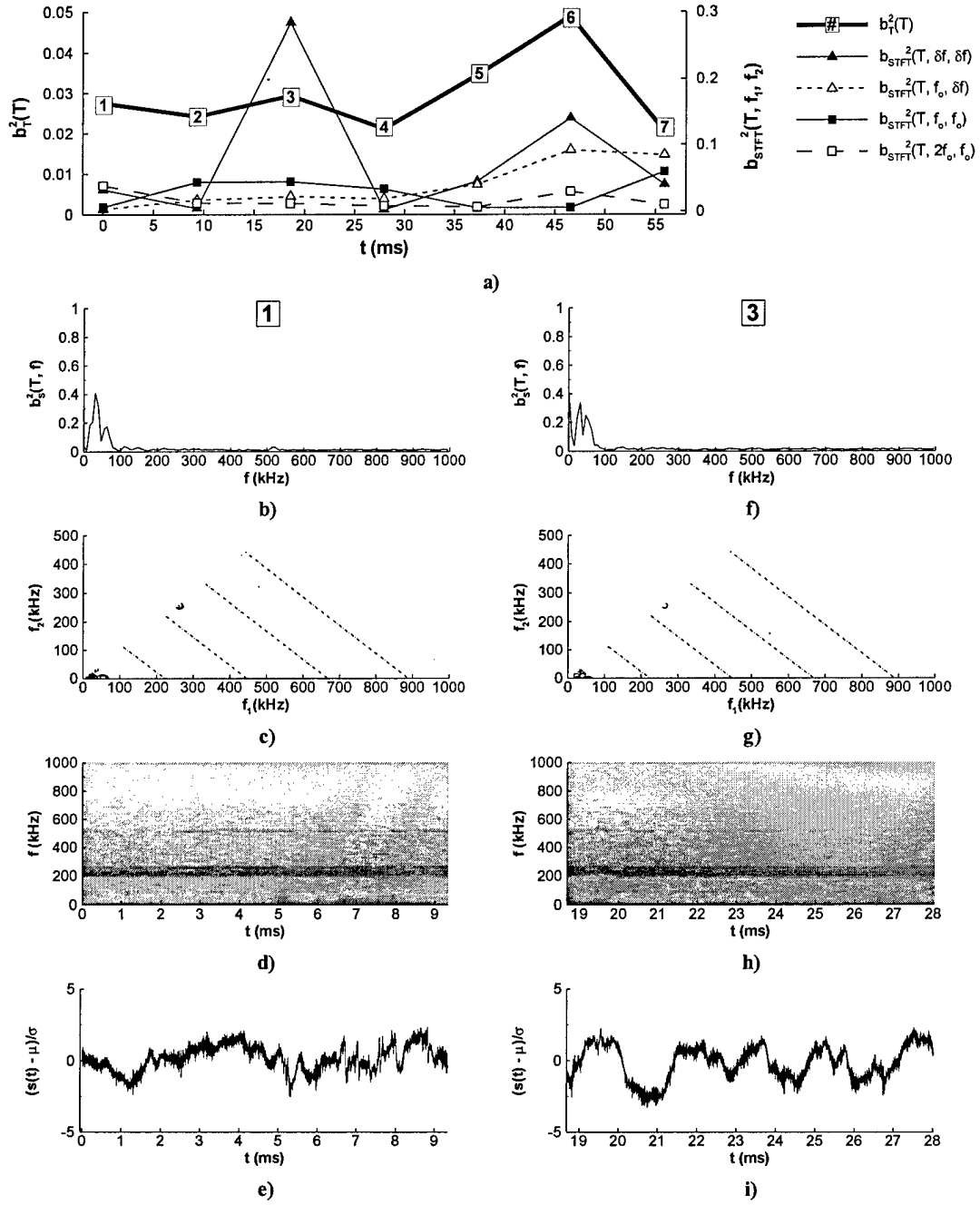


Figure 3.47 - 93-10 adiabatic wall model, $R = 1940$, a) total bispectrum, b) and f) summed bispectrum, c) and g) STFT bispectrum, d) and h) magnitude of STFT, e) and i) normalized time series.

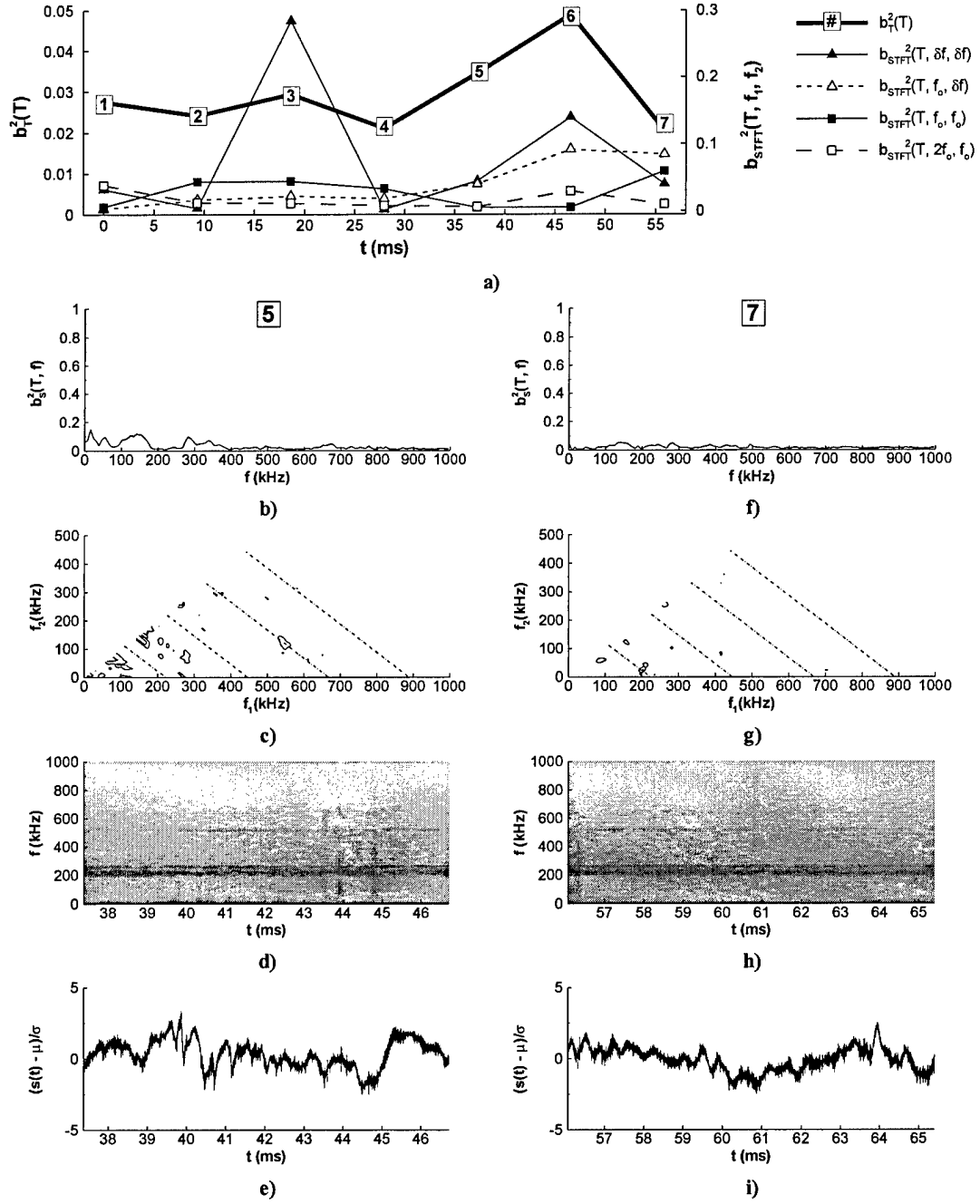


Figure 3.48 - 93-10 adiabatic wall model, $R = 1940$, a) total bispectrum, b) and f) summed bispectrum, c) and g) STFT bispectrum, d) and h) magnitude of STFT, e) and i) normalized time series.

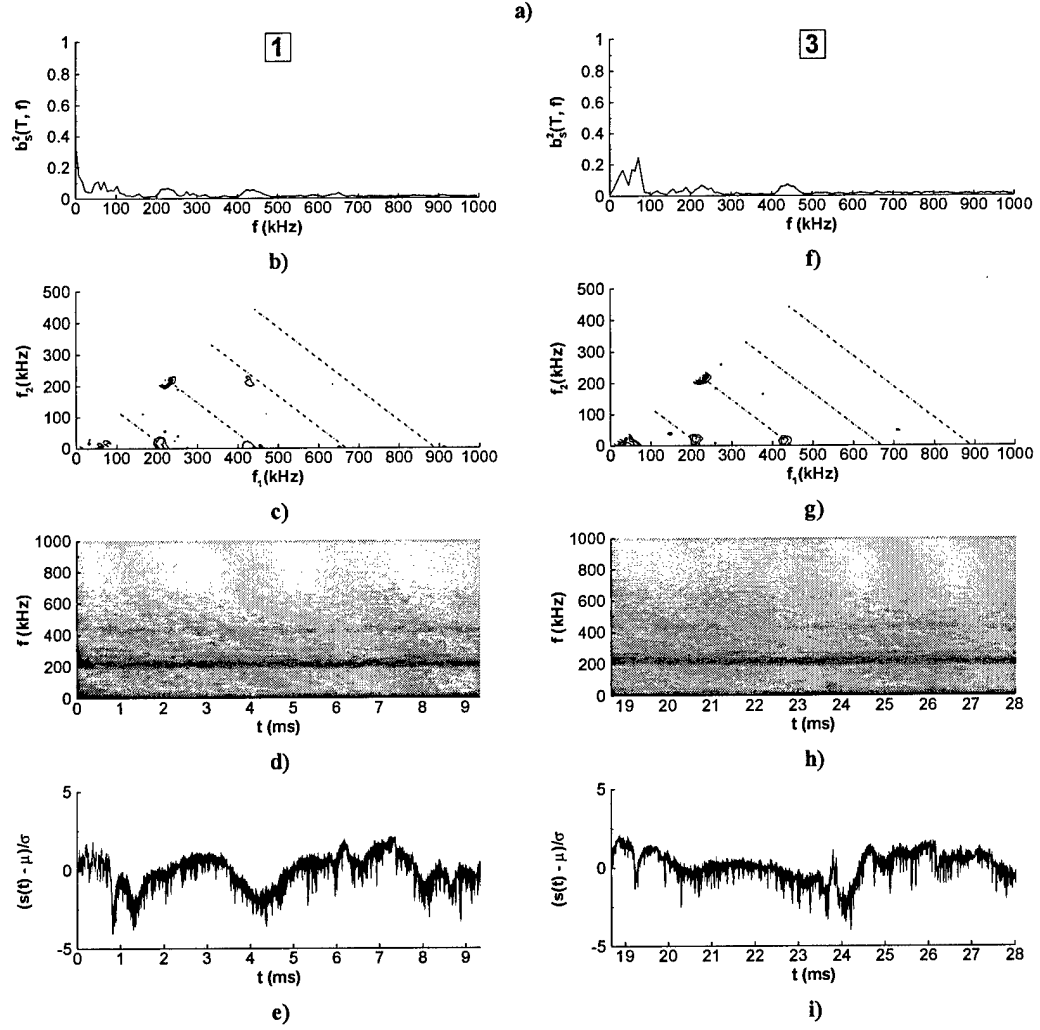
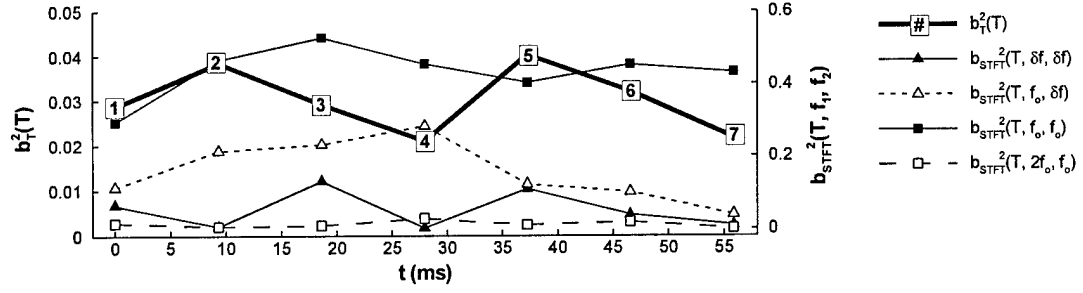


Figure 3.49 - 93-10 adiabatic wall model, $R = 2000$, a) total bispectrum, b) and f) summed bispectrum, c) and g) STFT bispectrum, d) and h) magnitude of STFT, e) and i) normalized time series.

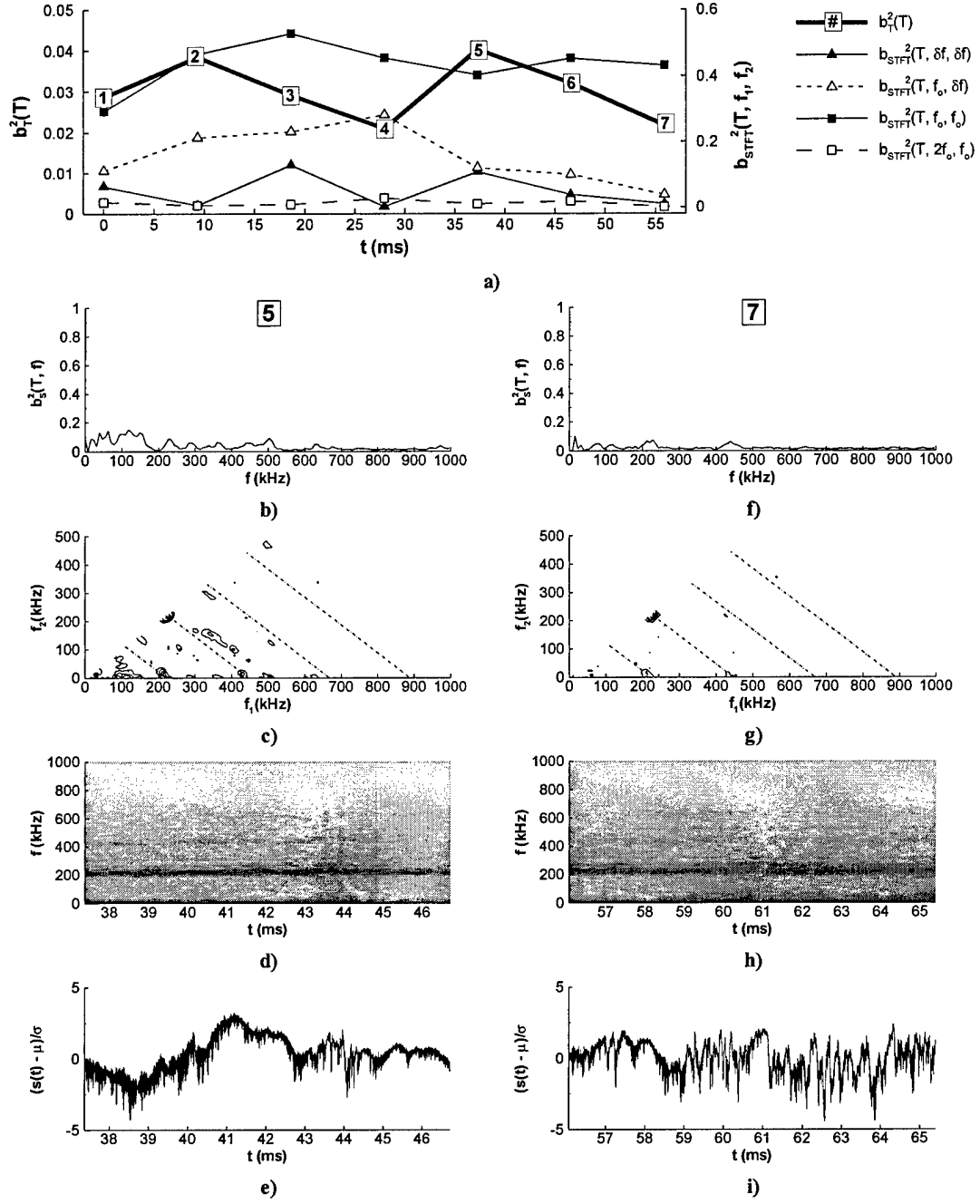


Figure 3.50 - 93-10 adiabatic wall model, $R = 2000$, a) total bispectrum, b) and f) summed bispectrum, c) and g) STFT bispectrum, d) and h) magnitude of STFT, e) and i) normalized time series.

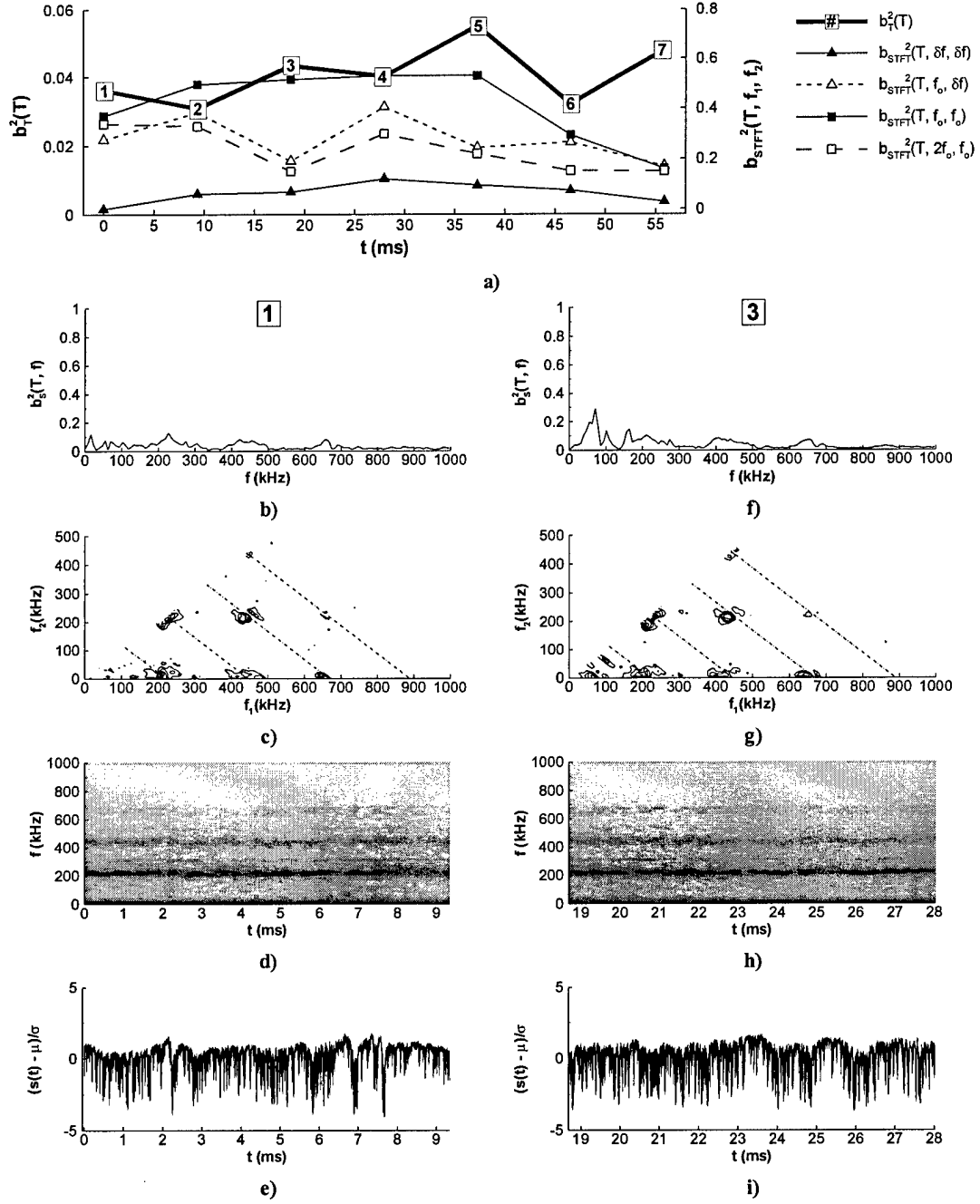


Figure 3.51 - 93-10 adiabatic wall model, $R = 2058$, a) total bispectrum, b) and f) summed bispectrum, c) and g) STFT bispectrum, d) and h) magnitude of STFT, e) and i) normalized time series.

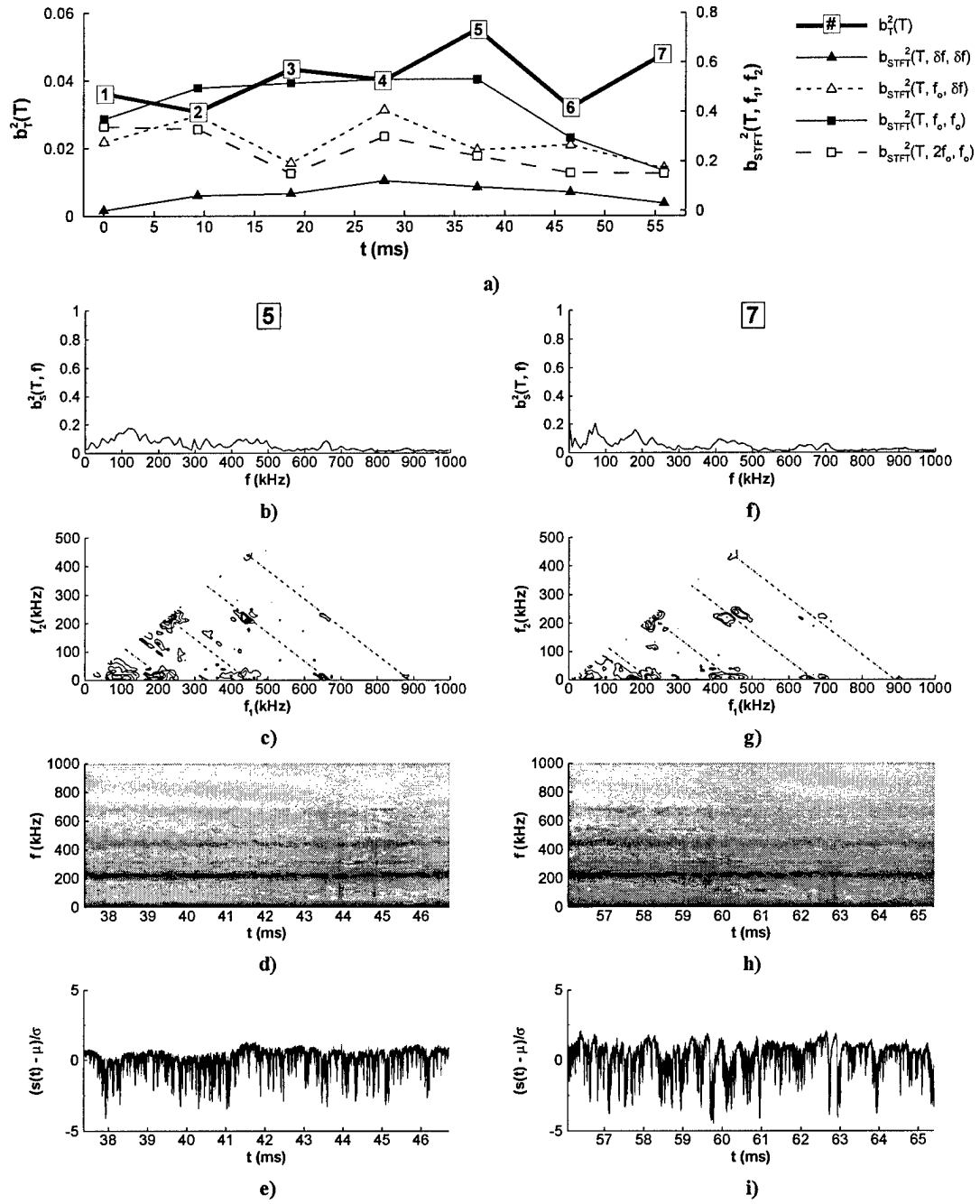


Figure 3.52 - 93-10 adiabatic wall model, $R = 2058$, a) total bispectrum, b) and f) summed bispectrum, c) and g) STFT bispectrum, d) and h) magnitude of STFT, e) and i) normalized time series.

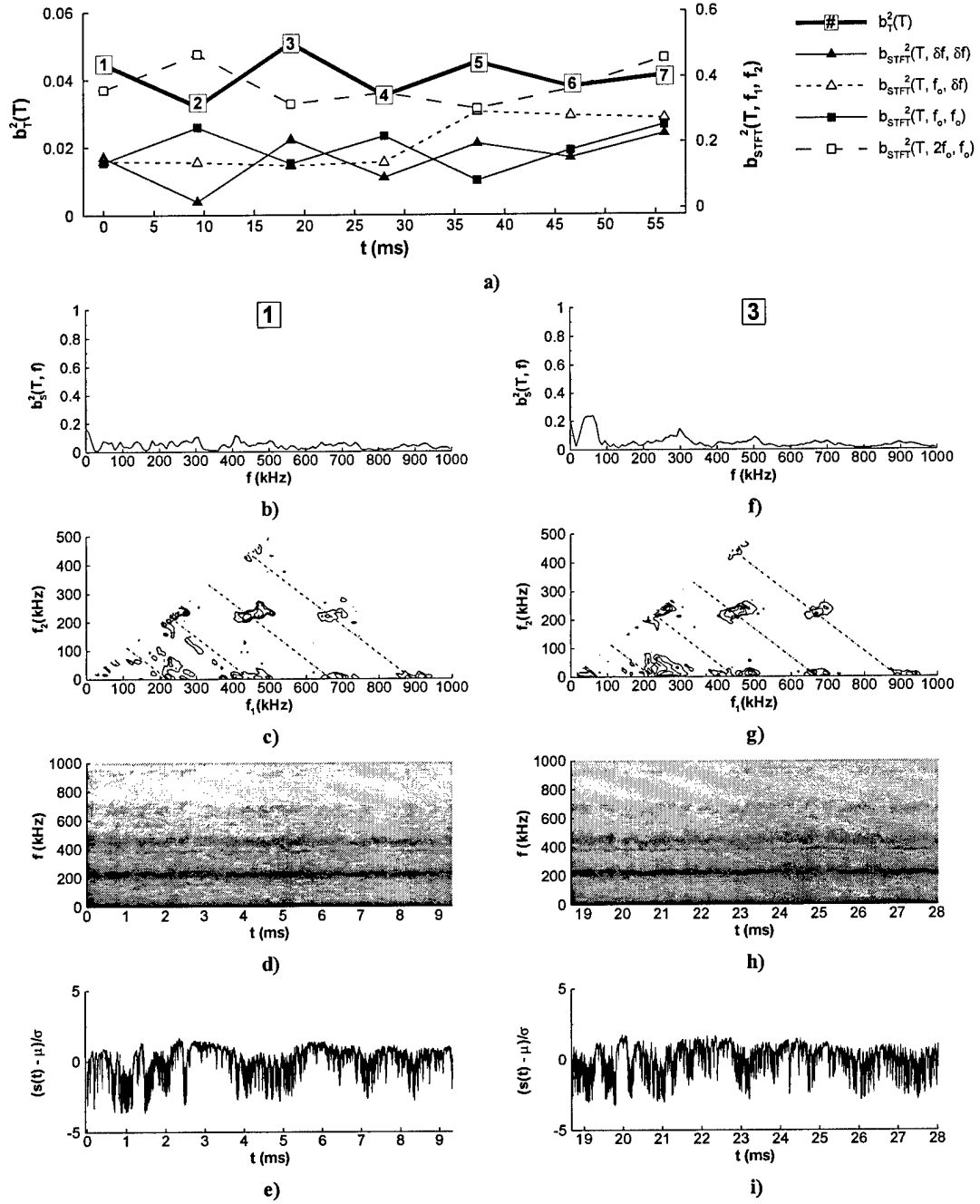


Figure 3.53 - 93-10 adiabatic wall model, $R = 2114$, a) total bispectrum, b) and f) summed bispectrum, c) and g) STFT bispectrum, d) and h) magnitude of STFT, e) and i) normalized time series.

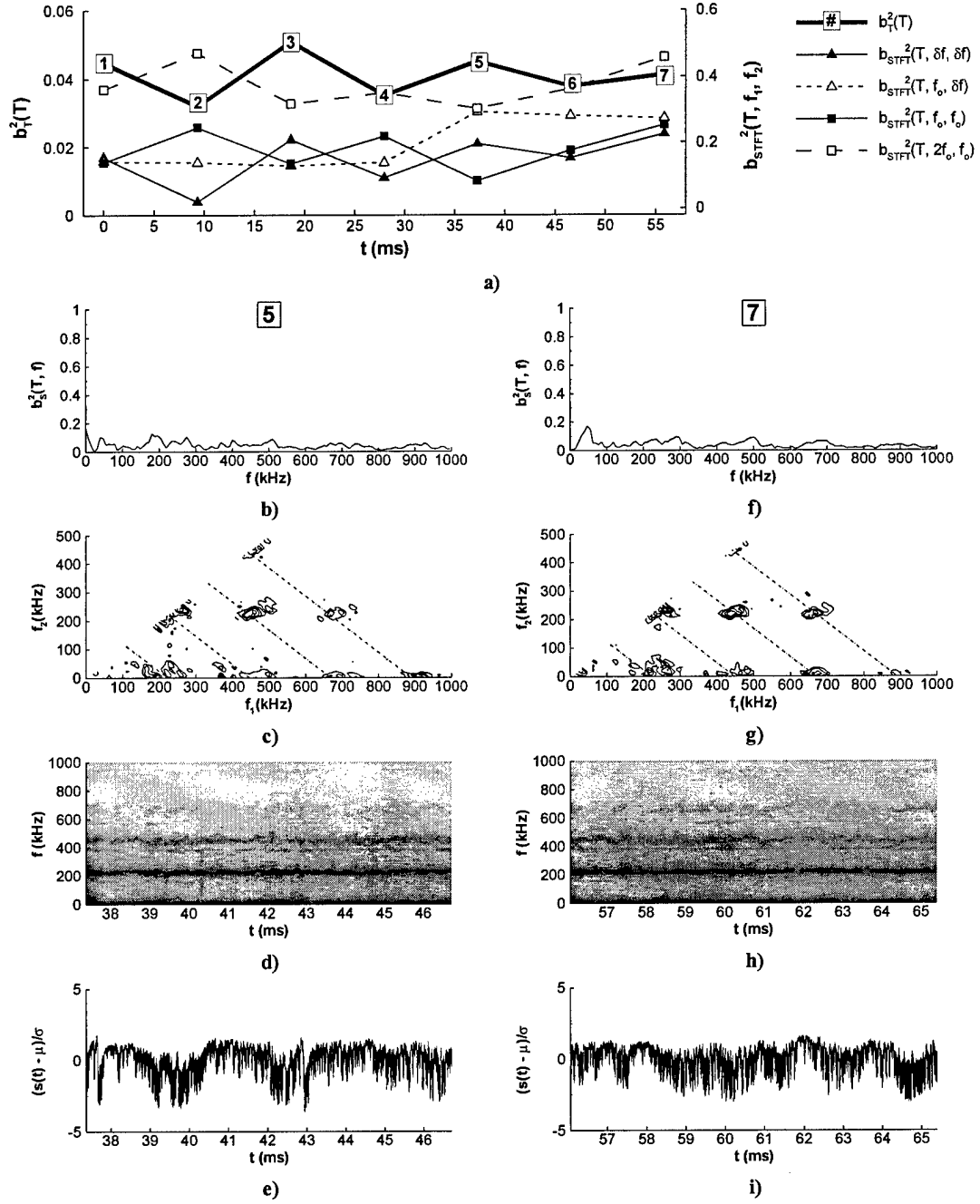


Figure 3.54 - 93-10 adiabatic wall model, $R = 2114$, a) total bispectrum, b) and f) summed bispectrum, c) and g) STFT bispectrum, d) and h) magnitude of STFT, e) and i) normalized time series.